Flexible, lightweight, silicon-based triple junction solar cell development

Federica Saitta

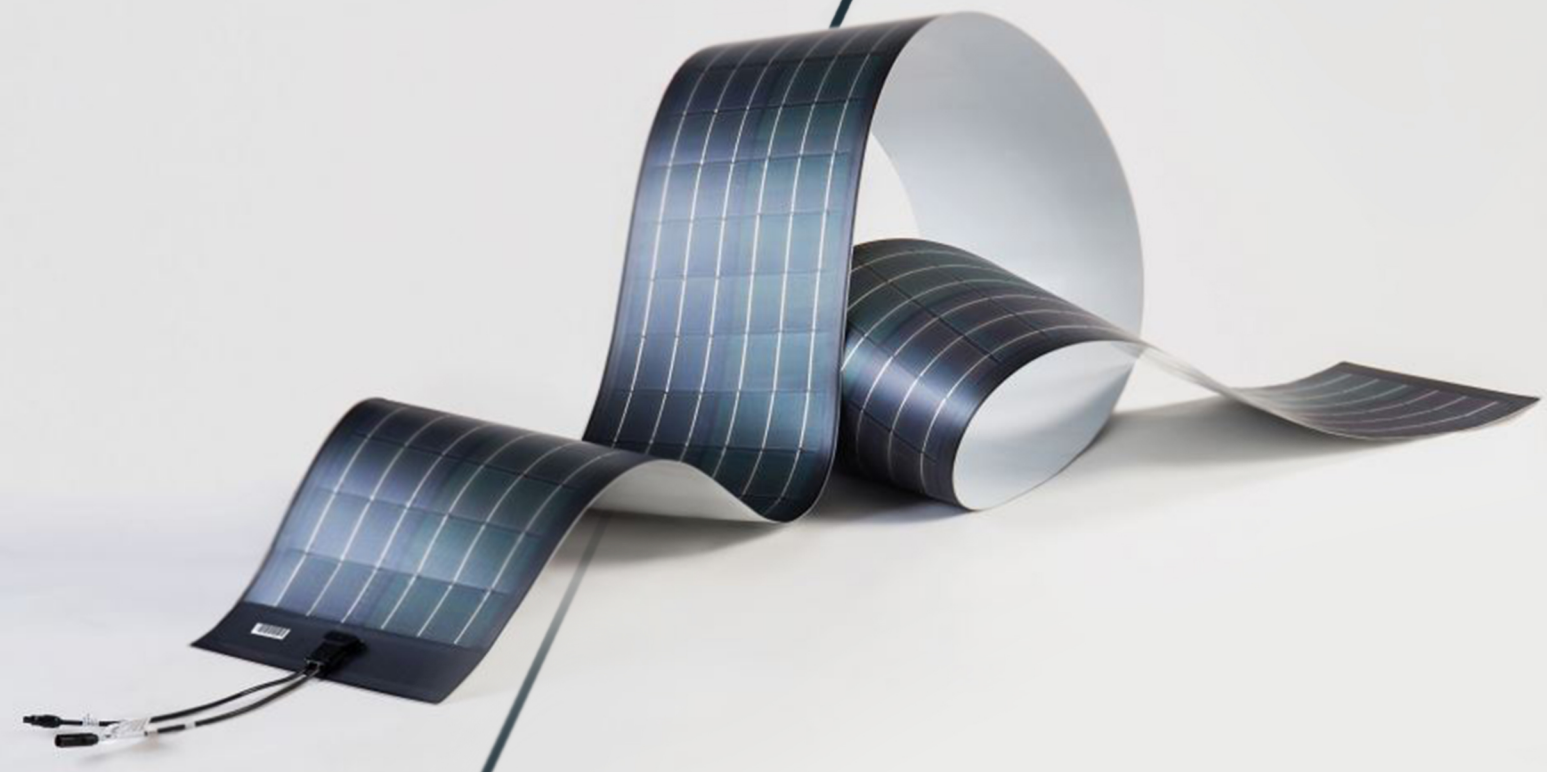

TU Delft Delft University of Technology

Flexible, lightweight, silicon-based triple junction solar cell development

by

Federica Saitta

to obtain the degree of Master of Science
at the Delft University of Technology,
to be defended publicly on Friday November 26, 2021 at 1:00 PM.

Student number:	5134552	
Project duration:	February 1, 2021 – November 26, 2021	
Thesis committee:	Prof. Dr. A.H.M. Smets,	TU Delft, PVMD supervisor
	Prof. Dr. R. A. C. M. M. van Swaaij,	TU Delft, ESE - PVMD
	Dr. ir. Aditya Shekhar,	TU Delft, DCE&S
	Dr. G. Limodio,	TU Delft, daily supervisor

Cover image by Huafei New Energy Co.Ltd, CIGS Flexible Solar module.
An electronic version of this thesis is available at `http://repository.tudelft.nl/`.

TU Delft Delft University of Technology

PVMD Delft University of Technology

HyET Solar Flexible light weight solar modules

Abstract

Photovoltaic solar energy is one of the most powerful renewable source and is a promising solution for one of the major challenges that our current generation faces: the transition of the global energy sector from fossil-based to zero-carbon emissions. In order to reach this goal, the second generation of photovoltaic technology has been based on thin films.

This thesis study, as a part of Flamingo PV project in collaboration with HyET company, focuses on development of a-Si:H/nc-Si:H/nc-Si:H triple-junction solar cell on aluminium substrate. The objective is to achieve a stabilised efficiency higher than 14% and an open-circuit voltage in the range of 1.7 and 1.9 V. The implementation of a performing solar device will ultimately move to Roll-to-Roll fabrication on large scale and provide a new competitive product in terms of flexibility, light-weight and cost-effectiveness.

The investigation has been largely built on optical modelling implemented with GENPRO4 software. Initially, the light model and the applied texturing have been validated for the triple junction architecture. An algorithm has been developed to find the thickness of active layers in current matching condition and enhance the spectral utilisation. The design of the solar cell has been analysed by changing layers thickness or materials towards an optimised optical performance.

By conducting a sensitivity analysis on the intrinsic layers thickness, it was found that an alteration of ±5% affects more the photo-generation in the middle sub-cell. Moreover, the analysis carried out on back reflector has shown the silver metal to be more favourable than aluminium. It enhances the reflectivity properties, especially for the bottom sub-cell which is the current limiting junction. Further improvements have been found through the inclusion of an encapsulant at the front side. The embedding of the triple-junction solar cell with a stack of anti-reflective coatings increases the light trapping above 4% on average, improving the photo-generated current density by 0.5 mA/cm^2 in each of the intrinsic layers.

Several thicknesses combinations have been modelled for current matched active layers, but only some of them resulted to be feasible. This has emerged that the spectral utilisation may achieve 27.3 mA/cm^2 and 28.5 mA/cm^2 with the encapsulant integration. The FTO is currently deposited as front reflector in thin films on Al substrate due to its good opto-electrical properties. However, the front reflector performance may be improved by developing a series of different transparent conductive materials. Alternatively, the FTO material may be replaced by IOH with better transparency property and still high conductivity in the near infra-red region of the solar spectrum.

The optical modelling has been an essential tool to forecast the multi-junction operation in experimental section of this work. The fabrication of thin-film solar cells has been divided into two main research areas: Si-based triple-junction devices on Al substrate and GeSn:H thin-films. For the former, two deposition series have been processed to analyse the enhancement of electrical parameters when the absorber layers are current matched. Furthermore, other elements of IV group besides silicon have been examined to achieve a low energy bandgap alloy and increase the light absorption at long wavelength of light spectrum. The first attempts have been investigated for amorphous and nanocrystalline materials based on germanium and tin with an achievable bandgap energy of 0.9 eV.

To conclude, a comprehensive optical modelling has been developed for Si-based triple-junction device on Al substrate. This aims to provide a potential pathway towards the fabrication of a new and efficient flexible and lightweight solar cell technology.

Acknowledgement

"Life is and will ever remain an equation incapable of solution, but it contains certain known factors."
(Nikola Tesla)

My curiosity and desire to understand the phenomena that surround me have been being certain known factors in my life. Five years ago, I dreamed of becoming an engineer, and now those aspirations are reality. Come to think on it, I reached this point thank to my self-will and all people that supported me in this long journey.

TU Delft University has given me the opportunity to face challenges with support of amazing teachers. Prof. Dr. Arno Smets, I would like to thank you for being an endless well of resources and knowledge. I do not know if this is the end of our collaboration, but there are no words to express my gratitude.

Dr. Gianluca Limodio, you have been the best supervisor that I could have ever wanted. I appreciated your teaching at the academic and professional level, but also your tips for everyday life. Grazie mille.

Dr. Thierry de Vrijer, you managed to push myself beyond my limits as a student. I am really pleased to have joined your research group and contributed actively. And who knows, maybe I will be able to be always on time. A special word of thanks goes to HyET company members and EKL laboratory staff. Your way of working professionally taught me a great deal.

In addition, I would like to turn my heartfelt thanks to people that supported me in daily life. These beloved ones have always reached out and grabbed my hand when I was falling down, but also they have been proud of my personal and academic achievements.

Mamma and Papà, you are my light. I hope to make you proud of me, as I am proud to have parents like you. Giorgia, your freeing love and unconditional support make me a better person. My love is also addressed to all the other members of family that I have not mentioned, but each one of them has a space in my heart.

Andrea, your constructive criticism helps me improve as person and engineer, I have learned things have to be always approached from a different point of view.

Last but not least, a special thank you to old and new friends. In Italian, we say: "Who finds a friend, finds a treasure". And this is completely true. I shared with you successes and failures, laughs and tears, fun and serious moments, love and anger. Because deep down, nothing is beautiful to own unless you have friends to share it with.

Federica Saitta,
Delft, November 2021

Contents

List of Figures

List of Tables

1

Introduction

The photovoltaic panorama has been dominated by crystalline silicon (c-Si) wafers technology for a considerable time: c-Si-based solar cells are high-performing devices in terms of efficiency and well-established manufacture. However, their major drawbacks are the high production costs and the long payback time. Accordingly, new alternative technologies have been investigated, such as thin-film technology, also known as the second generation PV technology. On one hand, the thin-film solar cells may compromise their own market growth due to several hindrances related to high initial manufacturing cost and technological complexity. On the other hand, global energy consumption makes it urgently necessary to boost renewables, and in particular, for the purposes of this thesis project, the research activities in the field of thin-film technology.

One of the main advantages is the potential thickness reduction, where the active layer of thin films is thinner than c-Si layer, the former typically in the range of nanometres up to micrometres. The thin layers allow the cost reduction through low encapsulation and low balance of system expenditures, looking towards a sector based on flexible and semi-transparent solar cells. The flexibility adapts solar cells to several PV scenarios, meaning many different semiconductors can be used which are non-toxic and based on earth-abundant materials. Coupled with the inherent flexibility, weight is another primary benefit: the lightweight feature eases and scales up the processing.

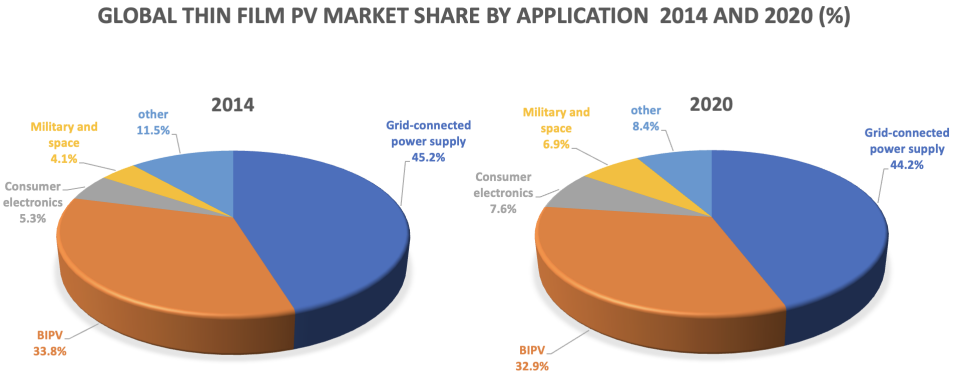

Figure 1.1: The whole thin-film PV market among sectors in 2014 and 2020. Retrieved by [1].

According to Allied Market Research, in 2016 the global thin-film solar cell market was estimated at $11,421 million, with a prospective compound annual growth rate of 19.4% between 2017 and

2023. Wherefore, the expected valuation results to be about $39,512 million by 2023. Despite the fact that the market increase in economic and quantitative terms, the pie chart in Figure 1.1 underlines the market of thin-film solar devices has been dominated by the utility segment towards objective-based cleaner and lower-carbon emission energy systems. The other two main areas of use are the commercial and residential sectors. This technology can apply several PV scenarios from small up to large scale, as for example they can cover electronic, communication and GPS devices, they can find applications in building-integrated photovoltaics (BIPV), for roofs and walls of houses, tanks or any other construction, and furthermore, they may be installed in solar farms or floating/off-shore systems.

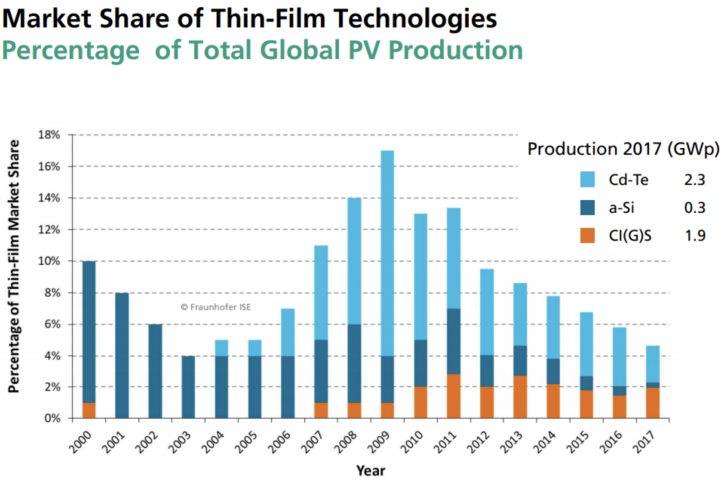

Figure 1.2: The global thin-film PV market among materials from 2000 to 2017 [2].

Figure 1.2shows three main materials implemented in thin-film technology: amorphous silicon (a-Si), cadmium telluride (CdTe), and copper indium gallium selenide (CIGS or CIS if it is gallium-free). The a-Si solar cells are generally used for calculators, although the main drawbacks regard the efficiency loss over time and the low power output. And despite that, it is the oldest thin-film technology with a gained record efficiency of 13.6%. Afterwards, CdTe has been dominating progressively the thin-film solar technology, and for instance, in 2016 world-record CdTe cell efficiency of 22.1% has been achieved by the well-established First Solar company, even if the modules efficiency has been set at 17%. Another market portion involves the application of CIS and CIGS modules, particularly worthy of note is 22.9% CIS cell efficiency record by Solar Frontier and 16.5% flexible CIGS modules efficiency by MiaSolé's [2].

In the thin-film technology framework, the multi-junction cells are embedded and the thin-film silicon-based triple-junctions are largely used. Several combinations are available, e.g. a-Si:H top cell, a-SiGe:H middle cell and nc-Si:H bottom cell configuration has been developed by United Solar Ovonic LLC company, and particular attention has also been paid to a-Si:H/nc-Si:H/nc-Si:H structure. These promising solar cells are extremely challenging in terms of spectral utilisation: sub-cells EQEs shows several overlaps and there is also a complex correlation among thicknesses that requires well-defined light management aspects. Recently, LG Corp company has produced an a-Si:H/nc-Si:H/nc-Si:H solar cell layout by achieving the triple junction record efficiency. The initial efficiency may be found at the value of 16.3%, but due to the light-induced degradation effect for amorphous material, the stabilised record efficiency is 13.4% [7].

1.1. Flamingo PV

The development of flexible and lightweight Si-based triple-junction project has been carried out in Flamingo PV team at TU Delft University, where Flamingo PV is the acronym for "**F**lexible **L**ightweight **A**dvanced **M**aterials **I**n **N**ext **G**eneration **O**f PV". Moreover, this team has a close partnership with HyET Solar department at HyET company (Arnhem, the Netherlands) and both cooperate in the achievement of common goals in the thin-film technology PV sector.

One of the milestones of Flamingo PV project aims to achieve lab-scale flexible a-Si:H/nc-Si:H solar cell (5 cm^2) and module (5x5 cm^2) with 13% as stabilised efficiency. In respect of this one, lab-scale flexible triple-junction PV cell (5 cm^2) and module (5x5 cm^2) with a-Si:H/nc-Si:H/nc-Si:H structure should be developed with a stabilised module efficiency of 14%. Further, there would be the production of 30x30 cm^2 modules area through the cutting-edge roll-to-roll (R2R) technique, managing to reach 12% aperture area stabilized efficiency with 80% production yield. In addition, the industry standard lifetime should be above 80% of the initial performance, verified for more than 35 years. Another important deliverable regards the design and cost model improvements of the bottom cell deposited by the use of PECVD with CAPEX<0.2€/Wp [24].

1.2. R2R technique at HyET Solar

HyET Solar has developed an exclusive and innovative production line based on several roll-to-roll steps for lightweight and flexible thin-film silicon solar cells production. The R2R technique lightens up the PV modules weight to 0.7 kg/m^2 [3].

HyET Solar is based on strategic fundamentals that make possible to manufacture PV modules at large scale, with low cost per W_p and numberless applications. Figure 1.3 summarises the company creed aimed to maximise the technology performance and control. The HyET enhancement looks into the PV modules electrical conversion efficiency which is combined with permanent performing production line and technological innovation. Nevertheless, attention is always directed to new materials research and selection in order to achieve efficient and cost-effective products [3].

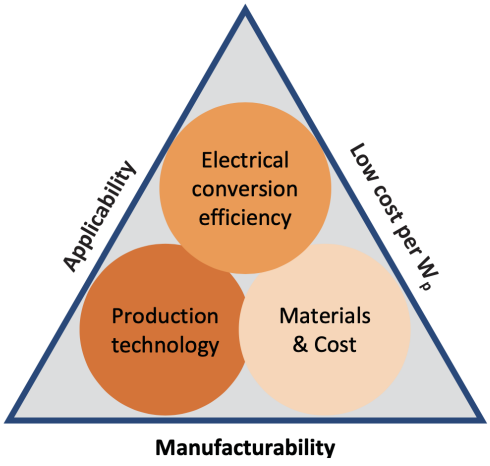

Figure 1.3: HyET Solar bedrocks [3].

Figure 1.4: Thin-film storage tank application (HyET Solar and Vopak partnership) [4].

The process uses a temporary aluminium foil substrate, in this case the Al film is the equivalent of the glass in superstrate configuration for non-flexible applications. Due to the Al foil, the deposition process may reach a higher temperature suited to high-quality transparent conductive oxide (TCO) and silicon layers. The TCO layer is produced with a process powered by atmospheric pressure chemical vapour deposition (APCVD), while a-Si:H or nc-Si:H layers are deposited by R2R plasma enhanced chemical vapour deposition (PECVD). Then, the back contact (ZnO:Al/Al) side is built up through an R2R DC magnetron sputter system, this series is also developed by using laser

scribing and printing methods. The following steps regard the foil lamination and etching: firstly the back contact side sticks on a polymer substrate and then when the permanent foil is laminated, R2R wet chemical etching removes the temporary Al superstrate. Finally, the long roll is cut into PV module size and encapsulated, and later the electrical terminals are linked to the PV structure [25]. Figure 1.4 shows an example of thin-film PV modules (Powerfoil) installation on a Vopak oil storage tank in Rotterdam. On the whole, this application reaches a cost-effective power generation capacity of 1 MW_p [4].

1.3. Thesis objectives and outline

Among FlamingoPV obligations presented in Section 1.1, this work aims to achieve the development of lab-scale flexible 5 cm^2 triple junction silicon solar cell in amorphous silicon/microcrystalline silicon/microcrystalline silicon configuration with 14% stabilised efficiency. Such multi-layer architecture requires a comprehensive optimisation of the cell layering for the energy conversion maximisation. Under this goal, an optical modelling has been used as an effective tool not only for the optimisation of solar cell design, but also for the optical properties and the performance simulation under various conditions. The simulation has provided indispensable results to process the first attempts of triple junction solar cell fabrication. In regard to this, an up-and-coming thin-film structure has been studied in the interest of meeting the main objective, which is a device with high V_{oc} in the range of 1.7–1.9 V.

This thesis project has the following fields of study:

1. Develop an optical model for the triple-junction solar cell and maximise the performance: by processing quality assurance on different textured substrates, considering the effect of the optical properties of layers and providing an evaluation of the best conditions.

2. Reach the current matching condition: by implementing an algorithm and studying the variations and implications in terms of layers thickness and optical parameters.

3. Fabricate triple-junction solar cells with modulated surface texturing on temporary Al foil: by including the texture transfer over the fabrication steps and the device characterisation. It includes the analysis of experimental results and the conformity with the reliable predictions of optical modelling.

The reader will be guided through the undertaken steps to reach these objectives. Chapter 2 collects the preliminary photovoltaic fundamentals and basic knowledge for the understanding of subjects presented in the next chapters. This chapter focuses on optical and electrical parameters, and besides, it provides the working principle and structure of semiconductor devices. Chapter 3 describes the thin-film technology and its main features. A wide discussion has been spent on TCO, amorphous and micro-crystalline materials, and also on deposition steps that are important in developing a multi-junction design. Chapter 4 presents the semiconductor optical modelling that has been implemented via GenPro4 software to investigate the optical properties, the texturing features, the front and back reflector materials. Here, by defining the solar cell architecture and validating the most suitable light model, the analysis has been centred on the current matching conditions and the encapsulant integration to optimise the spectral utilisation. Chapter 5 deals with the experimental processes that took place in the fabrication of triple-junction solar cells, along with the techniques used to characterise the devices. It also dwells upon the inherent challenges of processing hydrogenated germanium-tin, which could be included in the next future devices. Chapter 7 leads to the conclusions of this work, including suggestions for future research in this photovoltaic sector.

2

PV principles

Chapter 2 has investigated some of the PV principles which have been crucial for the understanding of theory related to the development of a silicon-based triple-junction solar cell. Section 2.1 explains the generation, separation and collection of electron-hole pairs during a solar cell operation. Section 2.2 focuses on the photo-generation phenomenon and the solar spectral irradiance. In Section 2.3 the solar semiconductors are differentiated depending on the bandgap configuration. Section 2.4 emphasises the main optical properties of solar cells, whereas Section 2.5 deals with doping concept for the silicon crystalline lattice and Section 2.6 stresses on the significance of p-n junction. The electrical performance and limitations of solar devices are described in Section 2.7 and Section 2.8 respectively.

2.1. Solar cell basic operation

The solar cell working principle relies on the photovoltaic effect: the exposure of specific materials to light makes possible to generate a voltage or current by the excitation of an electron contained within it. The incoming light has to have sufficient energy in order to excite the electron to a higher energy state, commonly called the conduction band. Hence, the electron can be collected and used outside of the generating material. When an electron is energised, it leaves behind a void at its initial position, which is described as a hole or, in other words, a positively charged elementary particle. The hole is collected at a lower energy state that is called valence band, and extracted from the material with an opposite direction in respect to the electron. A visual description has been provided in Figure 2.1, where the process of excitation, transport and collection is described schematically. Moreover, the bandgap energy E_g can be individuated by the energetic difference between the conduction and valence bands.

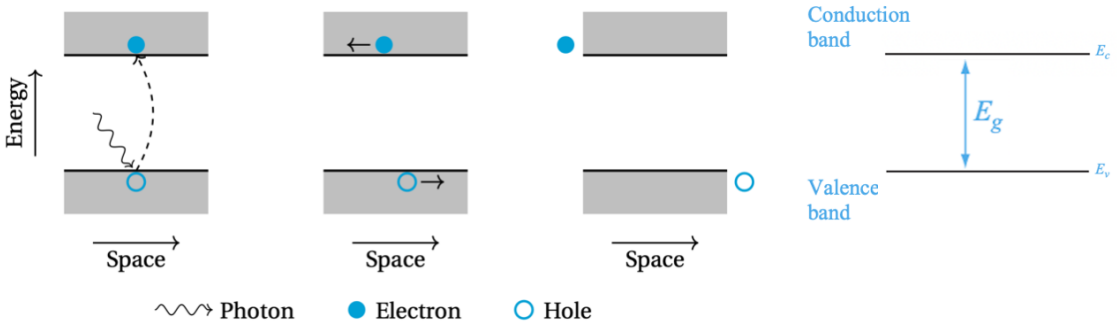

Figure 2.1: Simplified solar cell working principle and bandgap energy diagram [5].

2.2. Photo-generation

Regarding the photovoltaic field, the whole optics is based on the concept of a photon. A photon can be defined as an elementary particle representing a quantum of light or other electromagnetic radiation, usually a null rest mass and charge are associated with it. Since the beginning of the 20th century, the light understanding was revolutionised and it has been considered as clustering of discrete particles with correlated energy [5]. The energy E of a photon is given by:

$$E = h \cdot \nu = h \cdot \frac{c}{\lambda}, \tag{2.1}$$

where h is Planck's constant, c is the speed of light in vacuum, ν is photon frequency and λ is the photon wavelength. The distribution of photons for a given light source can be described by Planck's law when a black body is taken into account at a specific temperature T [26]. In the case of the Sun, this assumption cannot be considered completely true due to the slight Sun emission deviation from the black body behaviour. Additionally, the spectrum changes throughout the atmosphere before reaching the Earth surface. Hence, the Sun modified spectrum is the energy source for solar devices, where AM1.5 solar spectrum has been specified as a reference of the solar radiation reaching the planet's surface. As it is depicted in Figure 2.2, the solar radiation spectrum is highly aleatory in terms of intensity and spectral distribution due to scattering and absorption by atmospheric particles. The visible depressions in the Spectral Irradiance curve represent the atmospheric absorption mostly brought on by carbon dioxide CO_2, water vapour H_2O, oxygen O_2 and ozone O_3 [26], while the light transmitted to the ground can be used for solar devices. The material-specific properties also play a key role for the solar cells absorption and the most common ones have to do with the atomic arrangement, the bandgap or the layers thickness. All these conditions make possible that an incoming photon might have enough energy to be absorbed and thereby produce an electron-hole pair, as described in Figure 2.1 (Section 2.1).

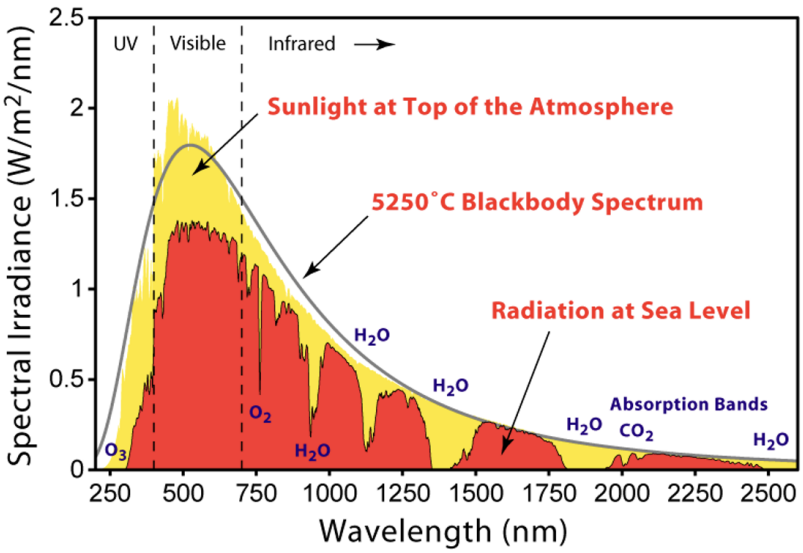

Figure 2.2: Several solar spectra: the Sun spectrum at top of the Atmosphere, the black-body spectrum at 6000 K and the solar radiation at sea level [6].

The electron-hole pair generation can be only reached when the photon energy is higher than E_g of the semiconductor, which would result in the break of atomic bonds. This process is also known as photo-generation and Lambert-Beer's law allows to outline the photons absorption profile through the following formula:

$$\Phi(\lambda, x) = \Phi(\lambda, 0) \cdot e^{-\alpha(\lambda)x}. \tag{2.2}$$

The photon flux $\Phi(\lambda, x)$ as a function of wavelength and position decreases exponentially with the increment of the distance x covered by light in the absorber and the material absorption coefficient α in function of the wavelength λ, while it increases with the growth of the incident photon flux $\Phi(\lambda, 0)$. The $\Phi(\lambda, 0)$ may be formulated via the correlation with the spectral irradiance of the solar irradiation $I_{e\lambda}$ as follows:

$$\Phi(\lambda, 0) = I_{e\lambda} \cdot \frac{\lambda}{hc}. \tag{2.3}$$

Moreover, the association of the absorption $\alpha(\lambda)$ and the photon flux $\Phi(\lambda, x)$ defines the photogeneration rate as:

$$G(\lambda, x) = \alpha(\lambda) \cdot \Phi(\lambda, x), \tag{2.4}$$

by pointing out the integral of $G(\lambda, x)$ over a defined wavelength window or up to a specified depth in a material provides the optical generation rate.

2.3. Direct and Indirect bandgap

Mechanisms, as for instance electron-hole pair generation or recombination, vary among semiconductors on a number of grounds, one major difference is the bandgap configuration that may be distinguished between direct and indirect bandgap. An illustration of the energy-momentum space of electron, such as Figure 2.3, shows two different positions of the conduction and valence bands that may be located in the crystalline lattice. The y-axis indicates the energy state, while the x-axis represents the charge carrier momentum, in other words, the crystal momentum.

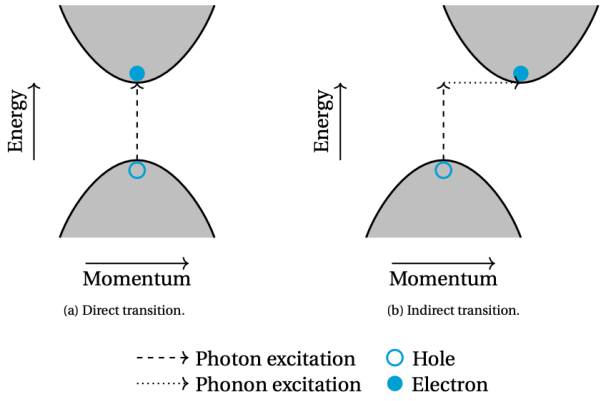

Figure 2.3: Dispersion depiction of direct (a) and indirect (b) bandgap semiconductors [7].

In a material with direct bandgap, the minimum peak of the conduction band is lined up vertically with the maximum peak of the valence band (Figure 2.3a), hence only the energy supplied by photon is needed for the electron excitation without any additional momentum transfer. On the other hand, the indirect bandgap (Figure 2.3b) involves a misalignment between the lowest point of the conduction band and the highest point of the valence band. This means the electron excitation requires the photon energy and the momentum caused by vibrations in the crystal lattice. If the light features some wave and particle properties, the phonon may be seen as responsible for the lattice vibrations with particle connotation. A phonon is the quantum unit of the crystal lattice oscillations and the momentum transfer, therefore, corresponds to the electron absorption of a phonon and its momentum variation accordingly. Considering the involvement of both photon and phonon in the indirect transition, the absorption coefficient for such semiconductors is often significantly lower than for direct bandgap materials.

2.4. Optics

In a semiconductor device, the incident light is partially reflected, while the remaining part may be only transmitted or also absorbed in an absorber material, allowing the charge carriers excitation. Each material might be characterized by two fundamental optical properties: the complex refractive index and the absorption coefficient. The complex index of refraction is given by:

$$\tilde{n} = n + ik, \tag{2.5}$$

where the real part n represents the refractive index. While the imaginary part k is the absorption index related to the absorption coefficient α and the wavelength in vacuum λ by the formula below:

$$k = \frac{\alpha\lambda}{4\pi}. \tag{2.6}$$

Figure 2.4 outlines an example of optics at flat interface, where light is incident on a surface between medium 1 and medium 2. At the interface, the reflected light is scattered with an angle θ_r, which is equal to the incident angle θ_i. The transmitted light is refracted in the medium 2 through an angle θ_t, and it could be related to θ_i by applying Snell's law:

$$\tilde{n}_1 \cdot sin(\theta_i) = \tilde{n}_2 \cdot sin(\theta_t). \tag{2.7}$$

Throughout Fresnel equations is possible to define reflection and transmission amplitudes of the incoming light. Formulas 2.8 and 2.9 stand for the parallel $R_\parallel$ and perpendicular $R_\perp$ polarized components of the reflection coefficient with respect to the plane of incidence.

$$R_\parallel = \left| \frac{\tilde{n}_1 \cdot cos(\theta_t) - \tilde{n}_2 \cdot cos(\theta_i)}{\tilde{n}_1 \cdot cos(\theta_t) + \tilde{n}_2 \cdot cos(\theta_i)} \right|^2, \tag{2.8}$$

$$R_\perp = \left| \frac{\tilde{n}_1 \cdot cos(\theta_i) - \tilde{n}_2 \cdot cos(\theta_t)}{\tilde{n}_1 \cdot cos(\theta_i) + \tilde{n}_2 \cdot cos(\theta_t)} \right|^2. \tag{2.9}$$

If the light is unpolarized, the reflectivity R can be obtained by the mean values of the $R_\parallel$ and $R_\perp$, while if the light comes perpendicularly on the surface ($\theta_i = 0$), the reflection coefficient is given by:

$$R = \left| \frac{\tilde{n}_1 - \tilde{n}_2}{\tilde{n}_1 + \tilde{n}_2} \right|^2. \tag{2.10}$$

Fresnel equations are only valid when both media are non-absorptive ($k_1, k_2 = 0$), hence there is only the real component of refractive indices (n_1, n_2). If the media are absorptive, then $R_\parallel$ and $R_\perp$ are a mere approximation [27], but still provide more precise coefficients instead of a complete denial of the absorption indices [28].

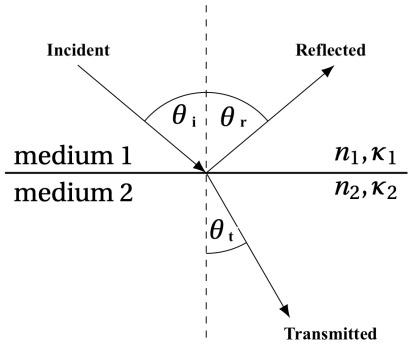

Figure 2.4: Sketch of the incident light: reflected and transmitted components at interface between medium 1 and medium 2, and relevant optical parameters. Retrieved by [8].

2.5. Semiconductor physics

Crystalline silicon (c-Si) solar cell has been taken into account due to its wide applications in the photovoltaic field. In general, semiconductors are materials with conductivity between those of insulators and metals. In the periodic table, semi-conductive elements are identified in group IV and are often combined with elements belonging to III and V groups in order to alloy semiconductor materials.

Each Si atom corresponds to a quantised energy level where the located electrons can be energised. This allows Si atoms to bind with other neighbouring atoms and organise in a periodic arrangement, commonly referred to as diamond structure. The covalent bonds characterise this diamond structure, where a pair of electrons is shared by two atoms and are in the outer atoms shell. This turns out into interaction between the possible states that electrons can be in, and hence a quasi-continuous distribution of allowed states in the conduction and valence bands. At singular atomic level, these bonds are strong, meaning a large amount of energy is required to break them; while at the inter-molecular level, the forces are weak, less energy is needed for the molecules separation from each other [10].

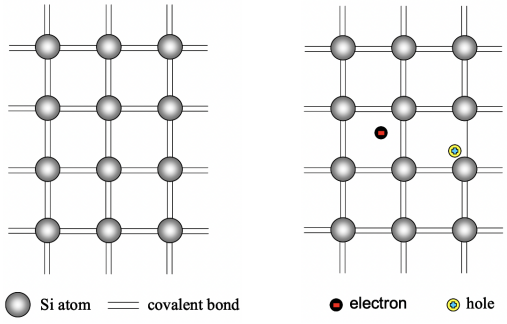

(a) Ideal bonding structure (0 K)

(b) Mobile electron-hole pair by a bond rupture

Figure 2.5: The bonding model of c-Si diamaond lattice [9].

Figure 2.5 represents a two-dimensional bonding model for c-Si diamond structure. If Si crystalline lattice is at temperature of 0°K, then no free electrons are present in the lattice, because all of them are involved in forming covalent bonds, as illustrated in Figure 2.5a. However, it is an unrealistic situation: the temperature is assumed to be always higher than 0 K, where thermal energy is absorbed and leads to the bonds breaking apart. Figure 2.5b underlines a covalent bond break, where an electron is able to move freely leaving a hole behind. When the free positive and negative charge carriers are at the same concentration, the semiconductor has an intrinsic carrier concentration [7].

An intrinsic c-Si may be favourable in terms of purity and homogeneity, but on the other hand, the impurities introduction is one of the main features in the crystalline lattice for the semiconductor operation. The insertion of other atoms is called doping and enables to shift the balance of the electron-hole concentration as shown in Figure 2.6.

Doping produces:

a) n-type material by increasing the number of available electrons. An atom with more valence electrons than Si is incorporated, elements from group V, such as phosphorus (P), are usually used as electrons donors (Figure 2.6a).

b) p-type material by increasing the number of accessible holes. An atom with fewer valence electrons than Si vacates a hole, elements from group III, such as boron (P), are usually used as acceptors (Figure. 2.6b).

In n-type semiconductors, the majority carriers are electrons (donors) and the minority carriers are holes, while the majority carriers are holes (acceptors) and the minority carriers are electrons for p-type semiconductors.

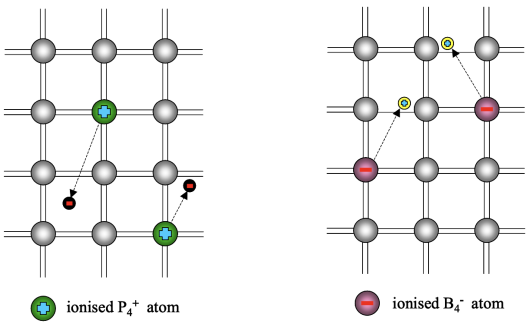

(a) P atoms replace Si atoms (n-type configuration)

(b) B atoms replace Si atoms (p-type configuration)

Figure 2.6: The doping process through the bi-dimensional bonding model [9].

Finally, the electrochemical potential, otherwise known as Fermi energy level E_F, is defined as the highest occupied energy level by valence electrons and is between the conduction and valence bands for intrinsic semiconductors. For n-doped materials, the E_F is localised closer to conduction band, while for p-doped materials, the E_F is shifted down to the valence band. The higher the donors or acceptors concentration is, the closer the Fermi level will be to the E_C or E_V respectively.

2.6. *p-n* junction

When a p-type semiconductor is joined with a n-type one, there is a large difference in terms of electron-hole concentration at first and this causes an electron current diffusion from n-type to p-type material and, by contrast, a hole current diffusion from p-type to n-type material. In addition, the thus metallurgical junction between the two regions is almost depleted of mobile charge carriers and, for this reason, it is more commonly called space-charge or depleted region, outside of which quasi-neutral spaces are located due to the conservation of the charge neutrality.

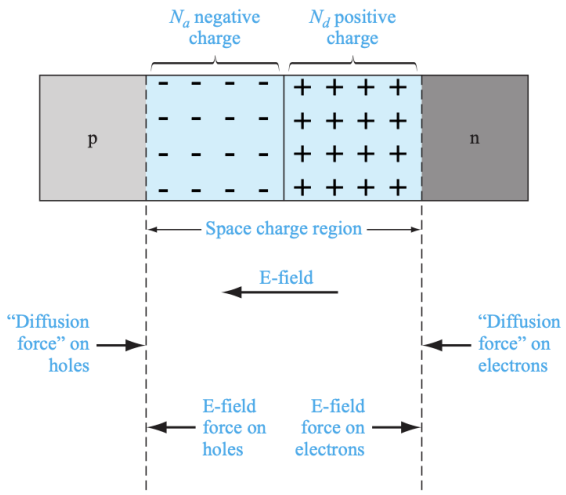

Figure 2.7: A p-n metallurgical junction and rough outline of involved forces [10].

Figure 2.7 provides a schematic representation of a *p-n* junction structure with its main futures for the solar cell functioning. A build-up charge can be found in the adjacent area to the interface: a majority of positive charge at *n*-side and a majority of negative charge at *p*-side. As a consequence, an electric field (E-field) occurs in the depleted space and points to *p*-type semiconductor. The *p-n* junction reaches the equilibrium when the diffusion force provided, by the concentration gradient, and the drift force, given by E-field, are balanced without the influence of any additional external forces.

The concentration of the charge carriers is directly connected with the width of the depletion region, under the assumption that the electric field is confined only to the space-charge region, a relation between the concentration of donors and acceptors (N_d, N_a), and the width of the *p-n* sides of the depleted area (x_p, x_n) can be found as follows:

$$N_a \cdot x_p = N_d \cdot x_n. \tag{2.11}$$

The *p-n* junction has also been analysed through a band diagram as in Figure 2.8: the energy levels are shown prior to and following the contact. In Figure 2.8a the *p*-type material has a prevalent acceptors concentration N_a and the *n*-type material meets a prevalent donors concentration N_d, as also shown by the E_F shifting to E_V and E_C respectively. If the two sides are connected and the thermal equilibrium is reached, then the band diagram in Figure 2.8b is obtained with a constant energy Fermi level across the junction. Moreover, the mobile charge carriers set up a potential barrier in the space-charge region. The bands are bended due to the electric field which generates an electrostatic potential between the edges. This process is known as band bending, where the change in carriers concentration is counterbalanced by the electrostatic-potential variation [7].

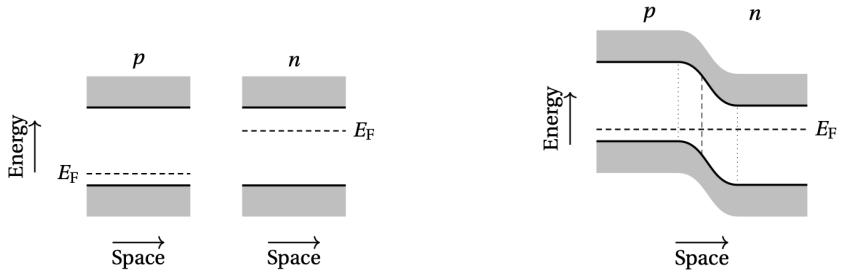

(a) Separate *p*/*n*-doped sides (b) *p*/*n* junction

Figure 2.8: The band diagram of a *p*/*n* junction a) before and b) after the contact [10].

In this regard, it is important to mention the solar device always needs an external and closing electric circuit. The charge carriers collection follows what has already been explained in Section 2.1 and depicted in Figure 2.1. A metal-semiconductor junction is normally involved as back contact and nearly always as front contact in the solar cell architecture. These contacts have to be conductive materials with low resistance. When the metal-semiconductor structure has a low resistance compared to the bulk resistance in the semiconductor, the contacts can be described as ohmic contacts.

In general, in a metal-semiconductor contact, the Fermi energy level has to be constant by leading to a gap between the E_F and the semiconductor E_C (*n*-type semiconductor taken as the benchmark) [7]. If the semiconductor doping concentration is low, the metal contact resistance can be decreased by keeping the barrier height as low as possible; whereas if the semiconductor is highly doped, the width of the depletion region is reduced. This results in the quantum-mechanic tunnelling of current, where the contact resistance decreases by increasing the charge carrier concentration.

2.7. Solar cell performance: external parameters

In order to determine the solar cell performance, some parameters with their respective definition have been discussed in this section. Two of the main features are the current-voltage characteristic (J-V curve) and the external quantum efficiency (EQE).

The electrical characteristic of *p-n* junction can be rounded to the one of diode without illumination. Current I as function of voltage V follows the Shockley diode equation:

$$I = I_0 \left[e^{\frac{qV}{nk_BT}} - 1 \right]. \tag{2.12}$$

Here, I_0 is the reverse bias saturation current, q is the elementary charge, k_B is the Boltzmann constant, T the temperature and n is the ideality factor ($1<n<2$ depending on the dominant recombination mechanism). When the light shines on the cell, a photon generated current I_{ph} and additional resistances have to be included in Equation 2.12 due to the non-ideal operation, resulting in:

$$I = I_{ph} - I_0 \left[e^{\frac{qV}{nk_BT}} - 1 \right] - \frac{V + IR_s}{R_{sh}}, \tag{2.13}$$

R_s is the series resistance and represents the total contact resistance, while R_{sh} includes manufacturing defects that bring to an alternative circuit for the current flow and so as result a performance losses [29]. An equivalent electric circuit such as Figure 2.9 gives a detailed graphical view of solar cell operation according to the external parameters.

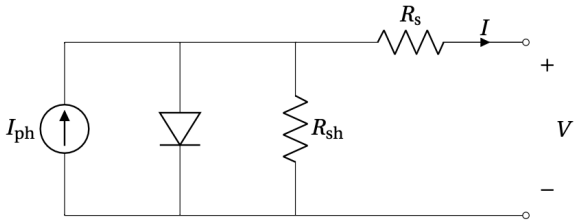

Figure 2.9: The equivalent circuit of a solar cell with electrical components. Inspired by [7].

Another important solar cell indicator is the open-circuit voltage V_{oc} obtained by applying a hypothetical infinite resistance at terminals of the device. As opposed, the short circuit current I_{sc} may be found when an infinitive resistance is included at terminals. In Figure 2.10 the red curve depicts the possible current-voltage combinations for the solar cell functioning, by multiplying I and V is possible to deduce the delivered power P (blue function). The V_{oc} and I_{sc} are the maximum voltage and current values provided by the I-V curve, but both result in a null power: I and V are equal to zero at $V=V_{oc}$ and $I=I_{sc}$ respectively. The desirable working condition is at the maximum power point, where I and V are the highest and therefore, the largest amount of power can be achieved.

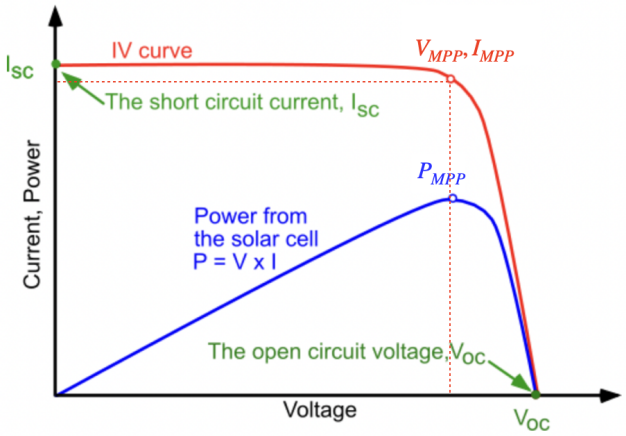

Figure 2.10: I-V and P curves for a solar device under illumination [11].

The maximum power generated by the device, the open-circuit voltage and the short circuit current may be related to each other by the fill factor parameter:

$$FF = \frac{I_{MPP} \cdot V_{MPP}}{I_{sc} \cdot V_{oc}}. \tag{2.14}$$

Alongside the fill factor, the conversion efficiency is a key parameter that allows quantifying the amount of Solar Irradiance (I_{in}=1000 W/m^2 under STC) is converted into power delivered by the solar cell. Equation 2.15 defines the efficiency η as the ratio between the power at the maximum power point and the incident power:

$$\eta = \frac{P_{MPP}}{I_{in}} = \frac{J_{MPP} \cdot V_{MPP}}{I_{in}} = \frac{J_{sc} \cdot V_{oc} \cdot FF}{I_{in}}, \tag{2.15}$$

instead of the current I, the current density parameter J (A/m^2) has been used for an area-independent estimation.

Furthermore, the EQE is a fundamental external parameter to quantify optical and electrical losses (as explained in further detail in Section 2.8). The external quantum efficiency may be seen as the ratio between the collected amount of electron-hole pair and the total number of incoming photons at a certain wavelength. By integrating the EQE over the photon flux $\Phi(\lambda)$ in a defined wavelength range, the short circuit current is specified as:

$$I_{sc} = \int_{\lambda_a}^{\lambda_b} EQE(\lambda)\Phi(\lambda)d(\lambda). \tag{2.16}$$

2.8. Limiting factors and losses

Equation 2.15 is constrained by several factors that do not allow to convert a significant amount of light incoming in the solar cell into available energy. In this section, several limiting effects have been briefly explained to get into understanding of the real solar devices performance.

As already presented in Section 2.1, each semiconductor is characterized by a specific energy bandgap depending on the used material. If an ingoing photon has less E_g than the semiconductor, the photon can not be absorbed and therefore the electron can not be excited. This effect limits the photon energy that may be potentially turned into electrical energy. It is worth noting that as the material E_g increases, as low the photon absorption is in terms of wavelength.

On the other hand, it occurs electrons have higher E_g than the semiconductor. In this situation, the absorbed photon has such energy to excite the electron above the edge of the conduction band.

The free-electron can easily interact with other atoms in the crystalline structure, resulting in energy loss to phonons and therefore lattice vibrations. As consequence, the electron returns to the minimum level of E_c and achieves a stable position. This process is also similar for the hole in the E_v and goes by the name of thermalisation: chemical energy is converted into thermal energy by allowing the charge carriers to escape to a non-allowed energy state [30].

In addition to the limited photon energy and thermalisation phenomena, recombination mechanisms might be present in the material bulk. In the direct bandgap materials, the radiative recombination is band-to-band transition of an electron from E_c to E_v with a photon emission, in other words, it is the opposite process of photon absorption. This effect thus can not characterise the c-Si due to the additional phonon required for the process in respect to the momentum conservation [31], as discussed in Section 2.3.

If the radiative mechanism characterises the direct bandgap semiconductors, non-radiative recombination, also known as Shockley-Read-Hall is mainly involved in materials with indirect bandgap. It may occur in the presence of some defects that generate energy states (trap states) between E_c to E_v. Hence, these new available recombination centres allow easily the capture of electrons and holes and therefore release energy to phonons [32].

Alternatively, indirect bandgap or highly doped semiconductors may be involved in the Auger recombination, whose three particles participate in this mechanism. After the electron-hole recombination, there is a transfer of energy to a third charge carrier that dissipates as phonons to the lattice, which then results in thermal energy loss [7].

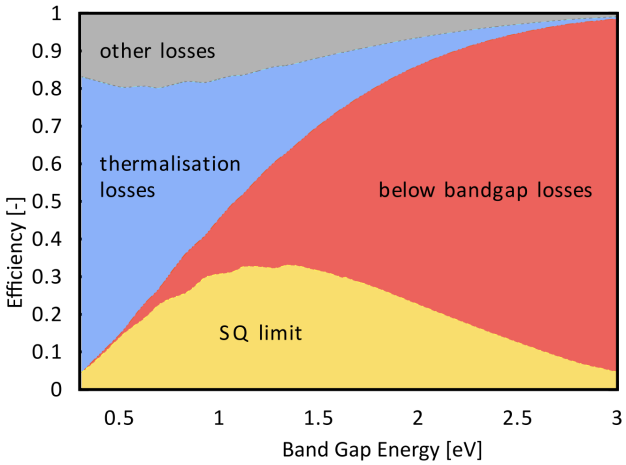

Figure 2.11: The Shockley-Queisser limit and main losses under STC [7].

Further to this bulk recombination mechanism, a key role is also played by surface recombination. In general, there are several unpaired valence electrons at the silicon surface and this results in undesired dangling bonds. The surface defects induce as Shockley-Read-Hall recombination.

In photovoltaic literature, the Shockley-Queisser (SQ) is often mentioned as the theoretical limit for direct bandgap solar cells. This limit does not apply if several recombination mechanisms take part in the solar cells, and hence the mere presence of radiative recombination has been assumed as a simplification. In Figure 2.11 the main losses are the spectral mismatch and thermalisation losses, besides the depicted red and blue area, there are other losses as voltage losses or fill factor losses. Although the Shockley-Queisser limit neglects optical losses, they have to take into consideration for a realistic assessment of a solar device. This aspect has been covered with a broad discussion in Chapter 4.

3

Thin-film technology

Chapter 3 goes through the thin-film technology increasingly being used in the field of photovoltaics. The thin-film solar cells follow a well-defined structure: the active layers are sandwiched within a transparent conductive oxide (TCO) layer and an electric back contact. The importance of TCO has been discussed in Section 3.1, where the difference between superstrate and substrate configuration, and the opto-electrical properties are mainly explained. Section 3.2 has paid attention to amorphous silicon materials by examining the density of states and Staebler-Wronski effect, whereas Section 3.3 investigates the microcrystalline phase for silicon-based materials largely employed in thin-film as well as amorphous ones. Subsequently, the design of multi-junction solar cells has been explored in Section 3.4. In the last part of Chapter 3 the reader has been guided into the thin-films deposition process (Section 3.5), in particular, the plasma enhanced chemical vapour deposition and physical vapour deposition are presented in Section 3.6 and Section 3.7 respectively.

3.1. Transparent conducting oxide (TCO)

The TCO can be made by inorganic or organic materials, and due to its function, high conductivity and high transparency have to be reached in the active wavelength range. Typical materials are aluminium-doped zinc oxide ZnO:Al (AZO), fluor-doped tin oxide SnO_2:F (FTO), indium tin oxide (ITO), which is a combination of In_2O_3 and SnO_2, and hydrogen-doped indium oxide In_2O_3:H (IOH) [7]. There are overall two basic cell configurations that require TCO with specific features. A solar cell may have in "superstrate" or "substrate" configuration, where the main difference is played by the deposition order.

3.1.1. Glass substrates and the *p-i-n* (superstrate configuration)

Normally, in this solar cell configuration, a glass is used with the function of transparent superstrate as thoroughly explained in Figure 3.1a. The semiconductor junction and metal electrode are deposited on top of the glass superstrate, meaning the layer that is first passed by the incident light is also deposited as first in the solar cell. In this case, the *p-i-n* deposition sequence is employed for a-Si:H and nc-Si:H solar cells. The glass-TCO combination is followed by *p*-layer as the first semiconductor layer. It has to be thin (in the order of 10 nm) and with a low absorption coefficient. After which, the light can pass through the thicker *i*-layer where the light absorption occurs and it ultimately crosses the thin *n*-layer (about 20 nm). If the light is not absorbed yet, it reaches the back contact part, where it is important to reflect back into the intrinsic layer the light amount not absorbed previously. At the back contact, a suitable configuration would be thin TCO layer and thick metallic layer, such as aluminium (Al) or silver (Ag). It allows high optical properties in terms of reflectivity and high electrical conductivity.

3.1.2. Opaque substrates and the *n-i-p* (substrate configuration)

This alternative solution involves the substrate as back contact or, in other words, the back contact is deposited in the substrate as showed in Figure 3.1b. Consequently, no light passes through the substrate and light first encounters the layer that is deposited last. The substrates are, in general, opaque or transparent, depending on what material is used. In this configuration (substrate and *n-i-p* cells) the light goes through the *p*-layer as first and the top TCO layer as last. Examples of common materials are stainless steel, polyimide or PET (polyethylene terephtalate). On the one hand, a drawback might be an undesirable low deposition temperature such as for the plastic substrates [33]. On the other hand, an example of promising application opportunities for polyimide or PET is the option to combine the roll-to-roll (R2R) production and monolithic cells series connection to the module.

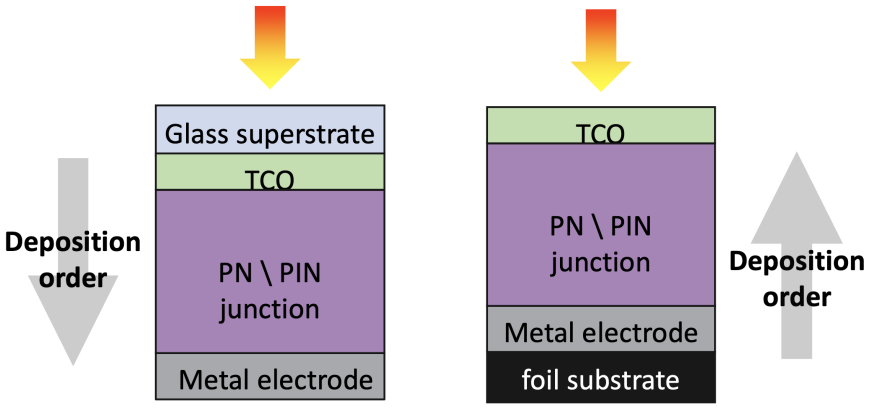

(a) Superstrate configuration (b) Substrate configuration

Figure 3.1: TCO layer as front contact in two solar cell configurations.

3.1.3. Electrical and Optical TCO properties

The electrical properties can be expressed through the sheet resistance of the TCO film:

$$R_{sheet} = \frac{\rho}{d}, \tag{3.1}$$

where ρ and d are the material resistivity and thickness respectively. The R_{sheet} plays a key role when a series connection of cells is considered for a solar module, hence it is additive and gives rise to the electrical power losses. Two different approaches may be followed in order to minimise R_{sheet}: the first is primarily aimed to reduce the material specific resistivity by increasing the carrier mobility; the second is more related to the thickness increase with the TCO absorbance rise as a drawback.

Other important TCO features are related to optical functions. Firstly, the TCO/*p*-layer interface is affected by a reduction of the reflection due to its roughness of sub-wavelength feature sizes, it produces a graded index of refraction. This effect is called anti-reflection effect (AR-effect) and counts for the entire spectral range of the incident light [34]. It is also important to mention the TCO light scattering and light trapping improve the total internal reflection and thus, the light absorption in active absorber layers. The enhancement can be reached through a high reflection at the back contact and it enables higher short-circuit current densities J_{sc}: this is of particular relevance to nc-Si:H cells. A low refractive index inter-layer, such as ZnQ, is typically required thus allowing an improvement in the light trapping of the long-wavelength portion [33].

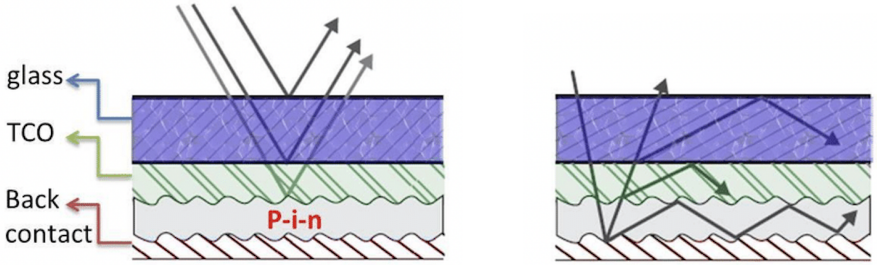

(a) Index grading at TCO/*p*-layer interface (full spectral range)

(b) Light trapping and index grading at rear contact (long-wavelength spectral range)

Figure 3.2: TCO textured-related effects with glass/TCO/*p*-*i*-*n*/back contact design [12].

Therefore, an adequate TCO surface texture with feature sizes similar to the wavelengths will make it possible to achieve both objectives. As Figure 3.2a depicts, the index grading diversifies the reflectances at the front TCO/*p*-layer interface for short-wavelength; while Figure 3.2b shows long-wavelengths penetrate to the back contact, in this case, index grading and light trapping are responsible for the reflectance reduction.

3.2. Amorphous silicon

This section has been mainly focused on amorphous silicon among amorphous materials due to its large application in thin-film technology. If c-Si material owns a well structured and oriented lattice as already explained in Section 2.5, amorphous alloys have a continuous random network (CRN) as shown in Figure 3.3. Looking at the atomic unit, it is possible to spot some Si atoms devoid of four covalent bonds, hence the valence electrons develop dangling bonds. This effect is similar to the surface recombination discussed in Section 2.8, where unpassivated electrons are arranged on the silicon surface. Generally, this material is referred to as hydrogenated amorphous silicon (a-Si:H), in this case, hydrogen ":H" plays a key role in passivating some of the unbound electrons in the silicon structure. Having pure a-Si would mean unaccepted high defect density (over 10^{19} cm^{-3}) [35].

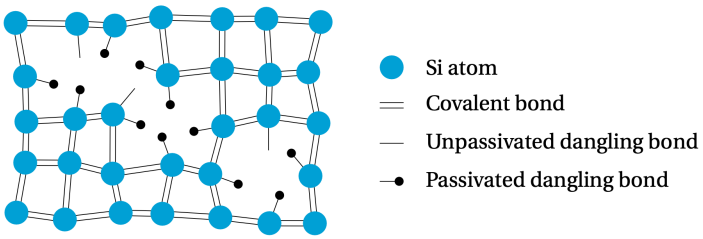

Figure 3.3: Amorphous silicon atomic structure [13].

3.2.1. Density of states

The passivisation of dangling bonds in a-Si:H allows to identify the conduction and valence band otherwise impossible in a-Si configuration, although the edge of the bands is undefined since the lattice is irregular. As represented in Figure 3.4, there is an extension of the conduction and valence bands or so-called tail states in the forbidden energy gap. In terms of energy state, they are not well localised, which means holes and electrons behave as free charge carriers in VB tail and CB tail respectively. The carriers are in low amounts compared to the ones in the non-localised states. An energy gap can not be associated with a-Si:H as a result of the continuity state, while it is more preferable to attribute the mobility gap (E_{mob}) term. The (E_{mob}) scales with the deposition condi-

tions, in particular, lower temperature and higher hydrogen concentration are both responsible in the mobility gap increase. A typical value for the a-Si:H mobility gap is 1.75 eV.

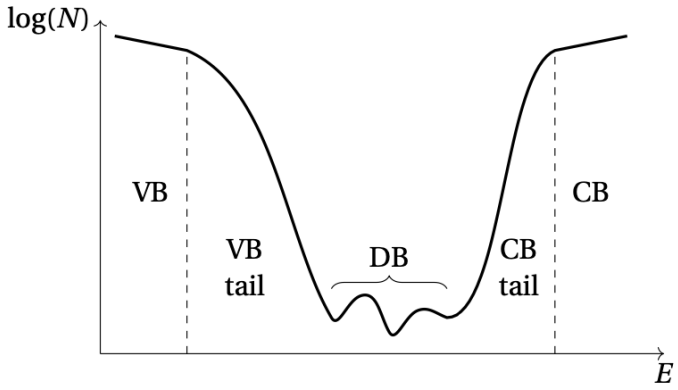

Figure 3.4: The a-Si:H density of states graph [14].

3.2.2. Light-induced degradation: Staebler-Wronski effect

The most challenging aspect for amorphous materials is the light-induced degradation, also known as Staebler-Wronski effect (SWE). Due to this effect, the dangling bonds function as recombination centres in the lattice and as consequence, there is a reduction of the charge carriers mobility. The more the atomic structure is defected, the grater electron-hole pairs recombination will be, resulting in decreased performance of amorphous solar devices. However, the annealing procedure allows the passivation of dangling bonds in a temperature range between 150°C to 200°C [36]. If the a-Si device is exposed to light for a thousand hours, then a reduction of 10-15% of the initial efficiency will occur [7]; on account of the degradation effect, a-Si:H solar cells require a solid distinction between initial and stabilised efficiency. The SWE may be shortened through two main strategies: the former is the temperature deposition increase, the latter is the hydrogen dilution raise [37], as detailed in Subsection 3.6.1 .

3.3. Microcrystalline silicon

Microcrystalline or nanocrystalline materials are between the well-organised structure of c-Si and the disordered one of a-Si. Figure 3.5 sketches the μc-Si phase, featuring a varied number of crystalline grains placed within amorphous tissue and some random voids where there is no presence of the material. On the left, the pure crystalline phase is represented and characterised by several cracks and pores, while on the right there is the opposite case characterised by the amorphous state. Hence, μc-Si material is a mixed phase of both and its grains can vary in a range of nanometers up to microns [37]. Usually, μc-Si is hydrogenated: hydrogen allows the passivation of dangling bonds and even more important, less hydrogen concentration results in a continuous amorphous structure instead of a microcrystalline one. Therefore, it is more appropriate to refer to the microcrystalline hydrogenated silicon (μc-Si:H).

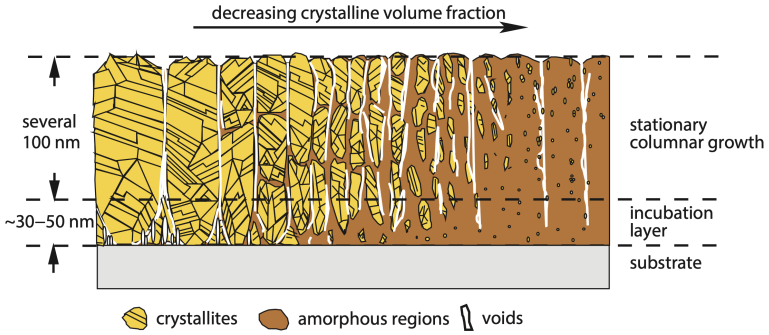

Figure 3.5: Thin-film phases: c-Si, μm-Si and a-Si (from left to right) [7].

3.4. Multi-junction design

Section 3.2 and Section 3.3 underline the disordered structure of hydrogenated a-Si:H and µc-Si. Due to the presence of free valence electrons, the lifetime of charge carriers and the diffusion length are limited, meaning thick layers are not favourable. A *p*-*n* junction has been discussed as the most suitable structure for c-Si solar cells in Section 2.6 (Chapter 2). However, amorphous and nanocrystalline materials are normally based on *p*-*i*-*n* junction, in which the *i*-layer is intrinsic without any doping atoms and with a thickness that can vary between hundreds of nanometers up to microns. On the other hand, the *p*-layer and *n*-layer are very thin (about 10-20 nm [7]), and between them, a built-in electric field can be found within the intrinsic layer. Under the conditions of darkness and thermal equilibrium, the energy Fermi level is aligned: closer to the conduction band at *n*-doped side and nearby the valence band at *p*-doped side. Therefore, a slop is present in the *i*-layer in order to satisfy the E_F across the junction, in which electrons come down towards the *n*-layer and holes move up to the *p*-layer. Contrary to *p*-*n* junction, the main transport mechanism is caused by the drift force resulting from the electric field. On the other side, the diffusion forces are dominant at the *n*-layer and *p*-layer, where the majority carriers are electrons and holes respectively. Given a poor diffusion length, the doped layers have to be fabricated thinner in any solar cell device.

Furthermore, considering the solar cell design is advisable to avoid the amorphous silicon in the *p*-doped and *n*-doped layers because a bandgap of 1.75 eV has a low utilisation due to recombination mechanisms and its bandgap energy structure. For that reason, materials such as silicon carbide or silicon oxides with higher bandgap are introduced in the architecture. They allow a better absorption at short wavelengths (blue part of the light spectrum) and hence, less parasitic absorption. This optical loss does not allow the generation of the electron-hole pair and thus reduces the solar cell photocurrent [38]. On the other hand, µc-Si material has a lower bandgap than the one of a-Si and may be employed for the spectral utilisation between 750 nm and 950 nm. However, nanocrystalline layers have a thickness in the range of 1-3 µm, they are thicker than amorphous films because of the indirect bandgap [7].

The best approach for optimised spectral utilisation is the multi-junction structure for solar devices. In many applications, a micromorph silicon solar cell or so-called tandem solar device is used and consists of a-Si:H and µc-Si:H connection, providing a double-junction structure. Here, a-Si:H is the top cell and absorbs high energetic photons at short wavelengths, while µc-Si:H becomes the bottom cell and reaches low energetic photons on account of its low bandgap.

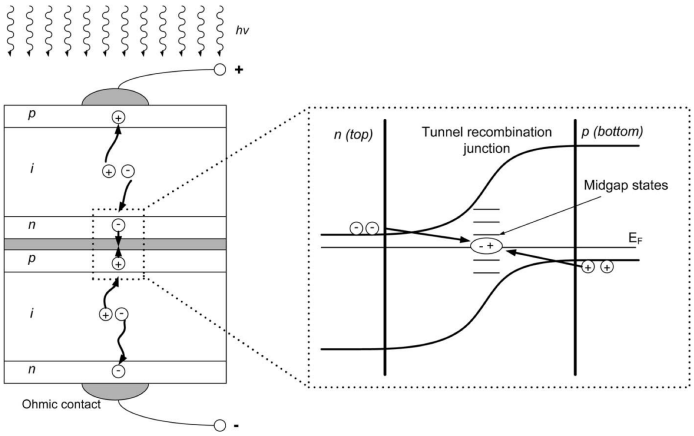

Figure 3.6: Tandem solar cell draft in *p*-*i*-*n*/*p*-*i*-*n* configuration and band diagram at top/middle cells junction [15].

In a multi-junction cell, the tunnel recombination junction TRJ is located at the interface between the *n*-type layer of the top cell and the *p*-type layer of the adjacent bottom cell. Here, electrons from *n* (top) and holes from *p* (bottom) recombine as illustrated in Figure 3.6, thereby enabling the current flow throughout the cell. The tunnelling process allows transporting the charge carriers via the TRJ, in which electrons and holes can easily overcome the potential barrier and recombine. This is also facilitated by a high concentration of states and thin *n*-/*p*-layers [14].

3.5. Thin-film silicon deposition

The thin-film silicon solar cells fabrication is a complex and well-structured process subdivided into several steps, the production process in the Else Kooi Laboratory (Delft, the Netherlands) has been taken as an explanatory example of the work carried out. Each kind of deposition requires a preliminary cleaning process in an ultrasonic cleaning bath where a potential shunt may occur between the front and the back contacts.

The following step involves the deposition of the TCO layers, FTO and ZnO:Al generally deposited through the sputtering process. For ZnO:Al a craters texturing structure is achieved by etching with strong acids and is remarkable for light scattering. When the samples have already a TCO layer (e.g. SnO_2 with a pyramidal structure), a ZnO:Al buffer layer is deposited on top to prevent potential material reductions during the deposition [39].

Therefore the thin-film silicon layers are processed in a multi-chamber setup in which each layer is deposited in a specific chamber in order to avoid contamination and preserve the quality of layers. In brief, the sample is mounted on a suitable holder and placed in the load lock. When the load lock is under low pressure or otherwise defined as in a vacuum, the substrate is moved in the possessing chambers through a robot arm that picks and places it mechanically. This procedure safeguards the processing chambers by undesired particles in the ambient air.

The thin-film silicon materials are normally deposited through plasma-enhanced chemical vapour deposition (PECVD), where different precursor gasses are brought into the chamber involved for the deposition. Further details about the deposition steps and process conditions have been discussed in Section 3.6.

After PECVD deposition, the sample is covered with a mask, which defines the areas onto which the metallic contacts have to be deposited. In EKL laboratory, materials such as silver (Ag) or aluminium (Al) may be deposited through the evaporation technique. Little pieces of the material are placed in a bucket that is heated by a very high current that flows through it. The evaporated particles can move freely through a vacuum until they hit the sample, allowing the layer deposition onto the uncovered squares. This process has been explained in more detail in Section 3.7.

3.6. Plasma enhanced chemical vapour deposition (PECVD)

The layers for thin-film devices are often deposited by using a vacuum technique that involves plasma as an ionised gas state which is neutral at macroscopic level [17]. Several parameters such as temperature, pressure, power coupled into the plasma or silane (SiH_4) gas flow rates play a key role during the deposition process. As shown schematically in Figure 3.7, the substrate holder that hosts the sample is heated to 200°C or even higher temperatures, and placed between the plates. This facilitates the process which otherwise could not take place at lower temperatures, as for instance at the ambient one.

SiH_4 or a dilution with hydrogen (H_2) are used as precursor gases for Si films deposition. Firstly, silane is injected into the chamber, and then its dissociation into Si_xH_y type of radicals is led by an oscillating electric field. A radio frequency (RF) or very high frequency (VHF) bias voltage is applied between two electrodes allowing plasma generation, the conversion occurs more specifically at 13.56 MHz for RF signal or at 50–80 MHz for VHF signal. The radicals, such as SiH_3, SiH_2 or SiH, consequently react with the substrate and enable the layer growth. Among these radicals, the SiH_3 has the longest lifetime and thereby the highest concentration in the chamber [40].

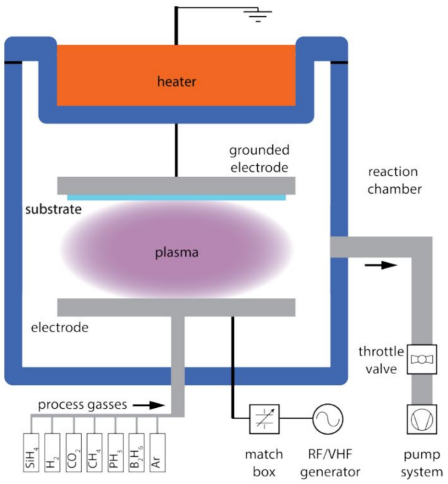

Figure 3.7: PECVD chamber layout [16].

While the plasma bulk is neutral with regard to charge, a space charge region, generally referred to as sheath boundary, is located between the substrate and the plasma as depicted with light-blue colour in Figure 3.7. The sheath acts as a selective cover, accelerating the positive ions to the substrate and confining the electrons, negative ions and powders inside the plasma. The sheath furthermore allows the diffusion of neutral radicals alsothrough the boundary to the substrate [17]. This process has been illustrated in Figure 3.8 through an outline diagram.

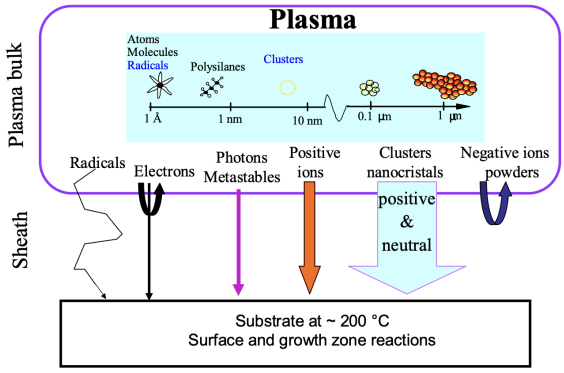

Figure 3.8: Reactive species in the plasma with their respective selectivity through the sheath [17].

Most of the samples mentioned in the experimental sections of this thesis have been deposited by using a cluster tool called AMIGO from Elettrorava (Figure 3.9) with six chambers for Si deposition. AMIGO's chambers are largely dedicated to *p*-doped, *n*-doped, intrinsic a-Si:H, intrinsic μc-Si:H depositions. Additional chambers are reserved for special silicon alloys like silicon carbides or nitrides, and one chamber for AZO sputtering.

Figure 3.9: AMIGO PECVD machine (EKL laboratory).

It is of utmost importance to point out that the quality of deposition is determined by the regulation of numerous parameters in AMIGO. For instance, a power increase allows the electric field to split easily the gas precursors, resulting in higher ions formation and higher deposition rate. On the other hand, higher ions motion results in more bombardment of the thin film deposition which is potentially damaging. A conclusive approach involves the excitation frequency increase, which ensues the sheath boundary decrease and the ions excitation reduction [33].

Another issue is the substrate temperature directly affects the defect states in the deposited layer and determines the bonding of SiH_3 at the layers surface, which mainly influences the defect concentration through surface reaction rates. In this case, pressure is fundamental to determine the inelastic collisions and reduce the ions momentum in the plasma which has direct impacts on both optical and electrical properties of the deposited silicon layers. The gases inflow determines the number of entities to be ionised (whether surplus or deficit) for deposition and thus the deposited material phase. Therefore, the power increase is not sufficient to boost the deposition rate, but also requires the silane flow raise, which will, in turn, regulate the type of material deposited [17]. Thus, the points mentioned above underline the mutual dependence of parameters and the relevance of fine-tuning to achieve device grade deposition.

3.6.1. a-Si:H growth

As previously mentioned in Subsection 3.2.1, some of the deposition parameters influence the growth of a-Si:H material. The main responsible for a-Si:H deposition is the silane, which may contribute to SiH_4 formation by breaking hydrogen bonds at the lattice surface and leaving an undesired dangling bond. Alternatively, SiH_3 may interact with the dangling bonds by increasing the amorphous layer deposition. For reasons of clarity, only part of the incoming radicals interact with the film surface as explained above, another amount is merely reflected backwards into plasma [41].

3.6.2. µc-Si:H growth

Microcrystalline film deposition is facilitated by the input radicals, in particular SiH_4 dilution with the precursor gas H_2. The method for a-Si dangling bonds passivation (Subsection 3.6.1) applies also for the µc-Si:H growth. The hydrogen attaches to the dangling bonds and this brings to an almost depleted surface by free bonds. The reaction is exothermic and the released heat improves the SiH_3 diffusion to a preferred location from an energetic point of view, and for instance, the µc-Si:H film results in an ordered structure. Therefore an organised lattice, such as the one of microcrystalline material, enables nucleation sites for epitaxial-like film growth [40].

3.7. Physical vapour deposition (PVD)

If in Section 3.6 PECVD has been discussed as a chemical method to produce gas source, here a non-chemical technology, also known as physical vapour deposition (PVD), has been analysed since its employment in the experimental part (Chapter 5). Two methods have been used: sputtering and evaporation. The PVD requires to be in a vacuum as in PECVD mechanism, and metals such as Ti, Al, Cu or compounds are involved during the process to fabricate contacts [42].

In the sputtering method (Figure 3.10), atoms are arranged on a target, and a free accelerated atom or ion hits the target by transferring energy and momentum to atoms. These atoms are enabled to escape from the target and evaporate (gas phase). The required power can be supplied by a reactive direct current (DC) or a radio frequency (RF) source [7].

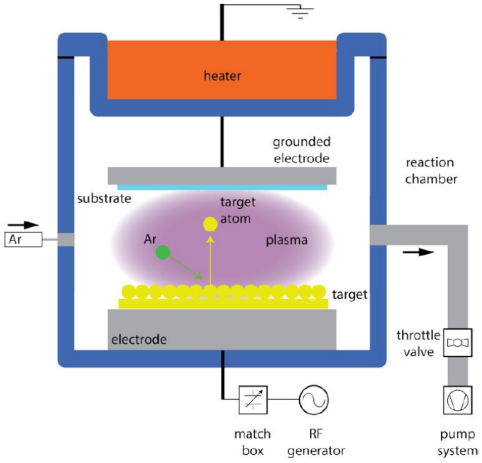

Figure 3.10: PVD with sputtering mechanism [16].

The target atoms form cathode deposit onto the substrate at the anode, meanwhile a steady control of pressure with inert argon gas (Ar) keeps the whole chamber in a vacuum. The interaction between Ar and the electromagnetic field powered by RF generator accelerates positively-charged argon ions (Ar^+) that through bombardment of the target facilitates the layer development on the substrate. Generally, sputtering is applied for transparent conducting oxide TCO, indium tin oxide

ITO or AZO aluminium-doped zinc oxide layers deposition, and besides, for metallic layers as for instance front/back contacts.

In the evaporation method, an additional metallic layer such as Al, Cu or Ag can be deposited [7]. The metallic source material is heated above the melting point and by evaporation, it solidifies on the substrate surface. As in the available equipment in EKL laboratory, the metallic crucibles are installed at the chamber base, making the metallic vapour possible to flow upwards. While the substrates holder is a rotating carrier in order to achieve an enhanced and uniform deposition.

4

Triple junction optical modelling

In this Chapter the focus has largely been placed on optical properties for the development of flexible, lightweight silicon-based triple junction solar cell on Al substrate. Section 4.1 explains the powerful Matlab tool used for the optical modelling: GENPRO4. Section 4.2 shows the triple-junction architecture by providing an explanation of the implemented layers and coatings. In Section 4.3 the texturing has been addressed in a theoretical way by exploring two available types of textures, and then it has been simulated for triple-junction structure. In Section 4.4 the light model has been validated through a preliminary investigation of theoretical aspects, and afterwards implemented into the simulations. Then, Section 4.5 has provided a comprehensive analysis on current matching conditions and the potential spectral utilisation of the solar device under discussion. In Section 4.6 the optical modelling has been focused on the properties of back reflector, whereas Section 4.7 has offered a sensitivity analysis of sub-cells thicknesses variation. The enhancement obtained by the encapsulant embedding has been investigated in Section 4.8. Finally, the front reflector implementation and the TCO properties have been examined in order to deepen fully the triple-junction optimal modelling.

4.1. GENPRO4 tool for optical modelling

Optical modelling is a powerful tool that allows designing the solar devices and simulating the optical response. For a given solar cell architecture, the optical simulation provides the reflectance (R), transmittance (T) and absorptance (A) as a function of wavelength. It also takes into account the light scattering effect at the interfaces, how the light is trapped into the structure and the parasitic absorption losses. The ingoing light is partially absorbed in each layer and the rest is transmitted to the layers below. This is extremely dependent on the absorption coefficient and thicknesses of each material. Therefore, parasitic absorption losses represent the overall amount of light absorbed into inactive layers [7].

The triple junction optical analysis has been carried out by using GENPRO4 software in Matlab. GENPRO4 is an optical model that treats the solar device as a multi-layer structure for its computations. The main simulation outputs deliver information regarding the photo-current density and generation profile by calculating the fraction of incident light absorbed in each layer. However, it is important to emphasise this software simulates only the optical characteristics of the device, while the electrical ones are completely neglected.

This software computation is based on the extended net-radiation method that includes the light scattering effect at the textured interfaces. It also takes into consideration the flexibility feature, indispensable for thin-film devices such as the triple-junction solar cells made on bendable Al-foil. The interfaces surface is simulated in a realistic 3D way via atomic force microscopy (AFM) scanning which is used as surface morphology input.

4.1.1. The extended net-radiation method

As mentioned above, GENPRO4 applies the extended net-radiation method and works efficiently with both textured and flat interfaces surface. The easiest case is when the interfaces are flat, Figure 4.1 offers a schematic representation of the multi-layer structure and light paths.

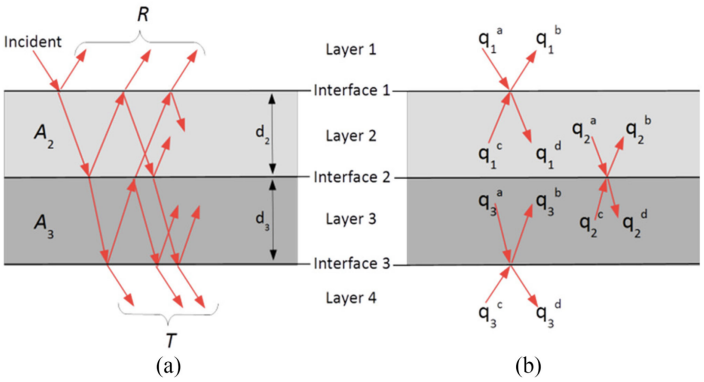

Figure 4.1: Multiple layers layout with a) R, T and A_i optical paths and b) net-radiation fluxes [18].

The simulation aims to achieve the total R, T and A_i (for each layer i) that are wavelength dependent. The main inputs for these optical quantities computation are the layers thickness d_i and complex refractive index $\tilde{n}(\lambda)$ as a function of wavelength. The $\tilde{n}(\lambda)$ has been defined in Section 2.4 (Chapter 2). Refractive index and absorption index have been presented in Figure D.1 and Figure D.1 (Appendix D) for each layer or coating applied in the triple-junction optical modelling. The calculation is repeated for each wavelength, normally the range is between 300 nm and 12000 nm, in which the active layers absorb photons. Flat interfaces calculate the interface reflectances r_i through the Fresnel equation, the interface transmittances t_i as r_i=1-t_i, and the layer transmittances τ_i with the aid of the Lambert–Beer law. As Figure 4.1a underlines, an incoming photon can impact the same interface several times via a complex path, hence all the eventual reflections have to be taken into account for the calculation of R, T and A_i.

Figure 4.1b shows four fluxes q_i^x at each interface for the extended net-radiation method. Here, x can assume a, b, c, d configurations, each letter represents the incoming or the outgoing light for each interface from the top or bottom part. The net-radiation (W/m^2) is expressed by these fluxes that consider all possible photon paths. In order to have dimensionless quantities, it should preferably normalised each flux to the incident radiation in W/m^2. Hence, the fluxes are put in relation through the following system of equations [43]:

$$\begin{cases} q_i^a = \tau_i \cdot q_{i-1}^d \\ q_i^b = r_i \cdot q_i^a + t_i \cdot q_i^c \\ q_i^c = \tau_{i+1} \cdot q_{i+1}^b + 1 \\ q_i^d = t_i \cdot q_i^a + r_i \cdot q_i^c. \end{cases} \tag{4.1}$$

The Equations set 4.1 has to be solved to obtain R, T and A_i, this latter may be seen as the difference between all fluxes into and out of layer i. Considering I as the total amount of interfaces, the optical quantities result to be equal to:

$$\begin{cases} R = q_1^b \\ T = q_I^d \\ A_i = q_{i-1}^d - q_{i-1}^c + q_i^b - q_i^a. \end{cases} \tag{4.2}$$

Since now, the effects of the interface have been completely ignored for the fluxes resolution. This method is consistent only if the layers thickness is bigger than the coherence length of light (in the range of 1 µm), therefore layers are called incoherent [18]. If layers are thin or coherent, the fluxes have to include the complex amplitude of electromagnetic waves [44]. Thus, in GENPRO4 media are treated incoherently if they generate thick layers, otherwise they are considered coherently if thin coatings are built up at interfaces.

In general, solar cells include texturing at the interfaces between layers to scatter more light and enhance the active layers absorption. This implies the incident light propagates in multiple directions, so an angular intensity distribution has to be associated for the reflectance and transmittance derivation. Figure 4.2a considers the region of light incidence as a hemisphere and each light direction can be detected by zenith (between 0° and 90°) and azimuth angles. They are the perpendicular and parallel positions to the interface plane respectively. The net-radiation method divides this space region into cones to which an angular range is related, and each cone is characterized by its corresponding sub-flux.

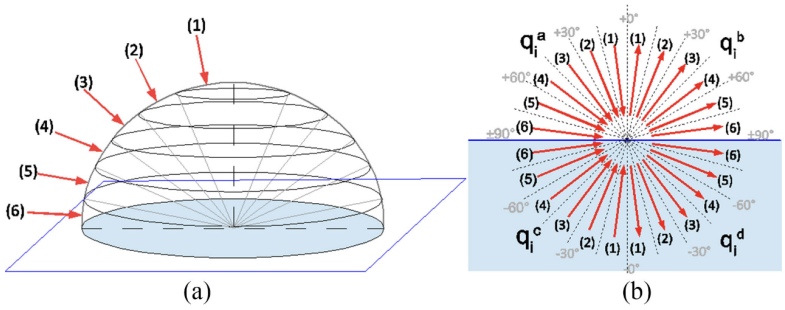

Figure 4.2: Graphic scheme of the net-radiation method at interface 1:
a) partition into a hemisphere and angular intervals, b) sub-fluxes in a radial pattern [18].

In GENPRO4 this approach is extended to a full sphere, where each flux $q_i^x(v)$ is distinguished by the layer i and angular interval v of belonging. Even if Figure 4.2b is a simplified representation that shows only six ranges for each zenith angle, the software calculation is refined by considering up to thirty intervals for each complementary angle. As the Equations set 4.1 for the case of flat interface, similar flux formulas can be found for the case of textured interface. If V is the total amount of angular ranges, then the equations set results to be matrices of VxV size, also known as $\boldsymbol{r}_i$ and $\boldsymbol{t}_i$ scattering matrices, and $\boldsymbol{\tau}_i$ layer transmittance matrix . Reflectance, transmittance and absorptance are calculated as follows:

$$\begin{cases} R = \sum \boldsymbol{q}_1^b \\ T = \sum \boldsymbol{q}_I^d \\ A_i = \sum \boldsymbol{q}_{i-1}^d - \sum \boldsymbol{q}_{i-1}^c + \sum \boldsymbol{q}_i^b - \sum \boldsymbol{q}_i^a, \end{cases} \tag{4.3}$$

for example, $\sum \boldsymbol{q}_1^b = q_1^b(1) + q_1^b(2) + \cdots + q_1^b(V)$ is the total R at interface 1 and is given by the sum of all sub-fluxes of this vector [18].

4.2. Triple junction implementation

As discussed in Section 3.4 (Chapter 3), multiple p-n junctions with different bandgaps increment the solar spectrum utilisation of the device. Figure 4.3 represents the triple junction solar cell architecture, in which the top sub-cell is a-Si based, while the middle and the bottom sub-cells are nc-Si based. The intrinsic a-Si:H absorber layer has a bandgap of 1.75 eV, and the absorption occurs at short wavelengths of the light spectrum, mainly in the blue region (below 700 nm) [45]. While the intrinsic nc-Si:H absorber layer has a bandgap of 1.12 eV, meaning most of the absorption takes place at long wavelength up to the near infrared region (below 1100 nm) [46].

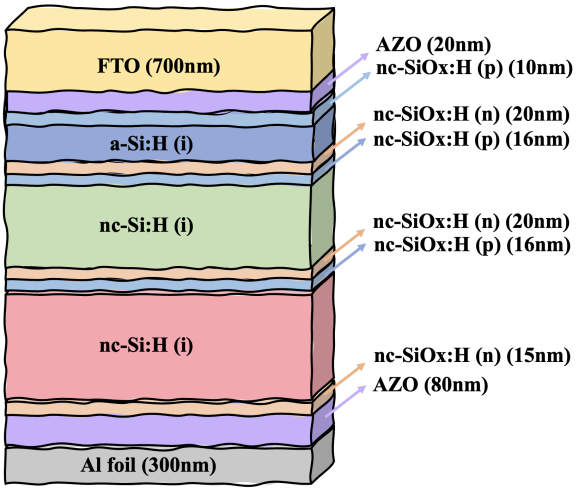

Figure 4.3: a-Si/nc-Si/nc-Si triple-junction architecture.

Looking at the multi-junction structure, the light incomes from the top side of the device. The a-Si material absorbs the blue spectral part, where photons have high energy, but low penetration depth. This explains why the solar cell with the highest bandgap has to be placed as the top one. The red light, on the contrary, has high penetration depth and low bandgap. Therefore it is able to travel through the device and then is absorbed in the middle or bottom sub-cells, both arranged below the top one.

For a better understanding of the working principle, an equivalent electrical circuit has been provided in Figure 4.4. Here, the three junctions are connected in series, and each sub-cell follows the circuital configuration discussed already in Section 2.7 (Chapter 2). According to Kirchhoff's law, at the external terminal, the resulting voltage is the sum of the three voltages, while the current density is the same throughout the circuit. The sub-cell with the lowest current density characterises the overall circuital current density. The p-n junction with the smallest current value is defined as the current limiting device.

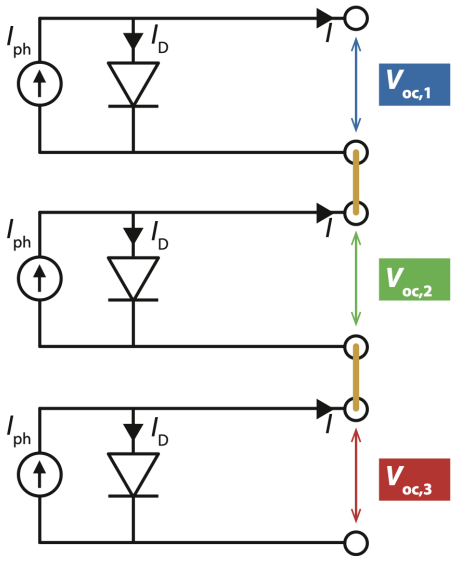

Figure 4.4: Electrical equivalent circuit of a triple-junction solar cell [7].

Figure 4.5 provides a simplified depiction of the triple-junction band diagram. On the left, the top a-Si:H *p-i-n* junction band diagram is represented with the highest bandgap, the band diagrams of the middle and bottom nc-Si:H sub-cells are depicted to the right side of a-Si:H sub-cell with a lower bandgap. So, when these three sub-cells are linked in series, the *p*-layer of the top cell creates a *n-p* junction with the *n*-layer of the middle cell. By analogy, a *n-p* junction is also formed between the middle and the bottom cells.

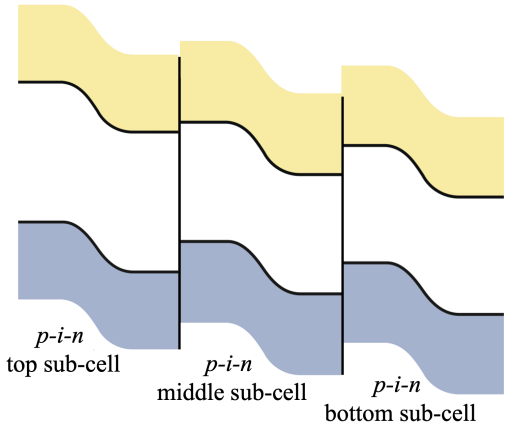

Figure 4.5: The solar device band diagram without tunnel junctions. Inspired by [7].

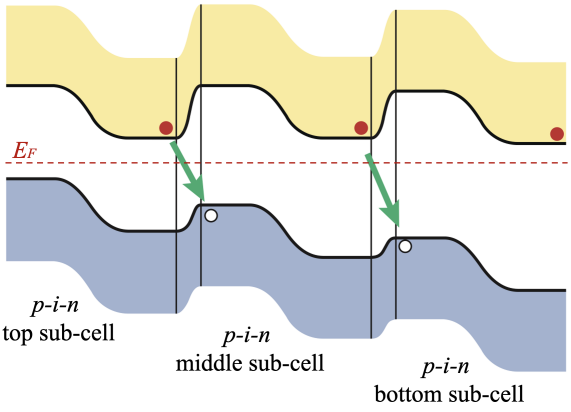

Figure 4.6: The solar device band diagram with tunnel junctions. Inspired by [7].

These reverse junctions provide a voltage drop because they work in reversed direction compared to *p-i-n* junctions. In order to prevent that, tunnel junctions provide continuity to the conduction band and the valence band. Accordingly, each tunnel junction has a steep inclination and small width, hence electrons from *n*-side can go easily through the tunnel junction and recombine with holes at the *p*-side (Figure 4.6). At these junctions, the bandgap is considerable high to prevent any losses by potential parasitic adsorptions, and furthermore *n-p* junctions need to have a small electrical impedance. As a result, the lower is the resistance to the passage of carriers, the smaller will be the voltage drop at the tunnel junctions. In the end, holes in the *p*-layer of the top sub-cell are

collected at the front contact, whereas electrons in the n-layer of the bottom sub-cell are collected at the back contact of the triple-junction. By way of final comment, Figure 4.6 has the mere purpose of representing the tunnel recombination junction process, but the bandgaps are not realistic and do not coincide with those explained in Figure 4.5.

4.2.1. Layering & Coating

Figure 4.3 displays the triple-junction structure implemented in GENPRO4 for the optical simulations. The sketched solar device is in superstrate configuration: the first layer subjected to the incident light is also the first deposited in the fabrication process. Starting at the top, the first medium is the FTO and is defined as a layer with a thickness of 700 nm. The FTO acts as a transparent front electrode, it traps the light into the solar device and enables the underlying active absorber layers to absorb photons due to its transparency and conductivity, or in other words high optical transmittance and low electrical resistivity [47]. Further details regarding the transparent conductive oxide properties can be found in Section 3.1 (Chapter 3).

Below it, the FTO/a-Si interface is formed by two coatings. The AZO is 20 nm thin and functions as a buffer layer. Working with bi-materials transparent conductive oxide allows optimising the electrical features and the optical properties in a wider range of the solar spectrum [48]. The other coating medium is p-doped side of the top sub-cell and is made of 10nm of nc-SiOx:H material. Its main function is the collection of holes. In thin-film p-n junctions, holes are less mobile than electrons, thus this layering order allows a higher generation rate at p-doped layer than at n-doped layer and so p-type layer may be reached more easily by holes [7].

The intrinsic media have been defined as layers and not as coatings due to their thicknesses and photo-active absorber function. For the intrinsic layer, the top cell features a-Si:H material, while the middle and bottom cells have nc-Si:H material. The thicknesses of absorber layers have not been indicated in Figure 4.3 as they change depending on the optical simulations. Further explanations about the characterization and properties of amorphous and microcrystalline materials have been addressed in Chapter 3.

The top/middle and middle/bottom sub-cells interfaces present the same coating structure: 20 nm of n-doped nc-SiOx:H and 16 nm of p-doped nc-SiOx:H. The nanocrystalline silicon oxide is a suitable material for the tunnel junctions. The p-doped nc-SiOx increases its band bending features when is highly doped and facilitates the tunnel recombination [49]. The chosen thicknesses for the nc-SiOx media are the result of a tunnel recombination junction analysis, based on a previous work by G.Padmakumar [50]. The n-SiOx:H thickness is typically decided with the object of destructive interference of light at i-n location. An optimised thickness reduces the electric field and as consequence, the parasitic absorption in the n-doped layer. While p-SiOx:H with a high bandgap decreases parasitic absorption in the blue part of the light spectrum [7].

The lowest interface between nc-Si:H (i) of bottom sub-cell and air has been developed with 15 nm of n-doped nc-SiOx:H and the back contact made by 80 nm of AZO and 300 nm of Al foil. Here, the metallic back contact performs as electrons collector, Al has been chosen due to its conductive properties and market availability at a low price. Silver could be a good aluminium replacement for the back contact: this material has higher reflectivity than aluminium, but it is also more expensive than Al.

4.3. Texturing

Textured interfaces have been used for the enhancement of the light management. Having rough interfaces helps to reduce the reflection because the reflected back light has the chance to rebound at the surface. Hence, more light is transmitted into the cell. As result, the total reflection is decreased and the light in-coupling is boosted in the solar cell [51]. Figure 4.7 illustrates how the incident light is reflected multiple times enabling an improvement of the refracted amount of light in the medium

below the interface.

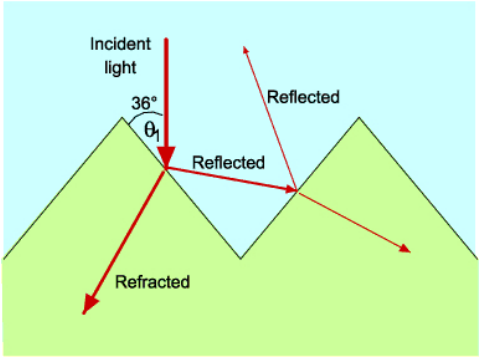

Figure 4.7: Representation of light path for textured interfaces [19].

4.3.1. Factory Baseline texturing

The R2R technology includes the so-called Factory Baseline that is used to allocate texturing at the Al foil surface. The texturing is achieved through a wet chemical etching process by using highly-diluted NaOH:H_20. The Factory Baseline main features are:

$$\begin{cases} \sigma_{RMS} = 28.4 \text{ nm}, \\ L_c = 497 \text{ nm} \\ \sigma_{RMS}/L_c = 5.7\%, \end{cases} \tag{4.4}$$

where σ_{RMS} is the root mean square roughness that characterises the surface unevenness through several height measurements [52]. L_c is the autocorrelation length that measures the craters width of the textured surface. σ_{RMS}/L_c represents the ratio between the root mean square roughness and the autocorrelation length.

A higher aspect ratio would mean low quality in the nc-Si:H growth, but it would result in an enhancement of the light trapping. Besides, light is trapped through the transparent conductive oxide that has a specific nano-textured surface and is deposited on top of the textured Al foil. Hence, it is extremely important to have an Al surface with smooth and wide craters in order to superimpose the FTO texturing on this one. This approach is also known as modulated surface texturing (MST).

Therefore the following deposited layers have to be conformal with the texturing of Al foil. This helps to minimise the reflectance and distribute the scattered light with a larger radial range, also known as angular intensity diffraction (AID). Figure 4.8 provides a 3D plot of the Factory Baseline texturing, this can be characterised by scanning the surface through AFM. The height-map refers to Interface 1 between air layer and FTO layer in GENPRO4 simulation.

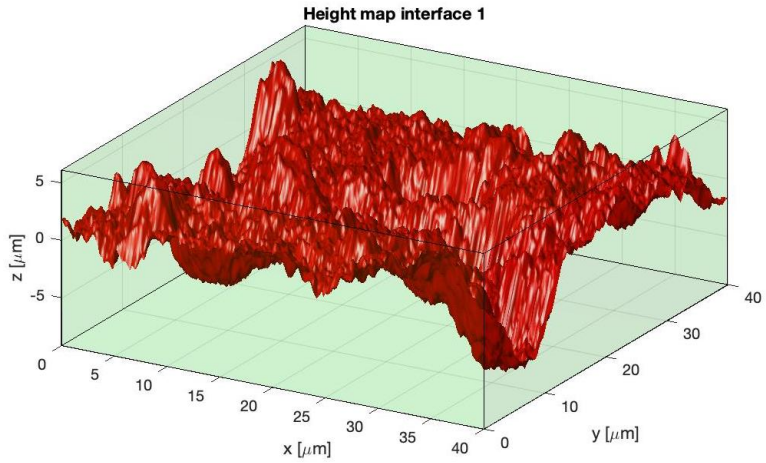

Figure 4.8: 3D representation of Factory Baseline texturing simulated in GENPRO4.

According to the results provided by HyET [20], this texturing features has surface morphology with small craters that obstruct the nc-Si layers deposition. The material results to be defected with cracks and vacancies in the bulk. Based on this analysis, a new texturing with larger craters has been developed and is called FLAM01.

4.3.2. MST: FLAM01 texturing

The developed FLAM01 morphology has been designed to meet two functions: enhancing the light trapping and favouring the microcrystalline material growth. As the height map shows in Figure 4.9, the surface is characterised by micro-textures with a smooth U-shape. On one hand, sharp nano textures would increase the light trapping in a-Si:H layer and decrease the thickness. Having a thicker a-Si:H layer would also mean higher light-induced degradation [7]. On the other hand, smooth texturing is needed for efficient light trapping in the red and near infrared region of the solar spectrum. Additionally, the high deposition rate of nanocrystalline silicon layers adapts better to this morphology and achieves defects free deposition [20]. The FLAM01 modulated surface texturing also provides an increase of short circuit current densities without affecting the FF and the V_{oc} [53].

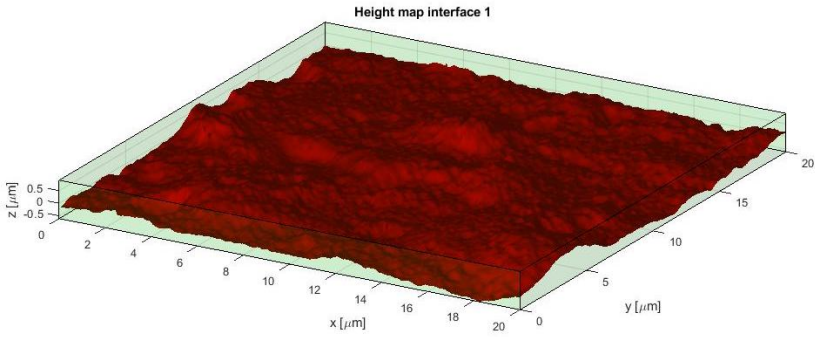

Figure 4.9: 3D representation of FLAM01 texturing simulated in GENPRO4.

The FLAM01 texturing is superimposed on aluminium rolls trough the etching of these substrates in a solution of sodium hydroxide (NaOH) diluted in water. As shown in the work carried out at HyET [20], the etching rate of NaOH is higher than the one used in the Factory Baseline. The FLAM01 main features are:

$$\begin{cases} \sigma_{RMS} = 233 \text{ nm}, \\ L_c = 2270 \text{ nm} \\ \sigma_{RMS}/L_c = 10.2\%, \end{cases} \tag{4.5}$$

4.3.3. FLAM01 and Factory Baseline texturing comparison

The GENPRO4 simulations have compared Baseline Factory and FLAM01 texturing through their optical effects on the triple-junction solar device. Figure 4.10 establishes a connection among three developed types of textures: Factory Baseline, FLAM01 and Lab-scale. The normalised angular intensity diffraction (AID) has been measured as a function of the spectrophotometer angle at 800 nm for each texturing. The goal was to investigate the differences in the near infra-red region of the light spectrum.

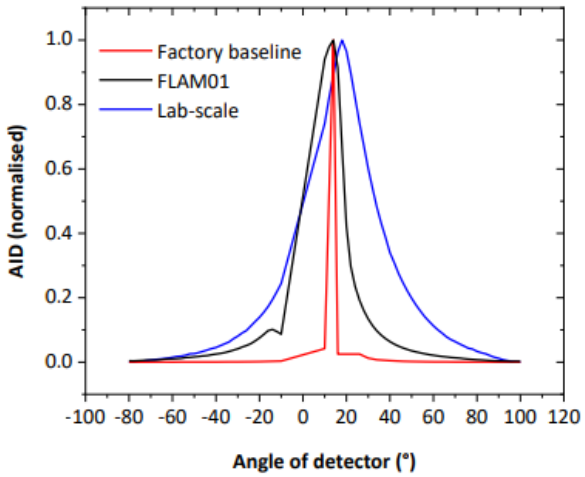

Figure 4.10: AID for Factory Baseline, FLAM01 and Lab-scale texturing compared at 800 nm [20].

The scattering properties of Factory Baseline (red curve) are smaller than the other two texturing. The AID of FLAM01 (black curve) is between -20° and 20° and the AID of the texturing on lab-scale (blue curve) is between -40° and 40° [20].

The triple junction device has been simulated through two different texturing scenarios: FLAM01 and Factory Baseline, and particular attention has been paid to the absorbance of three intrinsic layers of the structure. In Figure 4.11 and Figure 4.12 the FLAM01 has been taken as the texturing of reference, therefore the thicknesses of the photo-active absorber layers assume values that satisfy the current matching (c.m.) condition. Further explanations about the current matching topic have been provided in Section 4.5. In the first analysed scenario, each interface has the FLAM01 texturing and fixed top sub-cell thickness at 80 nm, then a study on thicknesses optimisation has led to 1.1 µm for the middle sub-cell and 2.5 µm for the bottom sub-cell.

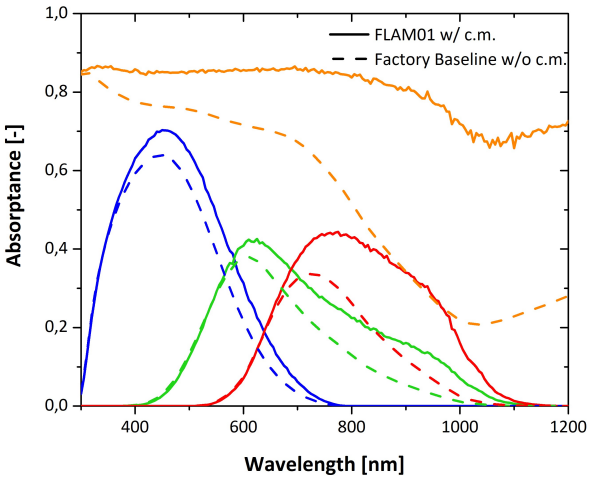

Figure 4.11: Total and active layers A for FLAM01 in c.m. and Baseline not in c.m. condition.

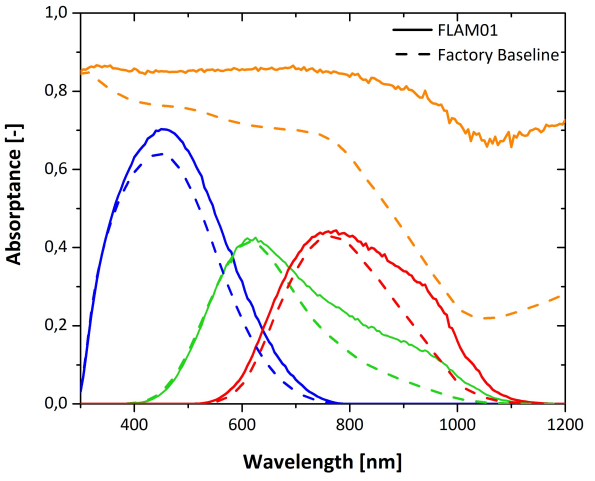

Figure 4.12: Total and active layers A for FLAM01 and Baseline both in c.m. condition.

Figure 4.11 shows multiple absorptance curves as a function of the wavelength in the range where the spectral utilisation occurs for the triple junction, which is between 300 nm and 1200 nm. Here, the intrinsic layers absorptance is represented in blue for the top-cell, in green for the middle-cell and in red for the bottom-cell, whereas the total triple junction absorptance is depicted in orange.

The total absorptance includes the amount of light absorbed in active layers and the one lost in the inactive layers and coatings of the solar cell. In Matlab environment, the total absorptance has been calculated as the unit minus the absorptance in the air layer or, in other words, the light reflected back into air at the front side. If A+R=1, then the total absorptance results 1-R. In GENPRO4 simulations, it has been verified that an Al foil of 300 nm does not allow any transmittance at the back side, hence T is assumed to be zero.

In the graph, the full lines represent the total and active layers absorptance when FLAM01 texturing is applied at the interfaces, while the dashed lines correspond to the total and active layers absorptance with Factory Baseline texturing. On one hand, using FLAM01 texturing implies higher light absorption in the three sub-cells and an increase in the photo-generation rate. On the other hand, the other inactive substrates absorb more, resulting in a visible increase of the total absorptance with FLAM01 compared to Factory Baseline. Baseline texturing presents an absorption drop that becomes more and more relevant from the top sub-cell to the bottom sub-cell. This behaviour denotes the incompatibility of Factory Baseline craters dimensions with the light absorption at long wavelength (above 800 nm). Therefore, these results are consistent with the analysis of texturing in Section 4.8.

As an additional remark, the Factory Baseline scenario has the same thicknesses as in the other texturing scenario. However, this implies that current mismatched active layers reduce the absorption and the photo-generation. Table 4.1 displays the photo-current densities, where a-Si:H(i)-nc-Si:H(i)-nc-Si:H(i) are 80 nm - 1.1 µm - 2.5 µm thick for both scenarios.

Sub-cell	*Thickness*	J_{ph} *w/ FLAM01*	J_{ph} *w/ Factory Baseline*
top	80 nm	8.74 mA/cm^2	7.24 mA/cm^2
middle	1.1 µm	8.77 mA/cm^2	6.51 mA/cm^2
bottom	2.5 µm	8.72 mA/cm^2	5.39 mA/cm^2

Table 4.1: J_{ph} of intrinsic layers with fixed thicknesses for FLAM01 and Factory Baseline texturing.

Even though the selected thicknesses only allow an equal distribution of current densities in the first scenario, the photo-current density of bottom sub-cell is the current limiting junction for both scenarios.

Figure 4.12 compares the absorptance in top, middle and bottom sub-cells and the total absorptance when currents are matched in the intrinsic layers with FLAM01 and Factory Baseline texturing. In this thesis, the absorptance has been always considered as the ratio between the absorbed light and the solar incident radiant power in a specific layer. Therefore, the maximum represents the highest value of light absorbed by a material at a specific wavelength. The top sub-cell absorptance peak is found at 0.7 for FLAM01 texturing and at 0.6 for Factory Baseline texturing. Instead, the absorptance peaks of the middle and bottom sub-cells reach 0.4 and 0.45 respectively for both texturing. Reaching the current matching condition helps to boost the absorptance and photo-current density in each active layer, but this is still less effective in the near infra-red region (from 800 nm onward). However, the amount of light absorbed by including FLAM01 texturing is significantly higher than the case with the Factory Baseline.

In order to reach the current matching requirement with Factory Baseline texturing, the top-sub cell thickness has been held to the value of 80 nm, this has resulted in thicker layers for the middle nc-Si:H(i) and bottom nc-Si:H(i) and lower photo-current densities.

Factory Baseline texturing					
Sub-cell	*Thickness*	J_{ph} *w/o c.m.*	*Sub-cell*	*Thickness*	J_{ph} *w/ c.m.*
top	80 nm	7.24 mA/cm^2	top	80 nm	7.23 mA/cm^2
middle	1.1 µm	6.51 mA/cm^2	middle	1.4 µm	7.01 mA/cm^2
bottom	2.5 µm	5.39 mA/cm^2	bottom	5.8 µm	7.05 mA/cm^2

Table 4.2: J_{ph} and thicknesses of intrinsic layers when the c.m. condition is or is not reached with Factory Baseline texturing.

Table 4.2 shows the thicknesses and currents of photo-active absorber materials when the current matching are or are not respected. The top sub-cell is the only layer that has not changed thickness value for both cases. $J_{ph,\,top}$ and A_{top} do not exhibit any inconsistencies if the triple-junction optical properties are simulated with or without the c.m. condition. While the middle and the bottom sub-cells show significant improvements with regard to $J_{ph,\,middle}$, $J_{ph,\,bottom}$, A_{middle} and A_{bottom}, especially in the near infra-red wavelength range. The optical achievements can also be seen through the total device absorptance: less reflected light at the front side means more red light transmitted into the solar cell and therefore, more light absorbed by the bottom sub-cell. Moreover, Figure 4.13 illustrates the absorptance enhancement among intrinsic layers by balancing the current densities.

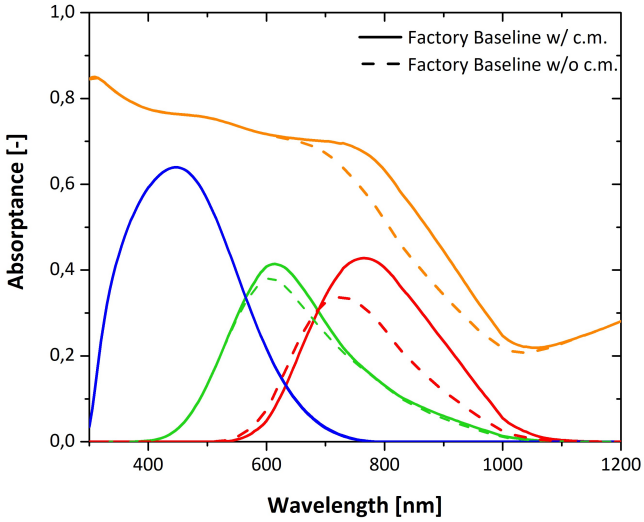

Figure 4.13: Total and active layers A when a-Si:H/nc-Si:H/nc-Si:H layers are current matched or not with Factory Baseline texturing.

4.4. Light model validation

The simulations in GENPRO4 can apply wave or ray optics. If the optical model is set to "wave", then the light includes purely the electromagnetic wave behaviours. In Matlab environment, light treated as wave means that each optical simulation has to solve the Maxwell equations. However, this approach carries a considerable computational complexity. The optical properties of thin-film solar cells are usually modelled through a Maxwell solver when it takes an admissible interval of time [54]. For this reason, the wave model is applied in a restricted simulation domain.

The light can be also approximated through a ray model and, the interaction between textured interfaces and light is simulated thanks to ray-tracing techniques [55], [56]. The diffraction is the main optical effect when light, considered as a wave, encounters a particle. In the ray model, the diffraction is completely ignored. Hence, the scattering effect that characterises the ray nature of light, does not apply for features smaller than the wavelength unit. If surfaces have sub-wavelength texture, then an optical model known as scalar scattering is required [21], while a texturing with surface features larger than light wavelength uses the ray tracing method [57]. Finally, any optical model needs AID as input, because it provides the morphology of the interfaces. As mentioned in Section 4.3.1, this preliminary surface scanning is done via AFM.

4.4.1. Wave & Ray light models

It has been discussed in Section 2.4 (Chapter 1) that if a monochromatic light beam with λ as wavelength interacts with a flat interface, then Fresnel equations provide the transmitted and reflected components of the incident light. In general, the interface size is smaller than λ. Although, the modelled triple-junction solar cell has nano-textured interfaces and a schematic light behaviour at one textured surface is given by Figure 4.14. A part of the incoming light may be specularly transmitted or reflected, these two specular components are abbreviated as T_{spec} and R_{spec} respectively; while another portion of light deviates from the specular direction of the angle of light incidence and generates the scattered/diffused transmission and reflection (T_{dif} and R_{dif}).

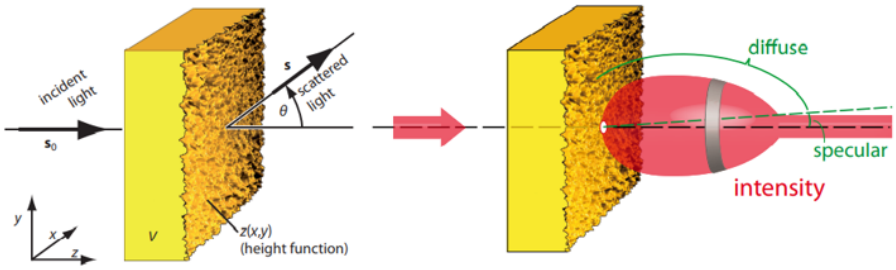

Figure 4.14: Light scattering scheme at a nano-textured interface [21].

Consequently, having rough or flat interface makes a difference in the definition of total T and R, and hence if the feature size of textured interfaces has the same order of magnitude of λ, then these equations can be found as follow [21]:

$$T_{\text{tot}}(\lambda) = T_{\text{spec}}(\lambda) + T_{\text{dif}}(\lambda), \tag{4.6}$$

$$R_{\text{tot}}(\lambda) = R_{\text{spec}}(\lambda) + R_{\text{dif}}(\lambda). \tag{4.7}$$

If the surface feature size is larger than λ, the specular portion of light is null, meaning a complete deflection of light occurs at the interface. Since now scattered light and diffused light have been used in the same sense. However, the diffuse reflection may characterise both flat or rough interfaces, while the scattering mechanism is exclusively responsible for R_{dif} with textured surface [23].

Moreover, it is possible to define the haze in transmission H_{T} and the haze in reflection H_{R} as the part of scattered transmission or reflection overall T_{total} or R_{total} and explicit them through:

$$H_R(\lambda) = \frac{R_{\text{dif}}(\lambda)}{R_{\text{tot}}(\lambda)}, \qquad H_T(\lambda) = \frac{T_{\text{dif}}(\lambda)}{T_{\text{tot}}(\lambda)}. \tag{4.8}$$

The scalar scattering theory is based on the differentiation of scattering effect into its main components: specular part and diffuse part. The specular fraction does not have any dependency on the texture at the interface. Even if the surface is flat or rough, its propagation complies with wave optics and is responsible for interference effects. The diffuse component may be modelled through ray optics by considering the light intensity and AID, and neglecting the wave features such as amplitude or phase.

When the textured surface features are smaller than the wavelength, the scalar scattering theory is employed in GENPRO4 optical modelling in order to take into account interference and diffraction effects. The interference is treated as a collection of point sources that propagate spherical scalar waves. Therefore, the phase is calculated through the specific height of the point placed on the surface and the angle of incidence. Each direction of propagation has a scattering intensity and this is the result of constructive or destructive interference in that specific location. This method has been validated for several surface configurations, the experimental results suggest the use of wave model when the feature size is lower than 100 nm [18].

Conversely, the ray model can be used when the feature sizes are in the same order or larger than the light wavelength, hence the wave nature of light can be neglected by exclusively looking at ray optics.

4.4.2. Optical results depending on texturing

In order to validate the ray model or alternatively the wave model, several scenarios have been investigated for both FLAM01 and Factory Baseline texturing. Figure 4.15 represents the three picked scenarios for each texturing typology.

On the left, I scenario models light with ray features for all interfaces of the triple-junction device and uses FLAM01 texturing. While II scenario substitutes the ray tracing model with the wave model at the IV and V interfaces. If the Matlab triple-junction architecture in Appendix A is taken into account, the V interface is defined by two coatings: nc-SiOx(n) of the middle sub-cell and nc-SiOx(p) of the bottom sub-cell. The V interface is characterised by the n-doped nc-SiOx coating of the bottom sub-cell and the back contact (AZO and Al substrate). Instead, the third scenario only applies the wave model at all interfaces.

On the right, three similar scenarios have been implemented for the light model validation when the Factory Baseline texturing is used. Here, I case models light as wave at each interface, II scenario applies the ray model at IV and V interfaces, III configuration treats light only through ray optics.

Light models with FLAM01 texturing			
	ray	IV and V wave	wave
I scenario	✓	✗	✗
II scenario	✓	✓	✗
III scenario	✗	✗	✓

Light models with Factory Baseline texturing			
	ray	IV and V ray	wave
I scenario	✗	✗	✓
II scenario	✗	✓	✓
III scenario	✓	✗	✗

Figure 4.15: Light model validation through three case studies for FLAM01 and Factory Baseline texturing.

It is important to notice that the connection between colours and top-middle-bottom sub-cells absorptance has not been altered in the next graphs of this Chapter and the association of optical quantities with colours can be found in Section 4.3.3. The following results have been provided in current matching condition, the thicknesses of the active layers are from Table 4.1. The results provided with mismatched currents or different current matching conditions have always been made explicit.

Figure 4.16 relates the three investigated scenarios through the total and active layers absorbance. The FLAM01 textured surfaces show some differences in term of light absorption between the ray tracing model and the scalar scattering theory. I scenario (full line) illustrates optical behaviours with the ray tracing model. As explained in Section 4.4.1, nano-textured surfaces such as the ones characterised by FLAM01 texturing have size features much bigger than the light wavelength. The light incident on each of the five interfaces interacts with particles that larger than λ. Compared to II and III scenarios, simulations with the ray tracing offer a better optical response. The use of MST enhances the scattering mechanism across the triple-junction active layers. The textured surface helps the scattering effect at short-wavelengths (blue range) in top sub-cell and transmits the red light to the middle and bottom sub-cell. Whereas wavelength above 600 nm scatters at the interface where the middle and the bottom sub-cells are located.

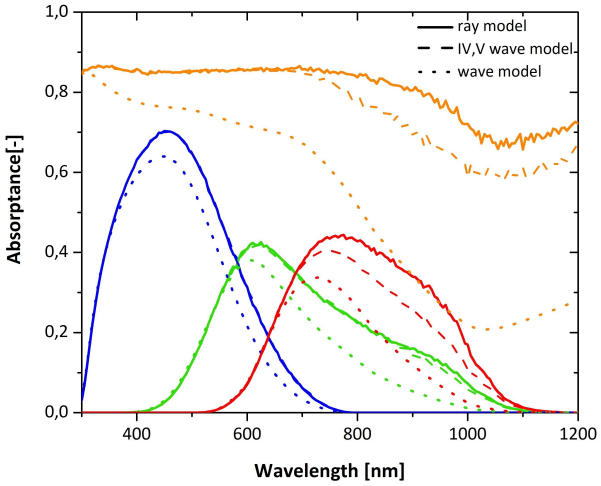

Figure 4.16: Total and active layers A comparison among three scenarios with ray and wave models and FLAM01 texturing.

This does not apply anymore when light is treated as wave at IV and V interfaces (II scenario) or at each interface (III scenario). In the second analysed case, the light scattering does not occur at the upper and lower interfaces of the bottom sub-cell, hence this results in a decrease of light absorption in nc-Si:H layer. Light is still scattered at short and medium wavelength, whereas wavelengths are not scattered above 800 nm. This is reflected by an absorptance drop at long wavelength. If the scalar scattering method is implemented at each interface, the light absorption is decreased in the all range of the solar spectrum. This loss is gradual among the sub-cells, at very short-wavelength it is possible to obtain the same performance because textured size features are still relatable to the wave model. However, the absorption loss becomes greater with the increase of dimensions difference between textured features and wavelength.

$FLAM01 texturing$			
$Light\ model$	$J_{ph,top}$ (mA/cm^2)	$J_{ph,middle}$ (mA/cm^2)	$J_{ph,bottom}$ (mA/cm^2)
I scenario	8.74	8.77	8.72
II scenario	8.77	8.61	7.62
III scenario	7.24	6.51	5.40

Table 4.3: J_{ph} of active absorber layers among three different scenarios simulated with FLAM01 texturing.

Table 4.3 provides the photo-current densities of i-layers in the three sub-cells for each scenario. The absorbance investigation represented in Figure 4.16 matches the photo-current densities among scenarios. In II scenario the near infra-red part of the light spectrum is not absorbed by the bottom sub-cell. The $J_{ph,bottom}$ value decreases more than 1 mA/cm^2 compared to $J_{ph,bottom}$ in I scenario. III scenario underlines the decrease of J_{ph} values among all active absorber layers: treating light through a model incompatible with texturing results in more optical losses, and thus, less photo-generated current density. Additionally, among the three simulated cases, the bottom sub-cell is always limiting the current in the multi-junction device.

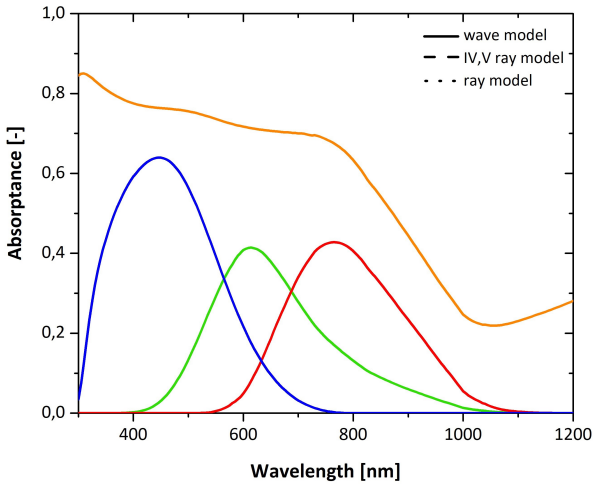

Figure 4.17: Total and active layers A comparison among three scenarios with ray and wave models and Factory Baseline texturing.

Figure 4.17 has been simulated with the current matching condition showed in Table 4.2 and Factory Baseline texturing at each interface. The size features of Factory Baseline texturing have already been presented in Subsection 4.3.1 and result to be compatible with the scalar scattering model. The light incident at one interface encounters features smaller than the wavelength. In this case, light is mainly distinguished by the diffraction effect, and it perpetuates in I, II and III scenarios. The light simulated through a ray tracing model does not allow a comparison between textured features and light wavelength, and therefore the scattering effect related to this model cannot be simulated in GENPRO4. Even if a mixed wave&ray model or a full ray model have been applied, Figure 4.17 presents a complete overlap of active layers and total absorptance among the three simulations. Hence, J_{ph} values do not see any change among the studied cases, as shown in the right part of Table 4.2.

4.5. Current matching & Spectral utilisation

In order to reach the maximum triple-junction device current and optimise the spectral utilisation, the photo-current density needs to have the same value among sub-cells. If the code of the multi-junction architecture in Appendix A is simulated with three random thicknesses for the intrinsic layers, then the respective current density outcomes will be mismatched. Hence, the current matching condition requires specific combinations of thicknesses.

It is possible to meet the current matching condition at higher J_{ph} values and lower thicknesses for the absorber layers by including the light management rules. Some of them, regarding the fundamental concepts of anti-reflective coating (ARC) and refractive index grading, have been discussed in Subsection 4.8.1 below. In Section 4.3 the focus has been paid on textured interfaces and it has been validated the use of FLAM01 texturing. The light in-coupling is enhanced by the elongation of the light pathlength on an optimised textured surface, resulting in more light absorbed in the intrinsic layers.

4.5.1. Algorithm development

The algorithm in MATLAB has been implemented through the GENPRO4 tool and the Matlab triple-junction current matching code has been provided in Appendix B. To reach the current matching condition and understand the spectral utilization, the search algorithm has been based on the sub-cells thicknesses variation. It does not go through all possible thickness combinations, but finds directly the thicknesses that meet the mathematical requirement imposed for the current matching condition. GENPRO4 multi-junction architecture has been simulated only once because the scattering matrices calculated through the architecture code can be reused even if the i-layers assume different thicknesses. Furthermore, the simulations calculate J_{ph} values by integrating the photon flux over AM1.5 spectrum [44].

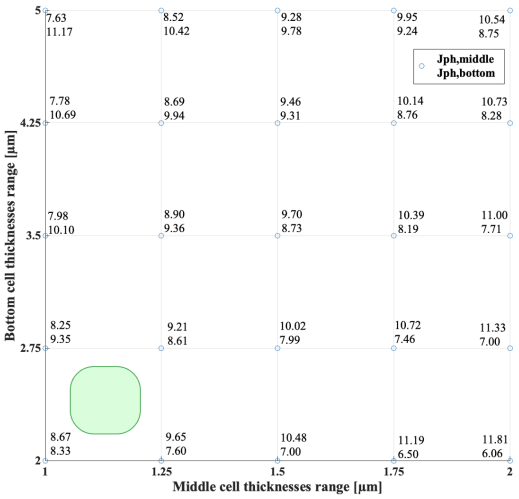

Figure 4.18: Space table of photo-current densities as a function of middle and bottom sub-cell thicknesses.

Afterwords, the simulation has been run for different middle and bottom i-layer thicknesses, meanwhile the top sub-cell thickness has been fixed constant. The algorithm receives as input two thicknesses range, one for the middle and one for the bottom sub-cell. Thus, the user has to indicate which is the starting and ending thickness of each interval and specify the increment in nm. The code translates them into vectors and simulates the optical properties for each top-middle-bottom thicknesses combination. The plot in Figure 4.18 is provided as output: in the space table, each point shows the current density of middle and bottom sub-cell and their thicknesses indicated on x-axis and y-axis respectively.

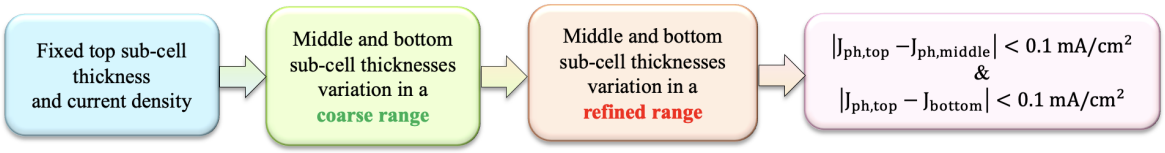

Figure 4.19: Blocks diagram: main steps of the current matching algorithm.

As the simplified blocks diagram of Figure 4.19 suggests, initially one proceeds using coarse thickness intervals and subsequently, once the region where the current matching can be identified, the simulation is repeated using a more refined range. In the example of Figure 4.18, the current matching region is underlined in green, and therefore this is an indicator of where the thicknesses intervals need to be refined.

In the end, the Matlab command window generates a message if the current matching condition

could have been found among the thicknesses by scanning each triplet of J_{ph}. The implemented current matching conditions are met when the absolute values of the difference between $J_{ph,top}$ and $J_{ph,middle}$ and the difference between $J_{ph,top}$ and $J_{ph,bottom}$ are lower than 0.1 mA/cm^2. Both conditions have to be satisfied simultaneously. These two requirements are sufficient to find the thicknesses combination that meets three equal J_{ph}, because the absolute values of the difference between $J_{ph,bottom}$ and $J_{ph,middle}$ complies with the transitive property among three elements. It is implicitly included in the other two mathematical relations.

4.5.2. Graphical implementation

In order to provide a complete current matching analysis, the example shown in Figure 4.18 has also been explained through contour colours representation. Initially, the top sub-cell thickness has been fixed at 80 nm, this corresponds to an absorbed photo-current density of 8.74 mA/cm^2 in a-Si:H layer. However, $J_{ph,top}$ has shown some small value variations among the simulated thicknesses combinations, but they have been neglected due to an order of magnitude of 10^{-3} mA/cm^2. Then the middle and bottom sub-cells thicknesses have been swept in two coarse ranges: 1 µm:0.25 µm:2 µm and 2 µm:0.75 µm:5 µm respectively.

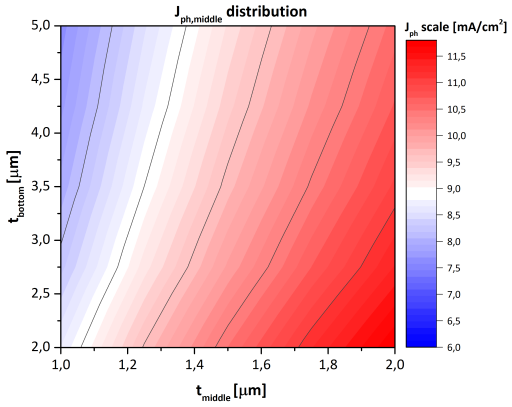

Figure 4.20: $J_{ph,mid}$ distribution in coarse thickness range.

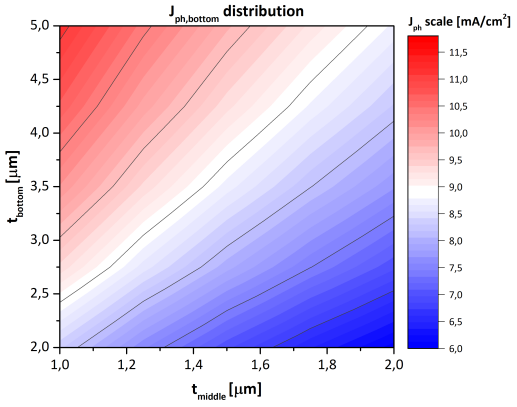

Figure 4.21: $J_{ph,bot}$ distribution in coarse thickness range.

Figure 4.20 and Figure 4.21 depict the J_{ph} distribution of the middle and bottom sub-cells by using contour colours plots. To make consistent colours maps, the same scale in terms of value and colours has been used for both graphs. It goes from 6 mA/cm^2 to 11.5 mA/cm^2 with a colours scale that blends between blue and red.

In Figure 4.20 smaller middle thicknesses t_{middle} and larger bottom thicknesses t_{bottom} underline lower current density values for the middle sub-cell, while combinations with larger t_{middle} and smaller t_{bottom} increase $J_{ph,middle}$. Figure 4.21 illustrates the opposite behaviour: smaller t_{middle} and larger t_{bottom} provide higher $J_{ph,bottom}$ (red region), larger t_{middle} and smaller t_{bottom} find lower $J_{ph,bottom}$ (blue region).

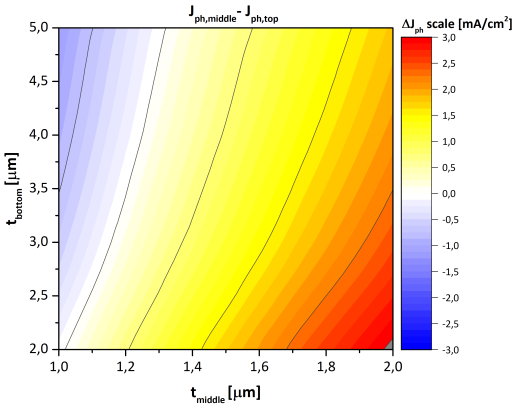

Figure 4.22: $J_{ph,mid}$ - $J_{ph,top}$ in coarse thickness range.

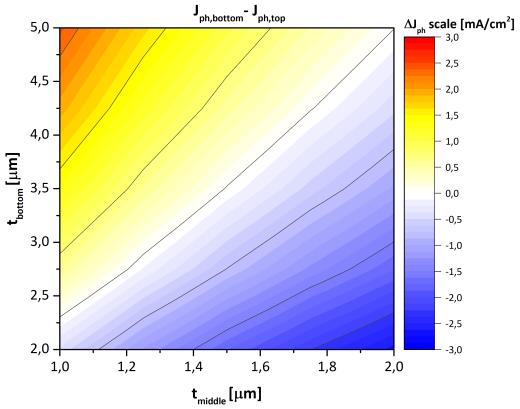

Figure 4.23: $J_{ph,bot}$ - $J_{ph,top}$ in coarse thickness range.

The difference between $J_{ph,middle}$ and $J_{ph,top}$ (Figure 4.22) and the difference between $J_{ph,bottom}$ and $J_{ph,top}$ (Figure 4.23) have been represented to understand where the thicknesses region has to be refined. The goal is to find the section in both plots where $\Delta J_{ph} \sim 0$ for the same middle/bottom thicknesses ranges. This corresponds to the white strip, but only the low left-hand corner of these two colour maps fulfil the required conditions.

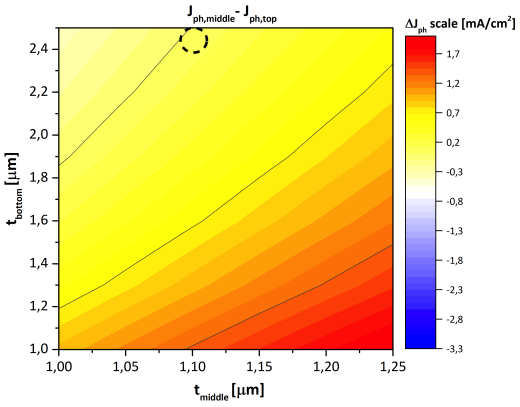

Figure 4.24: $J_{ph,mid}$ - $J_{ph,top}$ in refined thickness range.

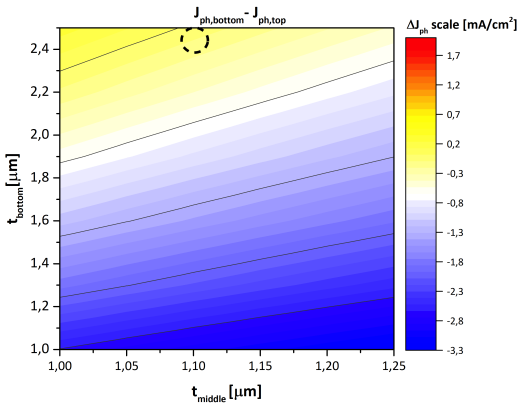

Figure 4.25: $J_{ph,bot}$ - $J_{ph,top}$ in refined thickness range.

The rang has been refined in that region and the new thicknesses intervals are 1 µm:0.05 µm:1.25 µm and 1 µm:0.3 µm:2.5 µm. Figure 4.24 represents the colours distribution of ΔJ_{ph} between middle and top sub-cells, while Figure 4.25 shows the colours distribution of ΔJ_{ph} between bottom and top sub-cells in refined ranges. The dashed circles designate which couple of thicknesses reaches the current matching conditions.

4.5.3. Thickness results

In Figure 4.26 two different outcomes have been exhibited as a function of the middle and bottom thicknesses variation. The black line points out the top sub-cell thicknesses used as input variables for the Matlab triple-junction current matching algorithm (Appendix B), each value is placed at the intersection of the corresponding middle and bottom layers thicknesses, thus each triplet of thicknesses has current matched sub-cells in the multi-junction structure.

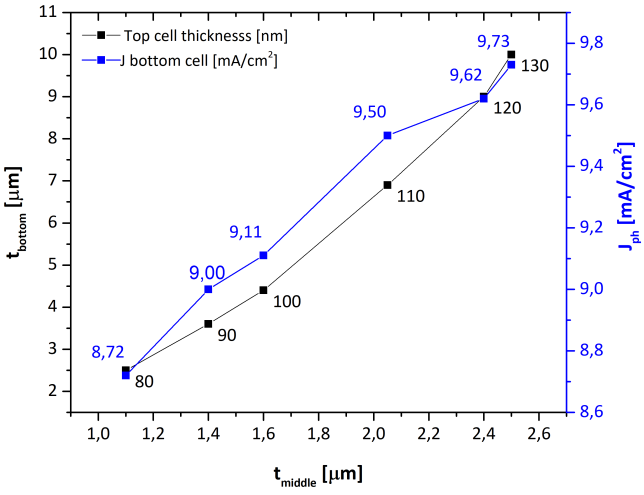

Figure 4.26: Combinations of optimised thicknesses in active layers (black trend) and photo-generated current density in the current limiting cell (blue trend).

While the blue line highlights the reached value in term of photo-current density for each thicknesses combination. These results represent the $J_{ph,bottom}$ because in each case the bottom sub-cell is behaving as the limit for the solar cell current. The top thicknesses have been varied in a broad range: from 80 nm to 130 nm with a step of 10 nm. Middle and bottom thicknesses scale up with it, as depicted in Figure 4.26. If the a-Si:H layer becomes thicker, then middle and bottom nc-Si:H layers increase their thickness as well. Furthermore, the thicknesses growth is consistent with the current density curve: a thicker multi-junction architecture with regard to intrinsic absorber layers generates higher photo-current density. However, the current matching findings have to deal with the device reliability, fabrication process and costs, and hence not all of them are feasible.

From a design point of view, thick active semiconductor layers are generally avoided, this has to do with high defect density (10^{16} cm^{-3}) of a-Si:H and nc-Si:H materials compared with c-Si [7]. The dangling bonds in these defected materials reduce the light-excited charge carriers lifetime due to the Shockley-Read-Hall recombination, as explained in Section 2.8 (Chapter 2). The diffusion length of carriers in hydrogenated materials are limited, especially for the amorphous one. Hence, the optimal thickness for active layers should not be larger than the diffusion length of charge carriers. If this is not the case, the generated electron-hole pairs do not transfer to the respective n/p-doped layers through the drift mechanism and unlikely recombine.

Furthermore, the n-coating is made by nc-SiOx in each p-i-n junction of the structure and behaves as an intermediate reflector layer with a low refractive index that redistributes light. For instance, the n-doped layer of the top sub-cell reflects back part of the light and enables a thickness reduction of a-Si:H absorber.

t_{top} [nm]	t_{middle} [µm]	t_{bottom} [µm]	$J_{ph,top}$ [mA/cm^2]	$J_{ph,middle}$ [mA/cm^2]	$J_{ph,bottom}$ [mA/cm^2]
80	1.1	2.5	8.74	8.77	8.72
90	1.4	3.6	9.04	9.10	9.00
100	1.6	4.4	9.34	9.19	9.11
110	2.05	6.9	9.60	9.50	9.50
120	2.4	9	9.93	9.70	9.62
130	2.5	10	10.16	9.79	9.73

Table 4.4: Sub-cells thickness combinations in current matching condition and their respective J_{ph} values.

Table 4.4 collects the simulated current matching conditions in terms of sub-cells thickness combinations and photo-current densities in the three intrinsic layers. The solutions are drawn attention to $J_{ph,bottom}$, because it is always the current limiting semiconductor. This is related to the fact that indirect bandgap materials such as nc-Si:H at the bottom cell have a smaller absorption coefficient than materials with a direct bandgap. The absorption path length of light at long wavelength requires 60 µm for red region and more than 100 µm for the infra-red region and this can not be compatible with the microcrystalline silicon layers that are commonly between 1 µm and 3 µm [7]. Furthermore, the following triple-junction analysis has been narrowed to a top sub-cell thickness range between 80 nm and 100 nm due to the considerations mentioned above.

4.5.4. Absorptance outcomes

Working at optimised thicknesses or in other words, reaching the current matching requirement allows achieving the maximum absorptance in the active absorber layers. Figure 4.27 depicts the graphical absorptance outcome when the triple-junction is simulated with 80 nm - 1.1 µm - 2.5 µm thicknesses combination for a-Si:H/nc-Si:H/nc-Si:H intrinsic layers. Each layer and coating at the interfaces provide an absorptance along the light spectrum. Therefore, a considerable amount of light is absorbed into FTO or reflected externally at the front side. The inactive layers should have the least possible amount of parasitic absorption because this accounts as optical losses for the solar device.

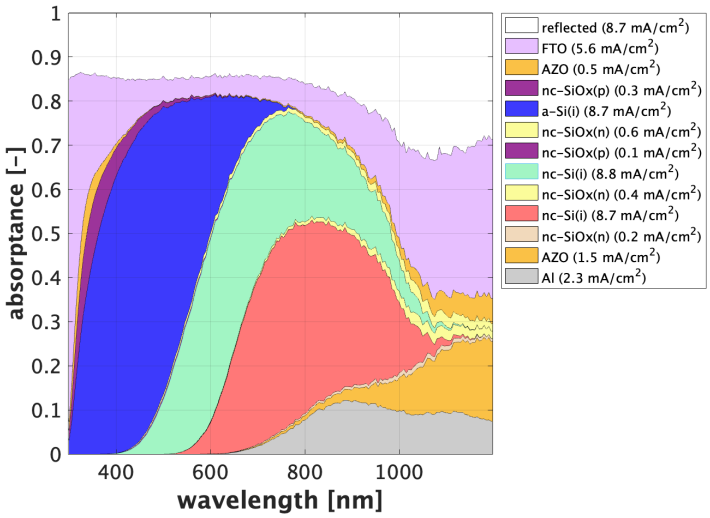

Figure 4.27: GENPRO4 absorptance output for each layer in triple-junction solar cell.

In addition, the area below each curve complies with:

$$R + T + \sum_{i=1}^{n} A_i = 1, \tag{4.9}$$

where the transmitted light at the rear side is close to zero for the entire light spectrum (T=0), the reflected component is fixed and given at the front side, while n reflects the overall number of layers. So for instance, FTO violet curve adds up all the absorptance of the layers below it (e.g. $A_{FTO,curve}$ = A_{FTO} + A_{AZO} + $A_{nc-SiOx(p)}$ +...+ A_{Al}) or AZO orange shape includes the whole layers underneath and AZO layer itself. This arrangement applies until the lowest layer.

In Figure 4.28 the active layers absorptance of three current matching cases has been represented as a function of the light spectrum. From left to right, the full lines indicates the absorbed light into the top-middle-bottom intrinsic layers where their respective thicknesses are 80 nm - 1.1

µm - 2.5 µm, the dashed curves likewise correspond to the absorptance of intrinsic materials at 90 nm - 1.4 µm - 3.6 µm, while the doted ones are at the thicknesses combination of 100 nm - 1.6 µm - 4.4 µm.

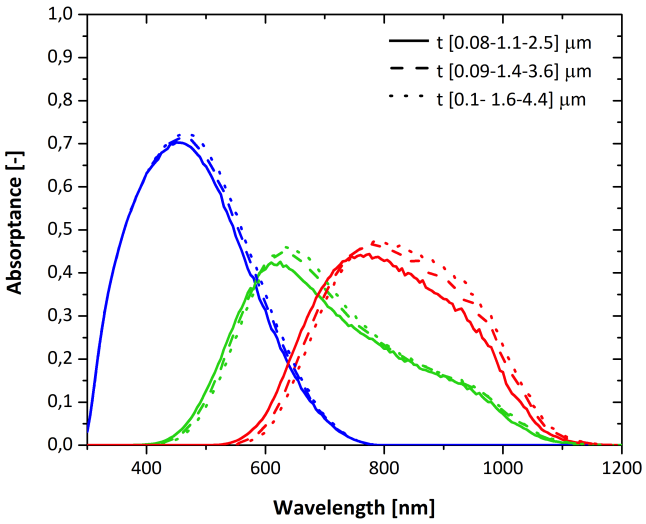

Figure 4.28: Active layers A for three examined thicknesses combinations in current matching condition.

Here, *i*-layer top cell has an absorption range between 300 nm and 700 nm that corresponds to blue range of light spectrum. The active layer of the middle cell covers the light spectrum between 400 nm and 1100 nm (green/yellow wavelength), whereas the bottom intrinsic layer performs from 600 nm to 1100 nm, mainly in the red and near infra-red region.

When a-Si:H is 80 nm thick, the absorptance peak is 0.7, while 1.1 µm of middle nc-Si:H finds its peak at 0.42 and the bottom nc-Si:H peak is at 0.44 with a material thickness of 2.5 µm. If the thickness of intrinsic layers increases, the absorptance peaks reach slightly higher values. For example, in the dashed case, the maximum are reached at 0.71-0.45-0.47 for top-middle-bottom absorptance respectively, while the peaks of the dotted representation are 0.73-0.46-0.48.

If absorber layers thicknesses increase, then a sizeable absorption enhancement is appreciable after the maximum peak of middle and bottom absorptance. Therefore, the thicknesses increase involves a visible improvement at long wavelength. This results in a shift of middle and bottom curves to red region of light spectrum and a gain in maximum absorptance for each sub-cell.

4.6. Back reflector

As shown in Figure 4.3, the thin-film multi-junction structure sandwiches the *p*-*i*-*n* junctions between front and back contacts. In general, the back reflector stack has three main functions. From the optical side, it minimises the transmission at the rear side and improves the light reflected back into the upper absorber layer. From an electrical side, it needs high electrical conductivity to operate as electric back contact.

In GENPRO4, the lowest interface of the triple-junction architecture has been developed as a sequence of three coatings. The nc-SiOx(n) is located below the bottom sub-cell *i*-layer and is characterised by high transparency. A thickness of 15 nm has been chosen as the optimal width for the reduction of electric field, as explained in Section 4.2.1. In addition, the second coating is made of 80 nm of transparent conductive oxide material that has been included with the same purpose of the silicon oxide. Further, an aluminium foil 300 nm thick is used with the aims of metallic back reflector and electric back contact.

4.6.1. Optical results with Al or Ag material as back reflector

The investigation has been focused on two different metals: aluminium and silver. The optical simulation results have been functional for the triple-junction fabrication with Al or Ag as a back reflector. Further experimental findings have been discussed in Chapter 5. The material selection is based on the reflectivity property of both materials: silver reflectivity is higher than that of aluminium. The former allows enhancing the solar cell optical properties, but in economic terms, it is available at higher prices than aluminium. Hence, Al material suits more applications than Ag due to its cost-effectiveness.

The triple-junction structure has been simulated by applying a singular change per each simulation in order to understand the variations in the optical solar cell behaviour. Initially, the current matching condition in term of active layers thickness has been studied for four different cases, where results have been summarised in Table 4.5. To proceed in this analysis, four separate cases have been set: FLAM01 texturing and 300 nm of Al as a third coating at the rear interface, FLAM01 textured interfaces and Ag 300 nm thick, Factory Baseline texturing and 300 nm of Al, Baseline textured interface and Ag 300 nm thick.

	FLAM01 texturing			*Factory Baseline texturing*		
BR material [300 nm]	t_{top} *[nm]*	t_{middle} *[μm]*	t_{bottom} *[μm]*	t_{top} *[nm]*	t_{middle} *[μm]*	t_{bottom} *[μm]*
Al	80	1.1	2.5	80	1.4	5.8
Ag	80	0.95	1.8	80	1.5	6.1

Table 4.5: Four analysed cases: current matched thicknesses in active layers depending on back reflector material and texturing.

The top sub-cell thickness has been taken as reference and constant among the simulations. By applying FLAM01 texturing, the triple-junction has shown a thicknesses reduction for middle and bottom i-layers with Ag as a back reflector (BR) instead of Al. This is in contrast with Factory Baseline textured interfaces: when the triple-junction is simulated with silver BR, the current matching condition is reached at thicker middle and bottom active layers.

	FLAM01 texturing			*Factory Baseline texturing*		
BR material [300 nm]	$J_{ph,top}$ *[mA/cm^2]*	$J_{ph,middle}$ *[mA/cm^2]*	$J_{ph,bottom}$ *[mA/cm^2]*	$J_{ph,top}$ *[mA/cm^2]*	$J_{ph,middle}$ *[mA/cm^2]*	$J_{ph,bottom}$ *[mA/cm^2]*
Al	8.74	8.77	8.72	7.23	7.01	7.05
Ag	8.76	8.94	8.93	7.23	7.22	7.22

Table 4.6: Four analysed cases: J_{ph} in active layers depending on back reflector material and texturing.

Table 4.6 presents the same four studied cases in term of active generated photo-current density. The mentioned thickness enhancement in Table 4.5 is consistent with the J_{ph} outcomes. FLAM01 texturing performs an optimal scattering by considering the surface roughness and its size features at interfaces. The silver material with higher reflectivity than aluminium makes the triple-junction structure thinner. However, optical results have been demonstrated that the bottom sub-cell optical performance is not improved with Ag and Factory Baseline texturing. As a matter of fact, the silver back reflector does not provide any J_{ph} improvement, instead it requires slightly thicker middle and bottom nc-Si:H layers to reach matched photo-current densities of 7.22 mA/cm^2.

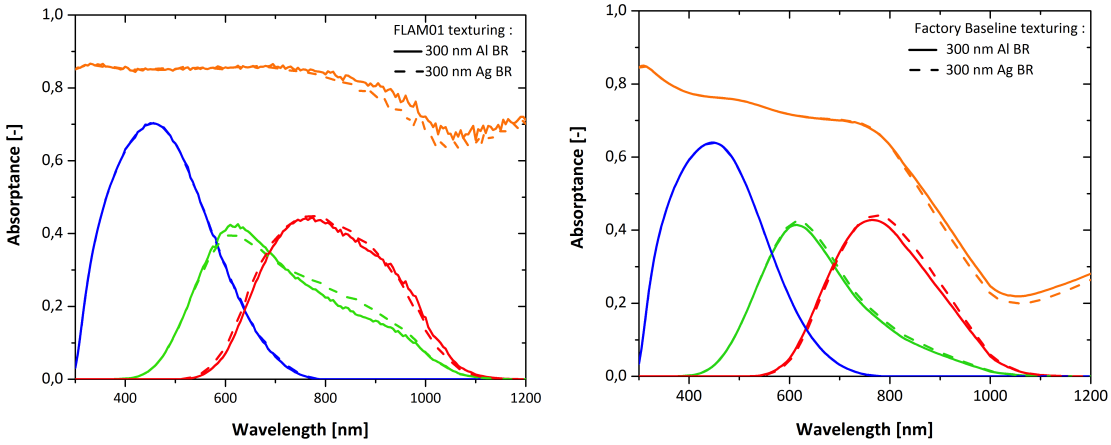

(a) FLAM01 texturing

(b) Factory Baseline texturing

Figure 4.29: Four analysed cases: total and active layers A depending on back reflector material and texturing.

Figure 4.29 depicts the active sub-cells layers absorptance and total device absorptance among four simulated cases. FLAM01 texturing exhibits a slight improvement in absorbed light in the near infra-red region of the light spectrum. Silver back reflector scatters more light back into the bottom sub-cell and influences accordingly the middle nc-Si:H(i). In terms of total absorptance, a material such as Ag that reflects more, also implies a reduction of parasitic absorption. Ag back reflector decreases the light absorption losses at long-wavelength. The red light incoming at the rear interface is subjected to an enhancement of the path-length, and this causes additional photo-generation (Figure 4.29a).

Moreover, Figure 4.29b represents the triple-junction optical behaviour when interfaces are textured with Factory Baseline and Al or Ag metals are applied as a back reflector. The drop of total absorptance and the rise of bottom absorber layer in the near infra-red region are analogous to the previous case.

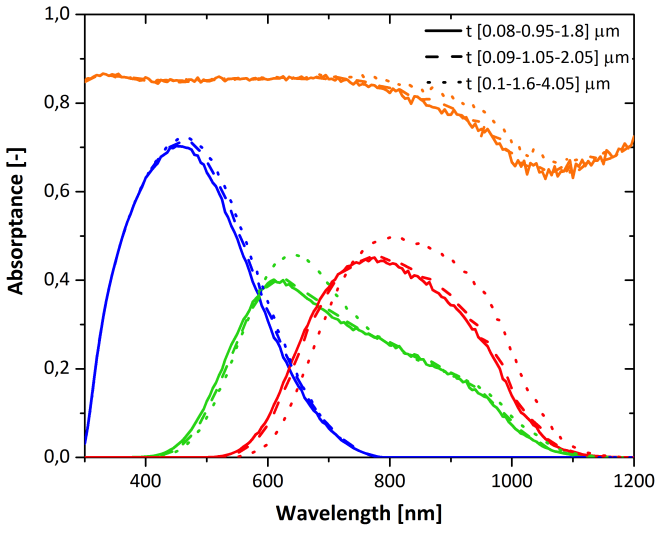

Figure 4.30: Total and active layers A for three examined thicknesses combinations in current matching condition with Ag as a back reflector.

Figure 4.30 analyses the total and active layers absorptance with silver material as a back reflector. Three thicknesses combinations in current matching condition have been investigated and the top sub-cell assumes the same values as the case with aluminium back reflector. The full line curves find the top-middle-bottom absorptance peaks at 0.7-0.4-0.45 respectively, the dashed case at 0.71-0.4-0.46 and the dotted curves at 0.72-0.46-0.5. Compered with Figure 4.28, the silver back reflector enhances the absorptance of middle and notably bottom sub-cells through the increase of absorber layers thicknesses. The total triple-junction absorptance is not visibly affected by it, because the reduction of optical losses in the rear reflector stack is balanced with more light reflected back in the upper p-i-n junction.

Looking at Table 4.7, it is possible to assert the level of photo-current densities achieved with Al back reflector (Table 4.4) can be reached in a thinner triple-junction architecture by means of Ag back reflector. Additionally, Subsection 4.5.3 has elucidated several reasons behind the possibility of fabricating only a few combinations of active layers thickness. Here, the investigated thicknesses are more feasible than Al BR in triple-junction structure. The middle and bottom active layers vary in a thickness range that is potentially applicable for the fabrication of the solar cell.

t_{top} [nm]	t_{middle} [μm]	t_{bottom} [μm]	$J_{ph,top}$ [mA/cm^2]	$J_{ph,middle}$ [mA/cm^2]	$J_{ph,bottom}$ [mA/cm^2]
80	0.95	1.8	8.76	8.95	8.93
90	1.05	2.05	9.09	8.92	8.97
100	1.6	4.05	9.34	9.49	9.54
110	1.8	4.75	9.61	9.55	9.56
120	1.9	5.1	9.86	9.48	9.53
130	2.1	5.9	10.07	9.55	9.55

Table 4.7: Sub-cells thicknesses combination in current matching conditions with Ag as BR and their respective J_{ph} values.

Figure 4.31 combines the thicknesses triplet in current matching condition through the black pattern, while blue results highlight the respective photo-current densities. The improved photo-generation at the bottom nc-Si(i) entails a change in the current limiting sub-cell. In this case, the top sub-cell acts as the limit for the J_{ph}. Whereas with Al BR, the bottom sub-cell is limiting the current of the solar device as displayed in Figure 4.26. By comparing these two scenarios, the total current utilization of the triple-junction cell is determined by the bottom cell with Al BR and if the thickest structure with 130 nm a-Si:H is taken into account, then it reaches 29.19 mA/cm^2, whereas the total current utilization is determined by the top cell with Ag BR and enhances to 30.21 mA/cm^2.

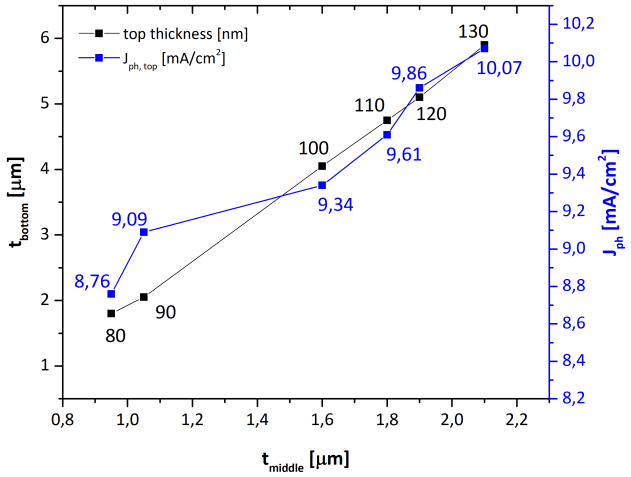

Figure 4.31: Combinations of optimised thicknesses in active layers (black trend) and their respective J_{ph} in the current limiting cell (blue trend) with Ag BR.

The following optical modelling simulations have been focused on Ag BR by narrowing progressively down its thickness. The benchmark case is with 300 nm Ag BR, which has been reduced to 15 nm at first, then downsized to 5 nm and removed for the latest. In this latter case, the rear interface consists of two coatings: n-doped nc-SiOx coating belonging to bottom cell and 80 nm Al-doped ZnO material.

Figure 4.32 compares the four simulations among the active layers absorptance, where the thinning effects merely the near infra-red wavelength of the spectral utilisation. A decrease of Ag BR thickness implies a decrease of absorptance when the wavelength is higher than 800 nm. The reduction is mainly visible in the middle (green) and bottom (red) sub-cell curves.

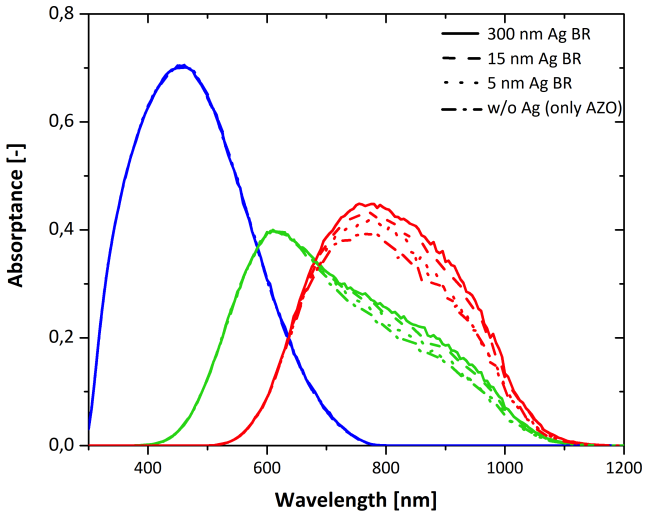

Figure 4.32: Active layers A when Ag (BR) thickness is scaled down.

For a comprehensive analysis, Figure 4.33 plots the three main optical properties for each case: the total triple-junction absorptance is depicted in orange, the reflectance at the front side in magenta and the transmittance at the back side in light-blue colour.

The thickness reduction of the metallic contact worsens the photo-generation of sub-cells working above 800 nm and therefore, this leads to more optical losses. A fundamental requirement of the back reflector is linked with the transmitted light outward the solar cell. If the BR is 15 nm or 5 nm

thick, then the absorptance and reflectance become less effective and more light escapes through the back. In the simulation without any metallic back reflector and only AZO, the light at wavelength above 800 nm is 30% transmitted out through the rear side of the multi-junction device. The transmittance turns into the major optical loss: less light is reflected at the front and absorbed in nc-Si(i) layers.

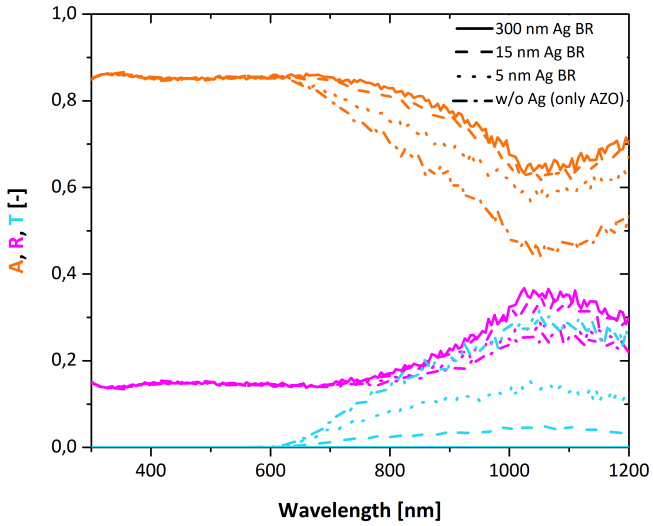

Figure 4.33: Total A, front side R, back side T when Ag (BR) thickness is scaled down.

The studied cases underline a direct correlation between absorptance and transmittance. Thinning gradually the metallic BR involves likewise absorptance decrease and transmittance increase. Figure 4.32 and Figure 4.33 show a trade-off between the absorptance improvement in the red part of the light spectrum and the optical losses due to the transmission of light at the rear side.

Table 4.8 investigates the four BR configurations in term of photo-current density generated in each intrinsic layer. The Ag thickness is bounded in a range between 300 nm and 15 nm, below which the metal reflectivity drops and the material becomes more transmissive. This is also reflected by a decrease of $J_{ph,middle}$ and $J_{ph,bottom}$.

Ag BR thickness [nm]	$J_{ph,top}$ $[mA/cm^2]$	$J_{ph,middle}$ $[mA/cm^2]$	$J_{ph,bottom}$ $[mA/cm^2]$
300	8.76	8.94	8.93
15	8.77	8.76	8.54
5	8.77	8.51	8.10
only AZO	8.75	8.31	7.73

Table 4.8: Active layers J_{ph} when Ag (BR) thickness is scaled down.

Furthermore, the baseline BR configuration with (AZO and 300 nm Al) has been compared to a back reflector structure with AZO and 15 nm Ag, and a BR arranged only with AZO. Note the cases have been simulated with different top-middle-bottom thicknesses combinations in order to respect the current matching requirement, refer back to Table 4.5. In terms of absorptance (Figure 4.34a), there are no visible implications between the cases represented by full and dashed lines. However, AZO as back reflector shows an overall decrease of total A consistent with an absorption drop in active layers above 800 nm. This is then explained in Figure 4.34, dotted case results in a transparent back reflector, hence absorptance and reflectance reduce in the near infra-red of light spectrum. If the Al BR was replaced with more reflective material such as Ag, the optical properties would be preserved and ultimately this would allow a thinner triple-junction structure.

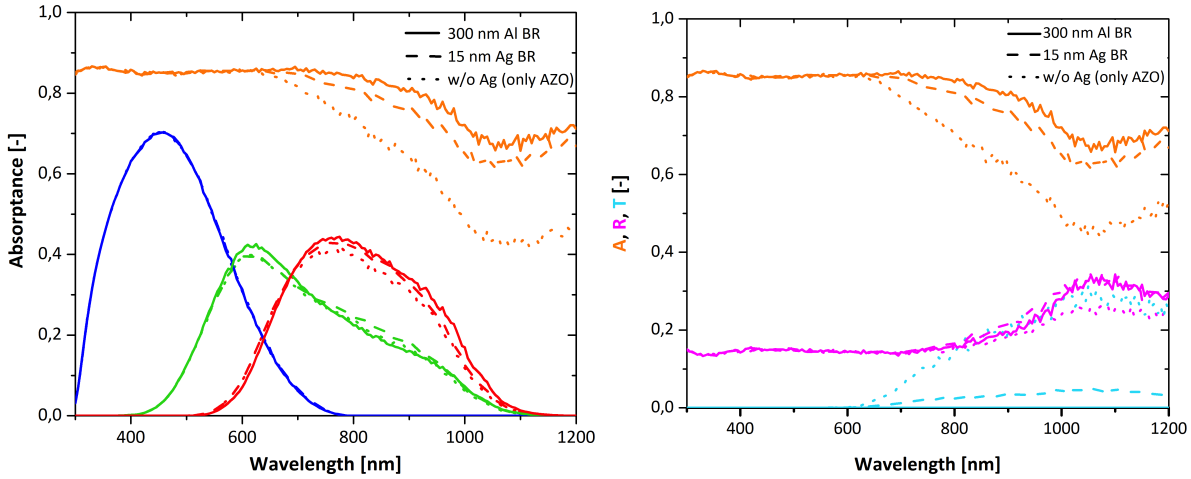

(a) Total and active layers absorptance (A)

(b) Total absorptance (A), reflectance (R) and transmittance (T)

Figure 4.34: 300 Al, 15 nm Ag and AZO as BR.

4.6.2. Ag back reflector with different light models and texturing

As stated earlier in Section 4.4.2, the textured interfaces require size features compatible with the wave or ray model. An apparent analogy can be found when FLAM01 texturing is used with Al or Ag back reflector (Figure 4.35a), and similarly with Factory Baseline texturing (Figure 4.35b). To get a better understanding of light validation steps, the reader is invited to refer to the explanation in Section 4.4.2. The triple-junction configuration with FLAM01 texturing exhibits an increase of optical losses when the ray tracing model is partially replaced with wave model (II scenario) or when the scalar scattering theory is applied at each interface. (III scenario). II scenario is related to the absorption region of long wavelength. III scenario drops the absorption in each sub-cell and consequently, the total absorptance visibly reduces from short wavelength (above 300 nm). Hence, even if the metallic back reflector changes its material and its reflective properties, the FLAM01 texturing is still inconsistent with the scalar scattering theory.

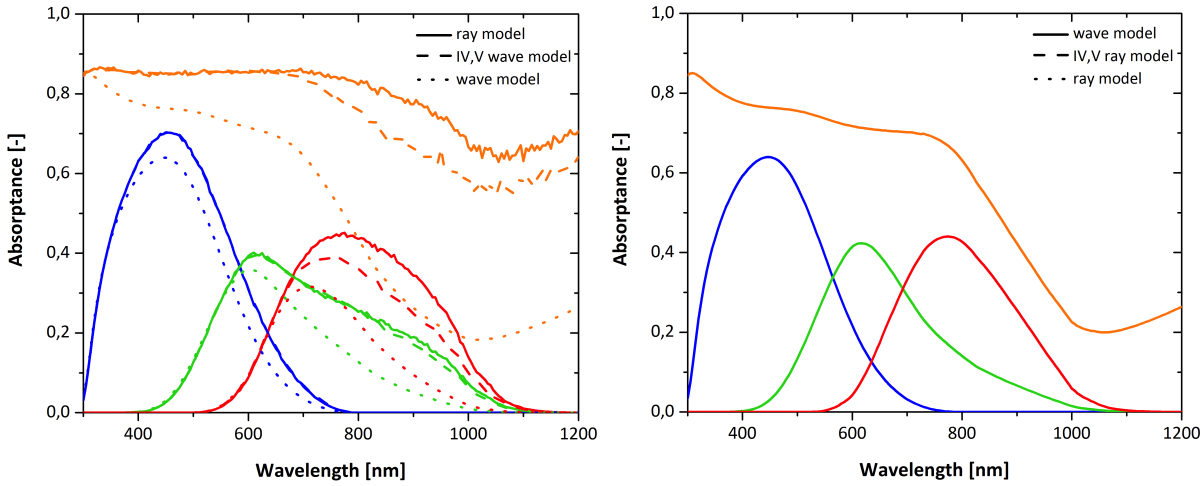

(a) FLAM01 texturing

(b) Factory Baseline texturing

Figure 4.35: Total and active layers A comparison among three scenarios with ray and wave models (two examined texturing).

On the other hand, the implementation of a partial of full ray tracing reveals inconsistency between the Factory Baseline size features and the light model. As shown in Figure 4.35, diffraction persists as the main optical effect at interfaces, and hence I, II, III scenarios exhibit the same behaviour.

The J_{ph} differences have been underlined in Table 4.9 when interfaces are modelled with FLAM01 texturing. A discrepancy between texturing and light modelling results in photo-current density decrease among absorber layers. The displayed results are an analogy to Table 4.3. The optimal photo-generation also relies on the light modelling. If it is not suitable, the J_{ph} reduction occurs regardless the material implemented at the back reflector.

$FLAM01 texturing and AgBR$			
$Light\ model$	$J_{ph,top}$ (mA/cm^2)	$J_{ph,middle}$ (mA/cm^2)	$J_{ph,bottom}$ (mA/cm^2)
I scenario	8.76	8.94	8.93
II scenario	8.80	8.76	7.54
III scenario	7.26	6.26	5.05

Table 4.9: J_{ph} of active layers among three different scenarios. Simulations with FLAM01 texturing and Ag (BR).

4.7. Sensitivity analysis

This section has been dedicated to the investigation of sensitive variation among sub-cells thickness. The simulations have been performed by altering ± 5% of each sub-cell thickness among three different configurations in current matching condition. The a-Si:H layer has assumed the values of 80 nm, 90 nm or 100 nm. In general, the layers deposition may be subjected to small thickness variation during the solar cell fabrication, and this can impact the device efficiency and the working performance. The optical properties such as absorptance, reflectance and transmittance of the multi-junction solar device have not provided any significant change. The investigation has been focused on the photo-generated current densities when a thickness variation occurs in the intrinsic layers.

When a sub-cell varies its thickness of ± 5%, the three J_{ph} values of intrinsic layers change as well. An example is offered in Figure 4.36: 80 nm of top sub-cell thickness has been changed by adding or subtracting 5%, meaning t_{top} may be 76 nm or 80 nm or 84 nm thick. Hence, the triple-junction solar architecture has been simulated three time. Each simulation has used one of the three top sub-cell thicknesses of interest and maintained fixed middle and bottom sub-cells thicknesses, 1.1 µm and 2.5 µm respectively.

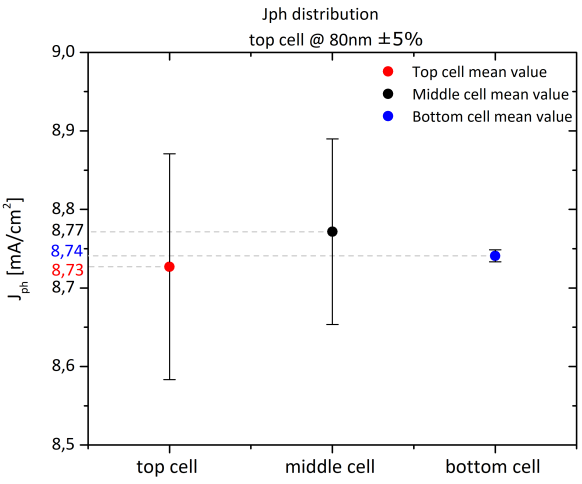

Figure 4.36: J_{ph} distribution with [80±5% nm - 1.1 µm - 2.5 µm].

The most affected J_{ph} is the one of the top sub-cell because it is involved in the thickness change of the a-Si:H(i) layer, and this is also suggested through the its standard deviation from the J_{ph} mean value. It influences also the middle and bottom photo-generation, $J_{ph,middle}$ varies from its mean value in a range of ± 0.1~0.2 mA/cm^2 as $J_{ph,top}$, whereas $J_{ph,bottom}$ is not influenced by the variation of top cell thickness. Thus, top and middle sub-cells are more sensitive in term of photo-current density than the bottom one. If the intrinsic a-Si:H layer is thinner, less light absorption occurs, and therefore more light is absorbed by the middle nc-Si:H(i) material. If the intrinsic a-Si:H layer is thicker, then the opposite optical effect takes place.

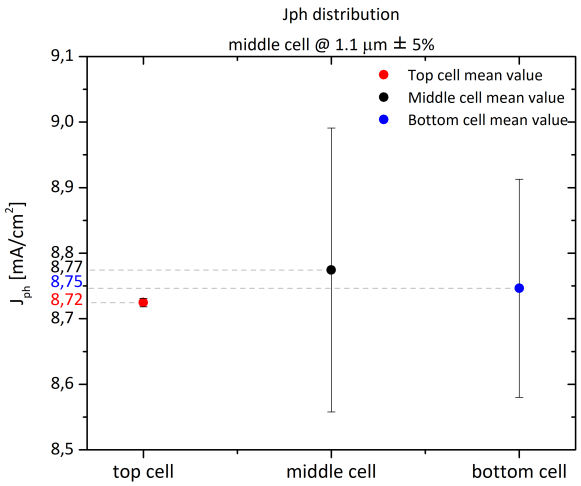

Figure 4.37: J_{ph} distribution with [80nm - 1.1±5% µm - 2.5 µm].

Figure 4.38 follows the same sensitivity analysis. In this case, the sub-cell of concern is the middle one. The ± 5% middle cell thickness variation influences more the $J_{ph,bottom}$ instead of the $J_{ph,top}$. As shown in Figure 4.36, lower photo-current density generated in the middle intrinsic layer corresponds to higher $J_{ph,bottom}$ and vice versa. Furthermore, $J_{ph,bottom}$ varies from its mean in a range of ± 0.1 ~ 0.2 mA/cm^2 as $J_{ph,middle}$, whereas $J_{ph,top}$ is not influenced by the middle cell thickness change.

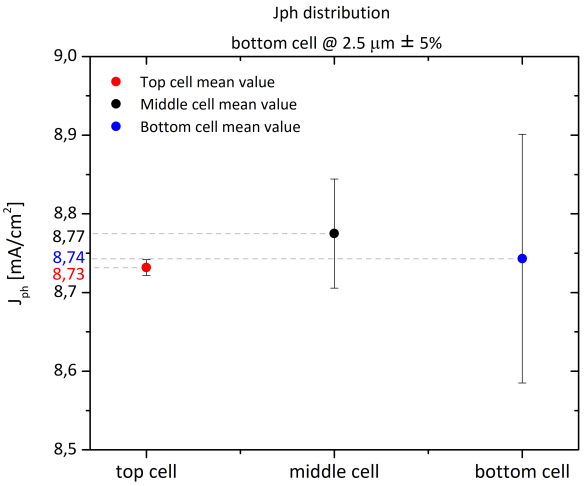

Figure 4.38: J_{ph} distribution with [80nm - 1.1 µm - 2.5±5% µm].

Afterwords, the simulations have been implemented when the thickness variation involves the bottom sub-cell. Figure 4.38 points out photo-current densities are less sensitive when the thickest active absorber layer of the multi-junction is slightly over/under-sized. The ± 0.1~0.2 mA/cm^2 fluctuation is only related to bottom cell, whereas the standard deviation of top and middle sub-cells indicates no significant photo-generation changes.

In order to validate the results above, the analysis has been extended for other combinations of current matched thicknesses, which have been collected in the left column of Table 4.10. The goal is to find a trend for the standard deviation of the photo-current density when a singular active layer is subject to thickness alterations. More specifically, the values in each row have been calculated by considering nine cases in total and then the ΔJ_{ph} for top-middle-bottom active layers. For example, in the first row the nine mentioned cases are the outcome of ± 5% t_{top}, where t_{top} may be 80 nm or 90 nm or 100 nm thick depending on the studied thicknesses triplet. Then, for each combination the respective $J_{ph,top}$, $J_{ph,middle}$ and $J_{ph,bottom}$ values have been used to estimate the average standard deviation.

Thickness variation	*Average J_{ph} standard deviation*		
	$J_{ph,top}$ (mA/cm^2)	$J_{ph,middle}$ (mA/cm^2)	$J_{ph,bottom}$ (mA/cm^2)
Top sub-cell 80 nm, 90 nm, 100 nm	0.15	0.12	0.01
Middle sub-cell 1.1 µm, 1.4 µm, 1.6 µm	0.01	0.21	0.13
Bottom sub-cell 2.5 µm, 3.6 µm, 4.4 µm	0.01	0.06	0.15

Table 4.10: The standard deviation of active layers J_{ph} among investigated triplets of current matched thicknesses.

This sensitive study has pointed out the thickness variation of top sub-cell modifies mainly the optical behaviour in the middle i-layer and the top i-layer itself. The variations of the middle sub-cell thickness impact exclusively the bottom sub-cell. Small fluctuations in the bottom nc-Si:H(i) layer do not deviate the J_{ph} values in the other sub-cells. Therefore, the latter case is the one that ensures better the current matching requirement, whereas the variation of middle sub-cell is the most sensitive scenario. $J_{ph,middle}$ is expected to vary by ± 0.21 mA/cm^2 and $J_{ph,bottom}$ by ± 0.13 mA/cm^2.

Additional outcomes about sensitivity analysis have been included in Appendix C. Figures from C.1 to C.3 depict the active layers and total absorptance when matched currents are at 80 nm - 1.1 µm - 2.5 µm (top-middle-bottom cells thickness) and ± 5% variation is implemented at each intrinsic layer per time. Hence, no considerable deviation from the baseline thicknesses combination has been found in term of absorptance. Further graphs show the J_{ph} distribution for all the other studied cases, which have been shown partially through plots in this section and summarised in Table 4.10.

4.8. Encapsulation

The sections above have yielded optical results through a triple-junction structure with FTO as the front layer. This section and the following ones have included the encapsulant in the optical simulations, which allows to better predict the optical behaviour of solar products delivered by HyET. The encapsulant layering is illustrated in Figure 4.39. Additionally, the Matlab code in Appendix A has modelled the encapsulant stack as an interface coated by four media between air and FTO layer.

Several grounds carry to including the encapsulation in the solar multi-junction architecture: it operates as a protection from the environment and improves the light management by decreasing the reflection losses at the front side. Hence, the encapsulant integration has aimed to provide a more realistic prediction of the triple-junction optical properties.

ETFE (25 µm)
glue (90 µm)
ETFE (25 µm)
glue (90 µm)

Figure 4.39: Encapsulant structure at the triple-junction front side used by HyET Solar.

The ethylene tetrafluoroethylene, also known as ETFE, is a fluorine-based polymer and is a material characterised by high electrical and thermal-energy radiation resistance [58]. The ETFE refractive index is 1.43, whereas glue has a refractive index of 1.53 [50]. Since the encapsulant goal is to reduce the total reflectance, the ETFE and glue coatings have a negligible light absorption and contribute mainly to the increase of light trapping. Accordingly, this also results in a solar device enhancement in terms of performance and efficiency.

4.8.1. Anti-reflective coatings (ARC) & refractive index grading

Light management helps to design the solar cell architecture and optimise its optical/electrical properties. In Section 4.3, the light management has been tackled from the point of light in-coupling. The texturing analysis has been focused on the reduction of reflectance and the increase of absorptance in active absorber layers (a-Si:H/nc-Si.H/nc-Si:H). Here, the complementary side of the light management has been developed in regard to the integration of anti-reflection coatings at the front side of the device. In general, ingoing light to a surface between two layers with different refractive indices splits into reflected and transmitted parts. Hence, it is important to minimise the reflective losses, which may be analysed roughly through Fresnel equations 2.4 (Chapter 2). If two media divided by an interface have a wide refractive index difference, Fresnel equations point out that significant optical losses are due to high reflectivity.

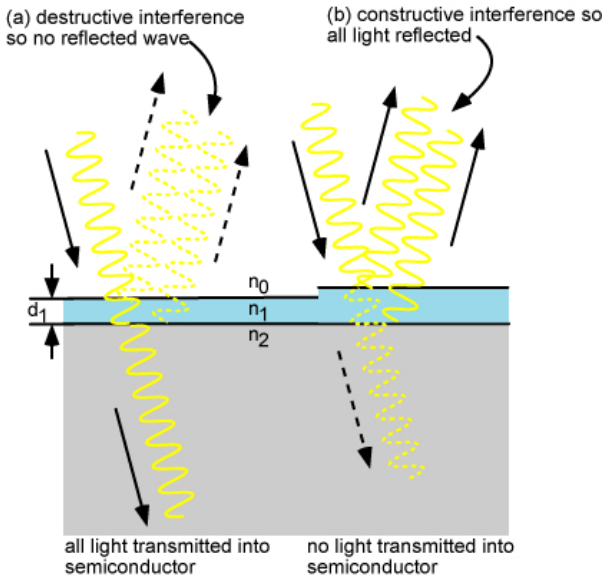

Figure 4.40: ARC with 1/4 wavelength for the minimisation of interface reflection [22].

Figure 4.40 sketches how the destructive interference is a light property that can reduce the optical losses by embedding an ARC. The air refractive index is indicated with n_0, n_1 for ARC and n_2 for the semiconductor material. The right designed structure is the non-desirable case, where

the incoming light is completely reflected back and not transmitted in the medium with n_2 due to constructive interference at the interface. Instead, the left situation depicts the destructive interference effect in ARC with a well-defined thickness, hence the upper ARC surface (air/ARC) generates a reflected wave that is anti-phase with the one at the lower ARC surface (ARC/semiconductor). Therefore, by adding up these two components the resulting reflected wave is equal to zero and the reflection losses are minimised.

In order to achieve a destructive interference effect, ARC thickness is chosen taking into consideration the wavelength in this material has to be one quarter the wavelength of the incident light at the air/ARC surface. Hence, an ARC with 1/4 wavelength, n_1 as refractive index and a free-space wavelength λ_0 of the ingoing light minimises the reflection when its thickness d_1 is calculated as [7]:

$$d_1 = \frac{\lambda_0}{4n_1}. \tag{4.10}$$

Furthermore, the refractive index n_1 has to satisfy an additional condition to reach the minimum reflection, its optimal value is found as the geometric mean of n_0 and n_2, $n_1 = \sqrt{n_0 \cdot n_2}$ [7]. In addition, the thickness and reflective index of each layer are directly dependent on the light wavelength. They have been calculated at 600 nm to minimise the reflection losses in correspondence with the peak power of the solar irradiance spectrum shown in Figure 2.2 (Chapter 2).

In the encapsulant development, more than one coatings have been included in the interface between air and FTO, this optical procedure is known as refractive index grading and allows to decrease the reflection even further. The GENPRO4 ".nk" data have allowed implementing ARC at air/FTO interface as follow:

Materials stack	*n @ 600 nm*
air	1
ETFE	1.43
glue	1.53
ETFE	1.43
glue	1.53
FTO	1.902

Table 4.11: Refractive index grading structure with materials and n values at 600 nm.

4.8.2. ARC simulation outcomes

The analysis has been started with a comparison in terms of total device absorptance and intrinsic materials absorptance when the current matching requirement occurs at top-middle bottom thicknesses combination of 80 nm - 1.1 µm - 2.5 µm respectively. In Figure 4.41 the full line behaviours represent the integration of an encapsulant structure (Figure 4.39) at the front interface. The dashed curves stand for the baseline configuration, where the front device interface is simply FLAM01 textured without any coatings. Since the encapsulation is placed above the front reflector, the refractive index grading provided by ARC boosts visibly the light absorption at short wavelength, which is the working range of the top sub-cell. The blue curve peak shifts from 0.7 to 0.75, whereas the ARC is less effective for the absorptance in the middle and bottom sub-cells.

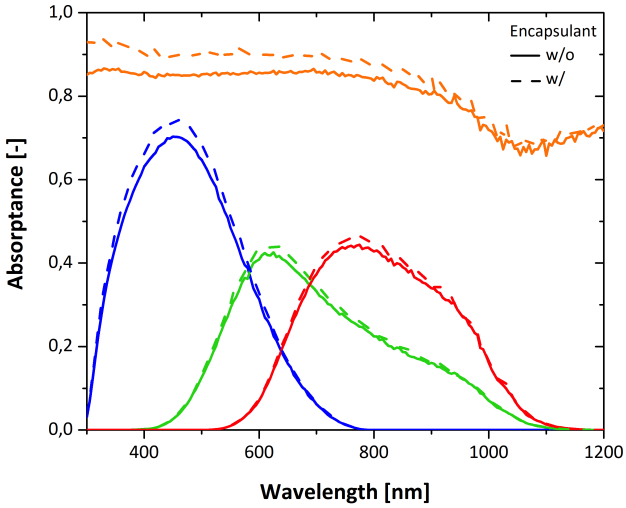

Figure 4.41: Total and active layers A with and without encapsulant.

The respective photo-current densities for the two examined cases have been illustrated in Figure 4.42. The J_{ph} without encapsulant in solar cell architecture have been represented in black, whereas the red J_{ph} values include the encapsulant. Here, the optical improvement provided by the ETFE stack may also be seen through photo-generated currents. In both cases the bottom sub-cell is the limiting current. The top sub-cell is the one most boosted up since the encapsulant embedding enhances mainly the light absorption at short wavelength. Dealing with amorphous materials entails the light-induced degradation as already explained in Section 3.2.2 (Chapter 3), here the encapsulant mitigates the Staebler-Wronski effect on the currents mismatch. On one hand, the current matching requisite does not occur anymore: it is possible to notice a slightly mismatched among the results connected by red line. On the other hand, the $J_{ph,top}$ increase is functional for the performance of the triple-junction above a thousand of hours. After that, the photo-current generated in the top cell stabilises at a lower value, but closer to middle and bottom J_{ph} values than in the case without encapsulant.

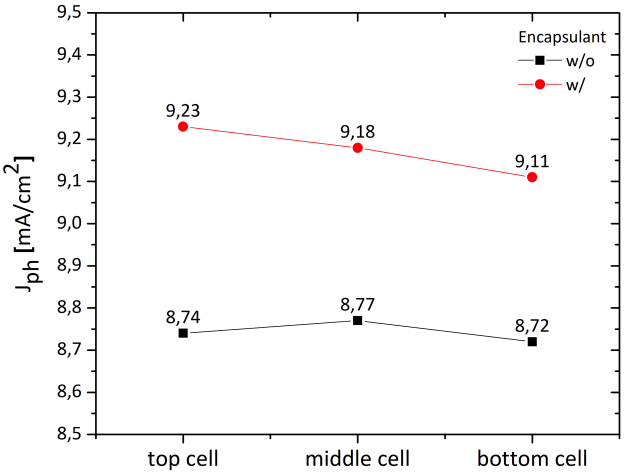

Figure 4.42: Active layers J_{ph} with and without encapsulant.

Furthermore, Table 4.12 provides an estimation of the percentage variation and enhancement through the encapsulant incorporation. Among sub-cells the delta J_{ph} is 0.43 mA/cm^2 on average and the light trapping contributes by more than 4% among active layers, notably in the top one where the gain is about 5.6%. Thus, the percentage variation has been calculated through the formula below:

$$PercentageVariation(\%) = \frac{J_{ph,encapsulant} - J_{ph,no/encapsulant}}{J_{ph,no/encapsulant}} \cdot 100. \tag{4.11}$$

Sub-cell	*Top*	*Middle*	*Bottom*
J_{ph} *(mA/cm^2) w/o encapsulant*	8.74	8.77	8.72
J_{ph} *(mA/cm^2) w/ encapsulant*	9.23	9.18	9.11
ΔJ_{ph} *(mA/cm^2)*	0.49	0.41	0.39
Percentage Variation (%)	5.61	4.68	4.47

Table 4.12: J_{ph} percentage variation among intrinsic layers.

Looking at the front device reflection, the refractive index grading provided by the encapsulant has decreased the reflective losses and therefore enhanced the light transmission to active layers. The bar graph of Figure 4.43 presents the photo-current densities values: the reflected $J_{ph,ref}$ may also be interpreted as the light absorbed by air layer with an infinite thickness above the front side of the multi-junction structure. Here, the encapsulant reduces $J_{ph,ref}$ by more than 1.6 mA/cm^2.

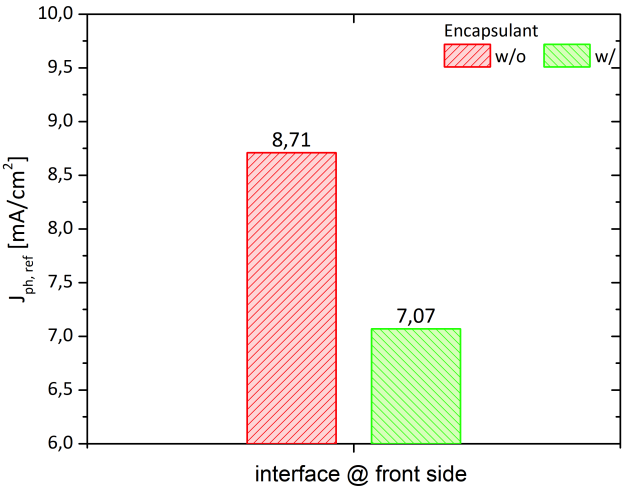

Figure 4.43: Reflected J_{ph} at the front side with and without encapsulant.

The investigation has subsequently been widened and the other two thicknesses combinations have been taken into account. The table in Figure 4.44 aims to recapitulate the analysed thicknesses configurations, which have balanced J_{ph} among i-layer of sub-cells.

Thicknesses combinations in current matching condition			
Combination	I	II	III
Top sub-cell	80 nm	90 nm	100 nm
Middle sub-cell	1.1 µm	1.4 µm	1.6 µm
Bottom sub-cell	2.5 µm	3.6 µm	4.4 µm

Figure 4.44: Recap of thicknesses combination used for simulations with embedded encapsulant in the triple-junction simulations.

After this clarification, attention has been paid to the photo-current density improvement among the three mentioned scenarios. As in I case, II and II scenarios have pointed out the Staebler-Wronski effect is attenuated by the encapsulant and the deliverable current for the solar device is then limited by the top sub-cell. Additionally, the encapsulant properties have less impact in the red part of light spectrum where the bottom sub-cell performs more. Considering Table 4.13, the encapsulation improves the current densities by 0.5 mA/cm^2 on average. Moreover, a thicker triple-junction structure as in III scenario does not compromise the encapsulant properties, thus the photo-generation gains by the same averaged delta as the other two thinner scenarios.

Active layers thicknesses combination	*w/o encapsulant*			*w/ encapsulant*		
	$J_{ph,top}$ [mA/cm^2]	$J_{ph,middle}$ [mA/cm^2]	$J_{ph,bottom}$ [mA/cm^2]	$J_{ph,top}$ [mA/cm^2]	$J_{ph,middle}$ [mA/cm^2]	$J_{ph,bottom}$ [mA/cm^2]
I	8.74	8.77	8.72	9.23	9.18	9.11
II	9.04	9.10	9.00	9.56	9.49	9.40
III	9.34	9.19	9.11	9.87	9.58	9.51

Table 4.13: J_{ph} comparison between encapsulated or not encapsulated triple-junction structure in three different current matching conditions.

Similarly, Figure 4.45 displays the same examined cases through the analysis of $J_{ph,ref}$ behaviour. The red columns of the histogram represent non encapsulated configuration and draw attention to a slight values reduction by thickening a-Si/nc-Si/nc-Si layers. Hence, the reflective losses may be scaled down through this approach subjected to thickness boundaries discussed in Subsection 4.5.3. Besides, this optical aspect gives rise to ARC embedding which minimises $J_{ph,ref}$ even further. The mean $J_{ph,ref}$ reduction is about 1.6 mA/cm^2 that is roughly redistributed in the same amount among the active layers, the gain of photo-current densities is about 0.5 mA/cm^2 per each intrinsic absorber material.

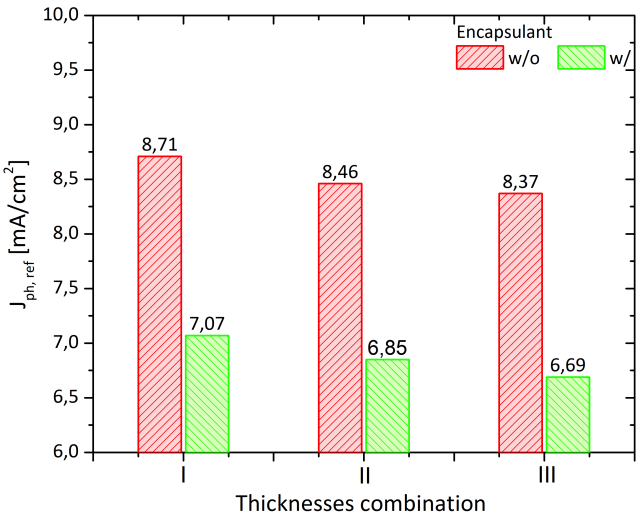

Figure 4.45: Reflected J_{ph} among thicknesses combinations in c.m.

Afterwords, the investigation of anti-reflective coatings has moved to the thicknesses of ETFE coatings since their optimisation is fundamental for the optical modelling and then, for the encapsulation process that takes place at HyET Solar company. Figure 4.39 sketches the encapsulant stack coated by two ETFE layers sandwiched between two layers of glue with fixed thickness of 90 µm each. Whereas both ETFE coatings have been chosen with a thickness of 25 µm by the evaluation of photo-generation optimisation. Table 4.13 underlines the optical improvements of the encapsulant are less effective on the bottom sub-cell photo-current density, hence the ETFE thicknesses optimisation has been developed in respect of this sub-cell. Initially, the thicknesses of ETFE materials have been varied in a range from 10 µm up to 100 µm as shown on x-axis in the plots. The same thickness value has been taken for both ETFE layers for the simulations.

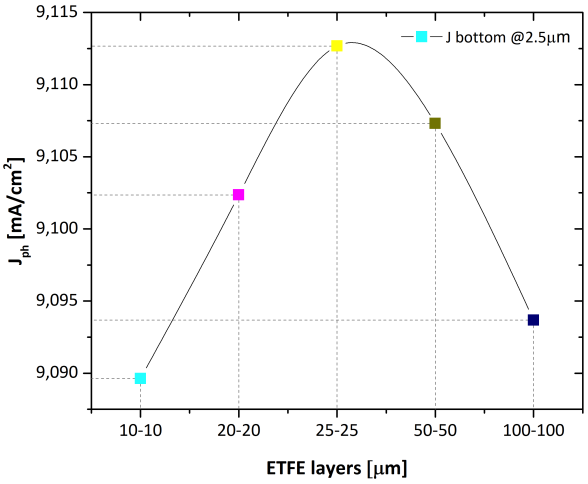

Figure 4.46: $J_{ph,bottom}$ for different ETFE thicknesses.

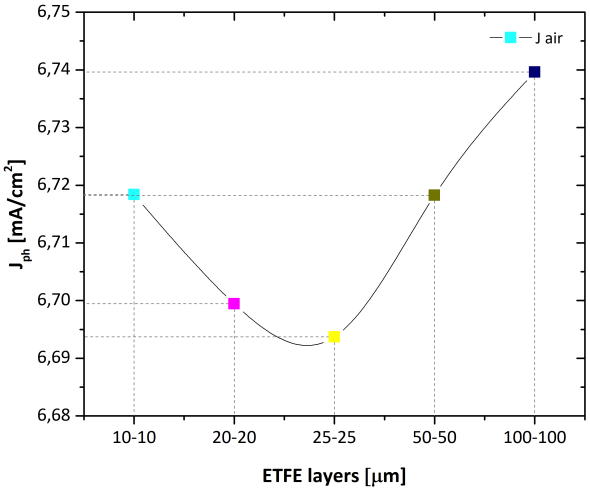

Figure 4.47: $J_{ph,air}$ for different ETFE thicknesses.

Figure 4.46 highlights an increasing trend of $J_{ph,bottom}$ until the thickness of 25 µfor both ETFE coatings. Any additional increase of ETFE thicknesses results in lower $J_{ph,bottom}$. Hence, the maximum $J_{ph,bottom}$ is reached when both ETFE coatings are both 25 µthick. Therefore, Figure 4.47 depicts $J_{ph,ref}$ at the front side, which is coherent with the graph on the left. It can be seen that the maximum $J_{ph,bottom}$ and the minimum $J_{ph,ref}$ are found at the same ETFE thicknesses.

A space matrix has been analysed to verify if heterogeneous thickness combinations would have given additional enhancement as illustrated in Figure 4.48. Here, En1 and En2 stand for the upper and lower ETFE coatings of the encapsulant stack respectively. Therefore, the triple-junction structure has been simulated for each combination between 10 µm and 100 µm, the incremented thicknesses are reported in the top row for En1 and in the head column for En2.

En2 \ En1	10 μm	20 μm	25 μm	50 μm	100 μm
10 μm	10-10	20-10	25-10	50-10	100-10
20 μm	10-20	20-20	25-20	50-20	100-20
25 μm	10-25	20-25	25-25	50-25	100-25
50 μm	10-50	20-50	25-50	50-50	100-50
100 μm	10-100	20-100	25-100	50-100	100-100

*Note: thicknesses in current matching [80nm 1.1 μm 2.5μm]

Figure 4.48: Space matrix: examined thicknesses combinations for ETFE coatings.

Hence, the multi-junction reflectance has been analysed for each thickness set of the space matrix. Figure 4.49 plots this optical quantity for some of the overall simulations. The optical modelling has pointed out that the space matrix is symmetrical about the main yellow diagonal. For instance, the reflectance for the combination En1 equal to 10 µm and En2 equal to 20 µm provides the same outcome if the combination results to be 20 µm En1 and 10 µm En2. Furthermore, any other homogeneous or heterogeneous thicknesses configuration compared to 25 µm-25 µm for ETFE coatings have provided minor and negligible variations. This latter homogeneous configuration has been selected as the optimal one.

The relative reflectance has been shown in a full red line and overlapped with the other heterogeneous simulations. The reflectance trend is the same among the depicted cases, except for small alterations. Only 10% of the incoming light is reflected back outside the solar device when wavelengths are below 800 nm. Whereas the light is reflected more considerably above 800 nm at the front side, the highest reflectance is about 30% in the range between 1000 nm and 1200 nm.

On final remark, these results have been presented for I thicknesses combination in current matching condition, however the same analysis has been carried out for the other two examined cases which have exhibited the same behaviours. Therefore, the respective graphs of those simulations have not been included to avoid repetitive findings, since the purpose of this section has been based on a comprehensive validation of ARC optical properties.

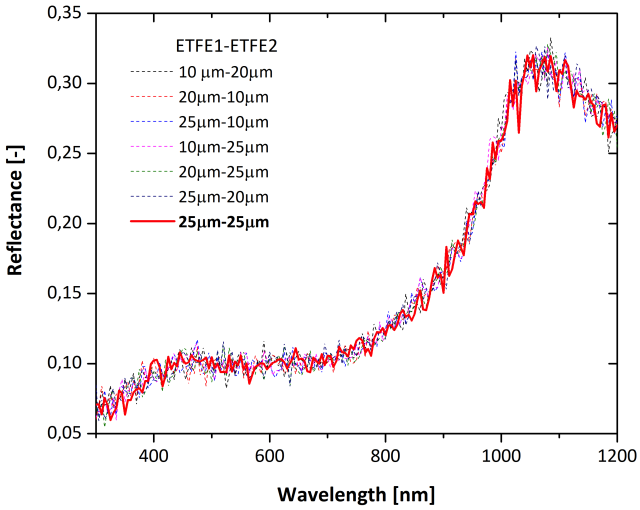

Figure 4.49: Total R at front side for different ETFE combinations.

4.9. Front reflector

The study has been focused on advantages and drawbacks of FTO for a better understanding of optical losses at the front side. Several potential alternatives have been provided for the transparent conductive oxide design.

As already mentioned in Section 3.1 (Chapter 3), in the thin-film solar cell technology the transparent conductive oxide plays a key role for the solar cell design and performance due to its optical and electrical properties. In Section 4.6, the transparent conductive oxide materials have been investigated at the rear reflector, while here the attention has been paid on TCO at the front reflector. In GENPRO4 solar cell architecture (Appendix A), the front contact has been modelled as 700 nm FTO layers and with additional 80 nm AZO coating, this latter belongs to the second interface of the designed solar cell together with the p-doped nc-SiOx coating of the top p-i-n junction. Both front and back reflectors have to meet two important requirements: low sheet resistance for high conductivity of free charge carriers and high transparency among all the solar spectrum. The transmitted light may be absorbed in the a-Si top sub-cell between 400 nm and 800 nm and in the middle and bottom nc-Si sub-cells up to 1100 nm. It should be noted that TCO features have to be combined with good light management to achieve optimal light scattering and trapping in the semiconductor junctions.

4.9.1. FTO, AZO, ITO, IOH comparison

This section focuses on several available transparent conductive oxide materials which may offer different optical enhancements for the triple-junction modelling. The developed TCO alloys at the front contact of the solar device are Fluorine-doped Tin Oxide (FTO), Indium Tin Oxide (ITO), Aluminium-doped Zinc Oxide (AZO) and Hydrogen-doped Indium Oxide (IOH).

In the interest of light management, it is therefore important to investigate how the incident light at the front solar cell side is optimised in terms of active layers absorption. As further the light travels through the absorptive materials, its intensity decreases with an exponential behaviour explained by the Lambert–Beer law [7]:

$$I(d) = I_o \cdot e^{-\alpha d}, \tag{4.12}$$

where I is the light intensity as a function of its path length d, α is the absorption coefficient and I_0 is ingoing light intensity. This equation implies that the total amount of light absorbed $I^{abs}(d)$

in a material is given by the difference between I_0 and the transmitted light through the absorber medium [7]:

$$I^{abs}(d) = I_o[1 - e^{-\alpha d}]. \tag{4.13}$$

Instead of photo-current intensity, the following analysis has been done in terms of photo-current density by dividing I_{ph} (mA) into the unit area (cm^2). Initially, the thickness of FTO layer has been varied between 100 nm and 1 µm by an increment of 100nm per time. As expected by Lambert–Beer law and illustrated in Figure 4.50, an increase of FTO thickness results in lower transmission to the active absorber layers and more $J_{ph,FTO}$. Thus, the FTO photo-generation increases when its thickness raises accordingly, whereas J_{ph} decreases in active layers with the t_{FTO} increase.

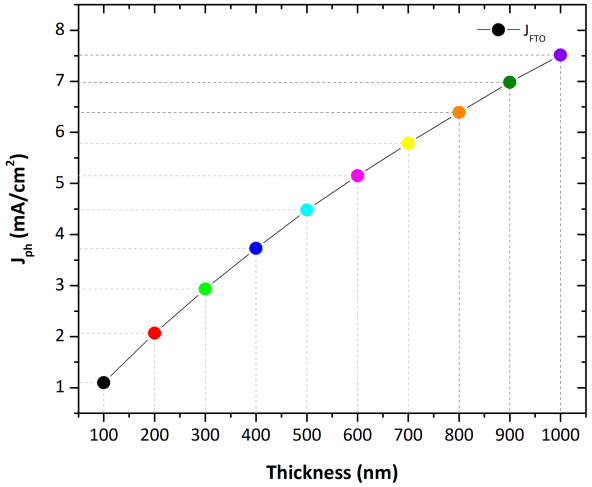

Figure 4.50: J_{ph} of FTO as a function of FTO thickness increase.

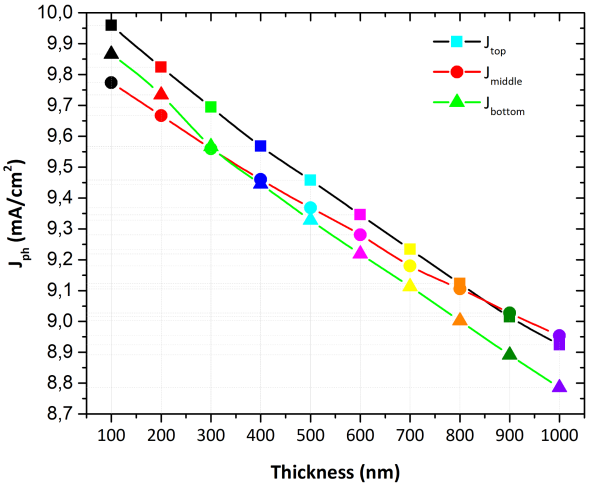

Figure 4.51: Active layers J_{ph} as a function of FTO thickness increase.

This behaviour has been presented in Figure 4.51 for the absorptive layers of the three sub-cells. The FTO thicknesses are represented on the x-axis, the J_{ph} values connected by a black line refer to the top sub-cell, whereas the red line connects the $J_{ph,middle}$ values and the green line links the $J_{ph,bottom}$ results. According to Equation 4.9.1, a thicker FTO layer generates more J_{ph}, and therefore less light is transmitted to the active a-Si/nc-Si/nc-Si layers, resulting in less photo-generation. The highest J_{ph} values in active layers occurs at the thinnest FTO (100 nm), whereas a thicker FTO implies a progressive J_{ph} decrease. In the graph there are two fundamental crossing points, the first is found where the FTO is 300 nm thick. Before this value the middle sub-cell limits the current in the solar device. Conversely, above 300 nm, the bottom sub-cell behaves as the limiting current semiconductor. The a-Si sub-cell has never limited the photo-generated current density. However, when the second intersection occurs at 800 nm, the range of short wavelength appears to be more absorbed by the front reflector and hence, the top sub-cell is no longer the most absorptive material.

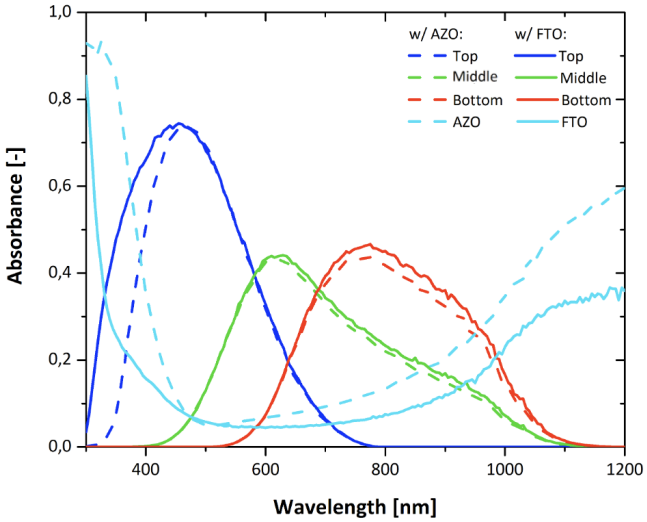

Figure 4.52: Active layer and TCO absorptance with FTO or AZO as front reflector.

In Figure 4.52, the triple-junction structure has been simulated in two different front reflector configurations: the full lines correspond to a stack of 700 nm of FTO and 80 nm of AZO, whereas the dashed curves include exclusively 700 nm of AZO. The absorptance plot points out that the front reflector arrangement provides better optical properties than the second one. The enhancement is more visible near the ultra violet region and near the infra-red range of solar spectrum, where the top and bottom sub-cells perform respectively. However, a front reflector configuration with only a thick Al-doped zinc oxide material turns out to be more absorptive and less transmissive.

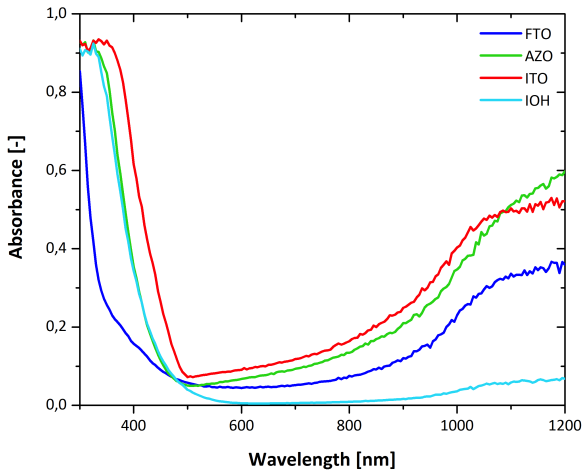

Figure 4.53: FTO, AZO, ITO and IOH absorptance.

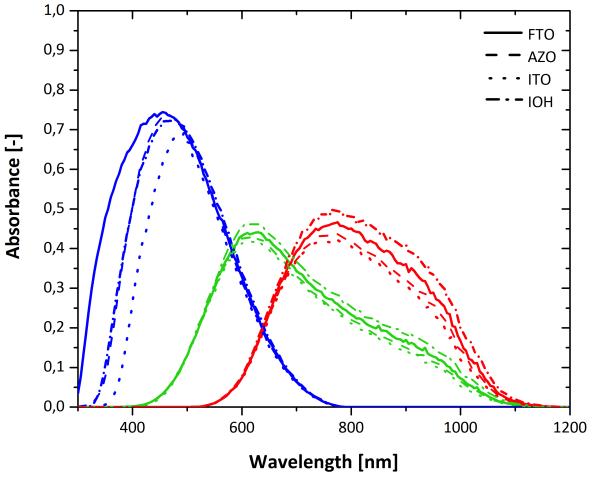

Figure 4.54: Active layers absorptance among different TCO materials for the front reflector.

Furthermore, the analysis has been widened among several transparent conductive oxide materials, which have been compared by analysing their absorption response in the solar spectrum range (Figure 4.53). Except for the green curve that represents a singular AZO layer of 700 nm, the other results have been simulated with 700 nm of the TCO material as referred in the legend plus 80 nm of AZO. All the materials share high transparency and high conductivity in the range from 475 nm up to 600 nm, this latter corresponds to the peak power of solar irradiance curve. AZO and ITO configurations are less suitable to be included as front reflector in the triple-junction design, because they result to be more absorptive than the other TCO materials in the whole light spectrum.

The simulations with FTO or IOH have provided better optical results. In general, FTO preserves its transparency and high conductivity at short wavelength, whereas at long wavelength it becomes be more absorptive material. Hence, its optical end electrical properties are less effective for the front contact purposes. However, IOH results to be a competitive front contact material, because it has higher transparency in the near infrared region compared to FTO. It appears to be a promising transparent conductive oxide material for multi-junction development.

Moreover, Figure 4.54 plots the same absorptance analysis for active layers. A front reflector with FTO performs better in the blue region by increasing the absorbed light in the top sub-cell, whereas IOH seems to be more adequate for an absorption enhancement in the bottom sub-cell at long wavelength.

Table 4.14 provides the absorptance percentage variation among different TCO configurations relative to FTO absorptance. Taking into account all n data points generated by GENPRO4 for each absorptance simulation, the absorptance percentage variation has been calculated as:

$$\Delta abp_{TCO}(\%) = \frac{\sum_{i=1}^{n} abp_{i,TCO} - abp_{i,FTO}}{n} \cdot 100. \tag{4.14}$$

Here, only a front reflector with IOH is less absorptive than FTO at wavelength longer than 475 nm. Additionally, the photo-current density among active layers is better distributed compared to FTO, even though $J_{ph,top}$ decreases by 4.3 %, J_{ph} of middle and bottom sub-cells gains about 6.7 % and 9.4 % respectively.

Absorptance variation from FTO configuration	
TCO material	Δ *abp (%)*
AZO	+12.01
ITO	+16.61
IOH (overall)	-4.94
IOH (λ<475 nm)	+24.12
IOH (λ>475 nm)	-12.16

Table 4.14: Absorptance variation (%) among different TCO materials compared to FTO.

4.9.2. Optical modelling of hybrid TCO

The FTO material is currently used as front reflector for the fabrication of solar cells with R2R technology at HyET company. However, it may be substituted or combined with other transparent conductive oxide materials to enhance the optical and electrical properties.

The first investigated configuration has a front reflector stack made with 100 nm FTO, 600 nm IOH and an additional coated interface with 80 nm of AZO. This has been compared with the cases of 700 nm FTO and 700 nm IOH. The graphs below illustrate the differences among the three studied front reflectors. Figure 4.55 compares their absorptance property, whereas Figure 4.56 shows the total reflectance at front side of the triple-junction. A front reflector with 100 nm FTO and 600 nm IOH follows 700 nm IOH absorptance behaviour throughout the wavelength range. The graphs underline a front reflector is more absorptive with 700 nm of FTO above 475 nm. In the same wavelength range, the light absorption always remains below 10% with 700 nm of IOH or with 100 nm of FTO and 600 nm of IOH. However, in these two latter cases, the reflectance at the front side increases up to 45 % at long wavelength. In the same range, R with 700 nm FTO is decreased by 10%, because it becomes more absorptive material.

Furthermore, these three configurations have also been analysed thorough the TCO photogenerated current density. If the front reflector is made by 700 nm FTO, J_{ph} is 5.79 mA/cm^2, whereas

$J_{ph,TCO}$ is 2.36 mA/cm^2 with 700 nm IOH and about 1mA/cm^2 more for 100 nm FTO and 600 nm IOH.

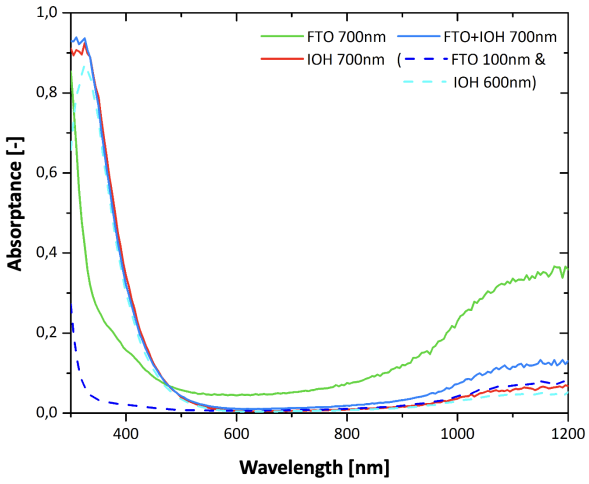

Figure 4.55: Among different TCO materials as front reflector.

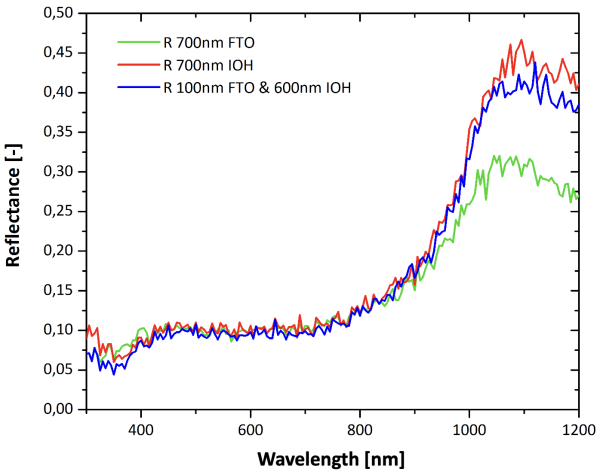

Figure 4.56: R among different TCO materials as front reflector.

The second front reflector configuration has been built with a series of 50 nm FTO at the top, 50 nm as intermediate layer IOH and 600 nm ZnO at the bottom. This attempt has been made to optimise the total reflectance at the front side, keep J_{ph} of TCO layering as lower as possible and hence, minimise the parasitic absorption.

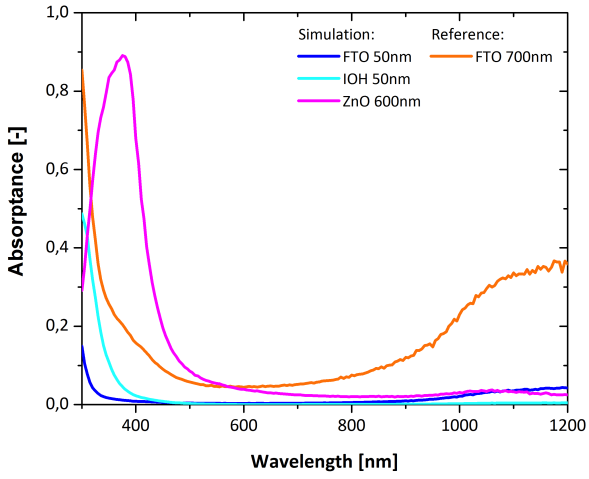

Figure 4.57: R of FTO IOH ZnO

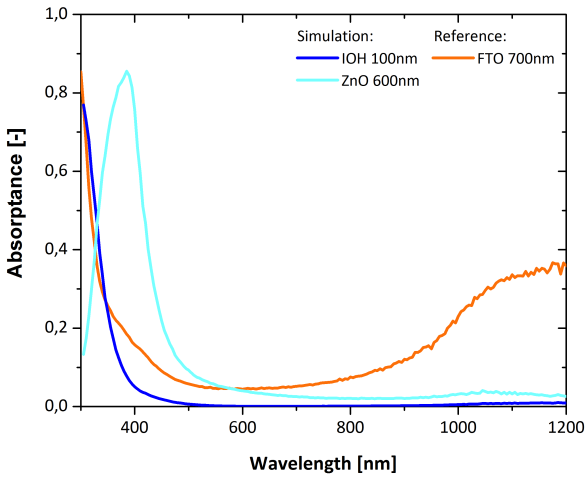

Figure 4.58: R of IOH ZnO

What Figure 4.57 underlines is that FTO and IOH 50 nm thin layers reach a high level of transparency. The conductivity property is mainly achieved through the inclusion of thick ZnO material. This configuration is optimised with wavelength above 600 nm, light at short wavelength is likewise absorbed by zinc oxide layer and not transmitted to sub-cells. Hence, an alternative solution has been provided in Figure 4.58 with a stack of two layers: IOH (100 nm) and ZnO (600 nm). The behaviours between the previous simulation and this one have a similar absorptance, but the latter optimises J_{ph} of front reflector. In conclusion, using a front reflector with 700 nm FTO brings to J_{ph} loss of 5.79 mA/cm^2, whereas J_{ph} results to be equal to 3.87 mA/cm^2 with 100 nm IOH and 600 nm ZnO and the series of three TCO layers supplies a value of 4.50 mA/cm^2, and therefore IOH results to be a promising alternative for baseline front reflector configuration.

5

Thin-film fabrication

This Chapter provides the experimental side of the triple-junction solar cell development that has been led in parallel with the modelling of triple-junction optical features. The first Section 5.1 has dealt with the fabrication of triple-junction films deposited on aluminium foil and the results of the first two deposition series attempted have been shown. The second Section 5.2 has investigated a different field of thin-film technology due to its potential route towards the inclusion of alternative low bandgap energy material from the IV group for multi-junctions solar cells.

5.1. Silicon based triple-junction solar cell on Al foil

This section presents the fabrication steps for the development of triple-junction samples held partially at Else Kooi Lab at TU Delft and HyET Solar company. The first outcomes regard a deposition series with mismatched currents among a-Si:H/nc-Si:H/nc-Si:H active layers, whereas in the second series presented, the thickness of top-middle-bottom sub-cells are 80 nm - 1.1 µm - 2.5 µm respectively. This combination is the result of the current matching findings widely discussed through the optical modelling developed in Chapter 4.

5.1.1. Temporary Al foil

All the sample depositions have been done on lab scale by using squared aluminium foils (10 cm x 10 cm). Initially, Factory Baseline texturing has been used for the fabrication of solar cells. However, Flamingo PV project has dedicated a part of its research to the development of a new performing texturing, also known as FLAM01 texturing on a temporary Al foil. The size features of both texturing have been mentioned in Section 4.3 (Chapter 4).

According to research developed by D.Rajagopal, Figure 5.1a and Figure 5.1b compare the surface morphology of two Al foils textured with Factory Baseline and FLAM01 respectively. What has mainly changed is the appearance of crater diameter. The dimension features of craters with FLAM01 are larger than those with Factory Baseline, hence the first texturing improves the scattering effect at the interfaces. Furthermore, FLAM01 may be distinguished for an enhancement in reflectance haze (76%) and also AID curve, which is wider than Factory Baseline [23].

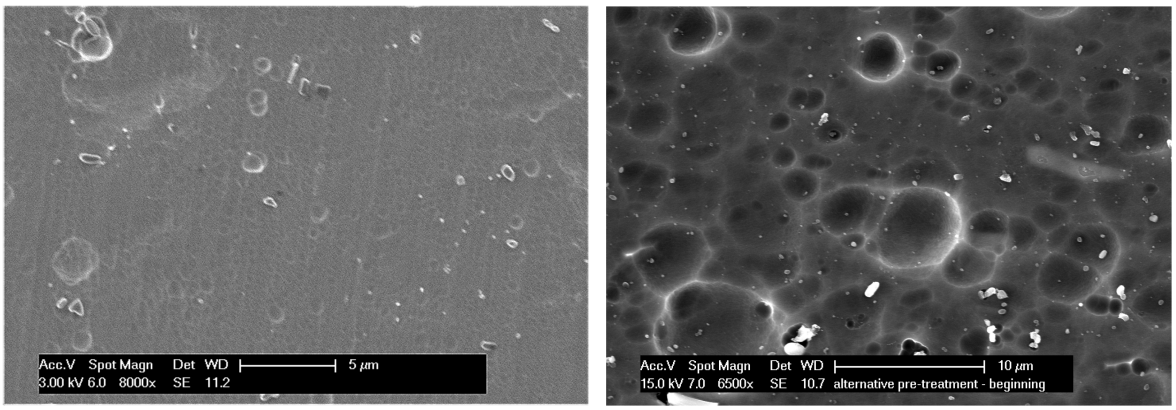

(a) Factory Baseline texturing (b) FLAM01 texturing

Figure 5.1: Surface imagines of two different textured Al foils used on an industrial scale. Retrieved by [23].

Regarding FLAM01 texturing, the Al foil has a starting thickness of 110 µm and, whereas the thickness results to be equal to 95 µm at the end of chemical etching process that textures the Al surface. However, the R2R method has to deal with several issues that do not allow achieving an excellent texturing. Hence, HyET company is moving towards the development of new texturing with thicker initial Al samples and this takes the name of FLAM02.

5.1.2. FTO deposition

The second step of the fabrication concerns the FTO deposition on Al foil through the atmospheric pressure chemical vapour method. This process is done at HyET, resulting from an accurate optimisation of several parameters such as deposition rate, thickness or temperature ordinarily at 500°C. The FTO thickness has been set at 700 nm for both texturing. According to Subsection 4.9.1 and Subsection 4.9.2, alternative configurations of transparent conductive oxide materials may achieve higher-performing front reflector in terms of optical and electrical properties, but these have not been processed yet.

5.1.3. Si-based *p-i-n* junctions deposition

The silicon p-i-n junctions of the triple-junction samples have been deposited through PECVD technique, this method has been explained in Section 3.6 (Chapter 3). Before the placement of samples in the load lock, the textured Al foils with pre-deposited FTO need to be cleaned. The cleaning procedure requires an ultrasonic bath in acetone solution and then in isopropyl alcohol (IPA). When samples are perfectly dried, they can be mounted on the metal holder and loaded in Amigo equipment.

It is equipped with six deposition chambers (DPC from 1 to 6), where each of them is characterised by specific functionalities based on the available precursor gas flows. B_2H_6 is the precursor gas in DPC1, whereas DPC2 is connected with PH_3 inlets. DPC1 and DPC2 are suitable for the deposition of p-doped and n-doped silicon layers respectively. The intrinsic layers are deposited in DPC3 for a-Si:H and in DPC4 for nc-Si:H. Moreover, the silicon oxide layers are deposited through inflows of carbon dioxide.

The first process involves the AZO sputtering in DPC6, this chamber is generally pre-heated for 1800 seconds. During the deposition, the applied radio frequency (RF) and temperature are 13.56 MHz and 300°C respectively.

Subsequently, the p-i-n junctions are deposited using RF for amorphous top cell and a very high frequency (VHF) of 40.68 MHz for middle and bottom cells. The layers growth occurs by the use of stable plasma that is confined between two electrodes in each chamber. The electrodes dimensions

are 12 cm x 12 cm. The upper electrode hosts the substrate, whereas the lower electrode is pierced, allowing the precursor gas to inflow homogeneously in the chamber. Table 5.1 summarises the main parameters used for the samples deposition in AMIGO equipment, however they are standard values that might have been altered according to different requirements of triple-junction depositions.

Layer	*Power [W]*	*Pressure [mbar]*	*T [°C]*	*Gas*	*Flow rate [sccm]*
AZO	300	2.6	300	Ar	20
µc-SiOx(p)	12	2.2	300	SiH_4 B_2H_6* CO_2 H_2	0.8 20 2.3 170
a-Si:H (i)	2.8	0.7	300	SiH_4 H_2	40 0
µc-SiOx(n)	11	1.6	300	SiH_4 PH_3** CO_2 H_2	1 1.2 2 100
µc-SiOx(p)	12	2.2	300	SiH_4 B_2H_6* CO_2 H_2	0.8 10 1.6 170
µc-Si:H (i)	40	4	180	SiH_4 H_2	3.5 120
µc-SiOx(n)	11	1.5	300	SiH_4 PH_3* CO_2 H_2	1.0 1.2 1.6 100
µc-SiOx(p)	12	2.2	300	SiH_4 B_2H_6* CO_2 H_2	0.8 10 1.6 170
µc-Si:H (i)	40	4	180	SiH_4 H_2	3.5 120
µc-SiOx(n)	11	1.5	300	SiH_4 PH_3* CO_2 H_2	1.0 1.2 1.6 100

Table 5.1: Parameters for the triple-junction depositions in AMIGO equipment, where B2H6** = B2H6/H2n(200ppm), PH3** = PH3/H2.

5.1.4. Back reflector deposition

The back reflector is made of two layers: AZO with a thickness of 80 nm and 300 nm of Al film. Firstly, a mask is attached to the sample that allows defining twenty solar cell active areas, which are the only ones subject to back reflector deposition. AZO and Al layers are deposited via the magnetron sputtering method, its working principle is based on the combination of electric and magnetic fields that are perpendicular to each other in order to confine the electrons within the electrode surface. This physical vapour deposition technique requires a refined tuning of parameters, because ions may bombard the layers enough heavily to damage the sample [59]. The deposition of AZO layers occurs through RF at a power of 407 W with an argon flow rate of 40 sccm, whereas the DC sputtering is responsible for Al layer deposition with an argon flow rate of 19 sccm.

A refined tuning of deposition parameters is fundamental for the growth of AZO/Al layers and the performance of the back reflector. As explained in Section 4.6 (Chapter 4), a high-quality back reflector ensures electrical and optical properties. Therefore, it has to provide the highest back reflection, the lowest transmission at the rear side and the highest conductivity for the charge carriers collection.

5.1.5. Copper contacts and Lamination

Below the Al film, the copper contacts are attached to the samples, each solar cell has a small squared extension suitable to tape the copper strip. Afterwards, the triple-junction sample is laminated by gluing a permanent carrier foil. This carrier material is polyethylene naphthalate with a thickness of 1.5 µm. The overall triple-junction thickness reaches about 240 µm at the end of the lamination process. This material provides a good trade-off between flexibility and rigidity and acts as an encapsulant at the back side. It is also functional for the next step where the temporary Al foil is progressively etched away. The etching process puts the sample under stress, the mechanical tension generated at the front side is transferred across the solar cell and then supported by the carrier foil avoiding any possible damage. Figure 5.2 shows the active areas and the copper contact at the back side of the sample after etching, each active area is 72 mm^2.

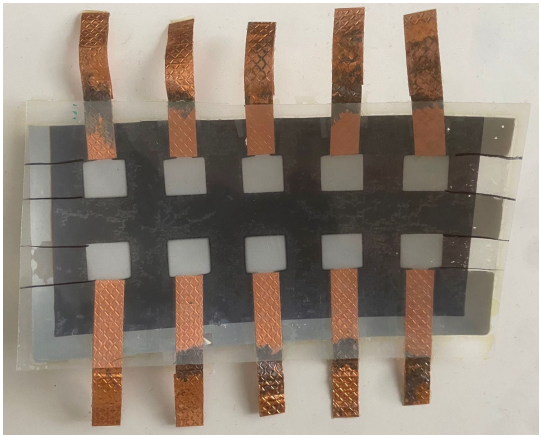

Figure 5.2: Back side of a triple-junction sample.

5.1.6. Al etching

When the triple-junction is on permanent carrier foil, the temporary Al foil can be etched away in two steps. The whole Al foil is reduced to a thickness of 20 µm through the use of NaOH 1.2M at 70°C. Then, the triple-junction is cleaned with 0.1M H_3PO_4 and water at 60°C. The sample subsequently is annealed, this process avoids the presence of cracks and other defects that might be caused by the mechanical stress when the Al foil is thinned. In the second etching step, three regions of front side are taped, and this results in two uncovered bands, which are in correspondence with the active

areas at the back side. Here, the aluminium is completely etched away, the left Al stripes act as bus bars. In Figure 5.3, it is possible to distinguish the bus bar connections in grey colour and the complete etched Al bands where active areas are located. Figure 5.4 is a schematic frontal view of the triple-junction structure after the etching process. The repetition includes the electrical contacts, the bus bars and the carrier foil.

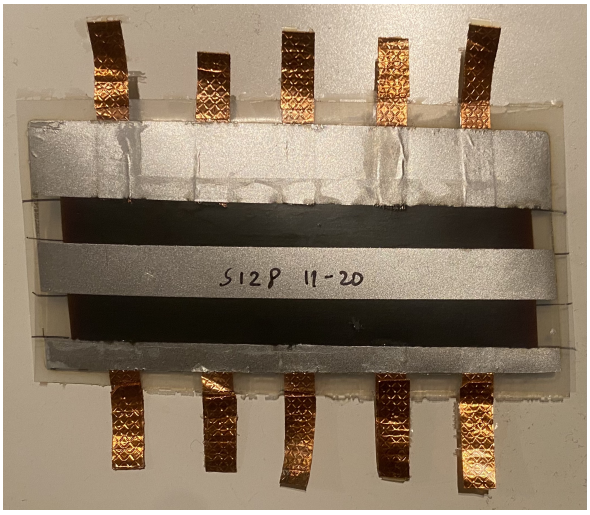

Figure 5.3: Front side of a triple-junction sample.

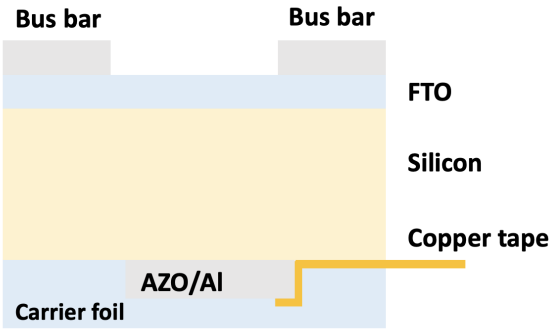

Figure 5.4: Frontal sketch of the triple-junction after the etching process.

5.1.7. Encapsulation

The following step regards the encapsulation at the front side with the use of a 4 layers stack: first ETFE layer of 25 µm, 90 µm of glue, second ETFE layer of 25 µm and 90 µm of glue. The tetrafluoroethylene protects the solar device from environmental agents and also enhances its performance. According to historical data of HyET modules [50], the total spectral utilisation is improved by 5% when the encapsulant is embedded in the architecture of solar cell. A wider discussion about the encapsulation can be found in Section 4.8 (Chapter 4), where its optical properties have been simulated for the triple-junction solar cell.

5.1.8. Outcomes of the first series

In the first series of triple-junction samples, the top-middle-bottom sub-cells thicknesses have been set at 200 nm, 1 µm and 2 µm respectively. The selected thicknesses do not meet any current matching requirement. The goal of this series was to inspect the presence of cracks and defects among layers and verify the deposition quality. The processed samples have been textured with FLAM01 and analysed without including the encapsulant and the lamination.

Figure 5.5 represents two cross-sections of the triple junction structure through the use of scanning electron microscopy (SEM) tool. On the left, Figure 5.5a delineates the location of sub-cells and FTO material, this latter is characterised by textured surface and brightness. The SEM cross-section has pointed out the presence of a few cracks with such thicknesses. The micro-crystalline Si-based materials have a complex atomic structure. In such materials several grains with a crystalline lattice can be found and these are incorporated in a tissue of hydrogenated amorphous silicon. Therefore, the best achievable nc-Si:H material should have an amorphous-microcrystalline transition phase where the crystalline lattice occupies 60% of the space. Having solar cells with mixed-phase layers such nc-Si:H causes cracks and vacancies. In general, these issues may be prevented by limiting the bottom sub-cell thickness.

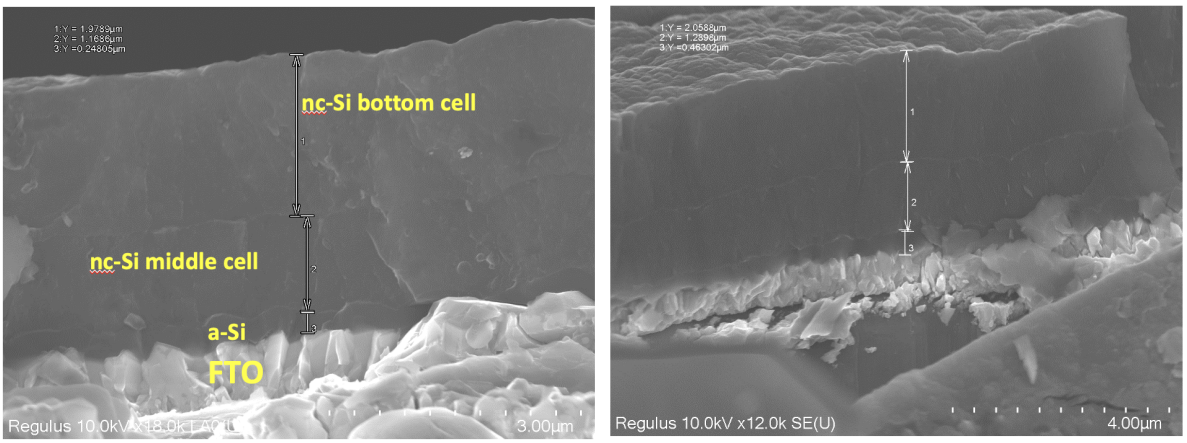

(a) I inspection (b) II inspection

Figure 5.5: SEM cross-section of a triple-junction sample.

Furthermore, these inspections have allowed estimating if the average thicknesses were in line with the selected thicknesses for the AMIGO deposition. In Table 5.2, it can be seen the thickness of each layer has been deposited homogeneously, even though the bottom layer shows considerable thickness variations.

Measurements	*a-Si:H top sub-cell [µm]*	*nc-Si:H middle sub-cell [µm]*	*nc-Si:H bottom sub-cell [µm]*
I	0.248	1.169	1.979
II	0.193	1.111	1.905
III	0.266	1.151	1.413
IV	0.357	1.164	1.872
V	0.322	1.245	1.970
average	0.277	1.168	1.828
standard deviation (%)	6.41	4.87	23.60

Table 5.2: Average and standard deviation of sub-cells thicknesses among five measurements with SEM microscopy.

Additionally, the J-V curve in darkness and the parallel resistance to be associated with shunts have been evaluated. The shunt resistance (R_p) values and J-V curves have been measured by using the following diode structure: Al foil/TCO/AZO/triple junction/AZO/Al. On this sample, each diode has size features of 4x4 mm and the whole diodes are deposited on a grid where 14 diodes are located per line for a total of 196 diodes. It shall be noted that not all the measurements have provided significant results, some measurements are not reliable due to damaged probes in the used test tool.

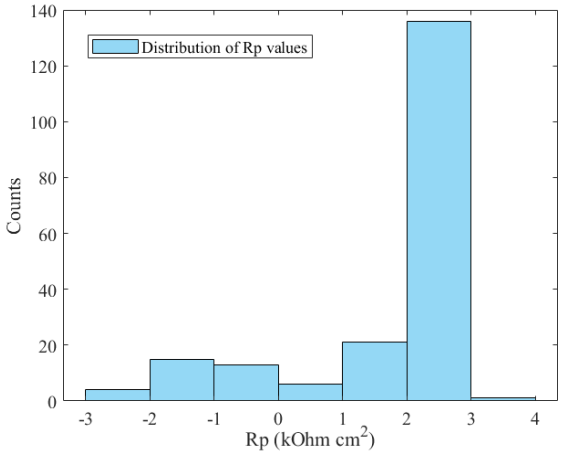

Figure 5.6: Rp distribution among 196 measured diodes.

Figure 5.6 represents the distribution of parallel resistance values on a logarithmic scale. Few outcomes are lower than 1 kΩ cm ^{2}, whereas the majority of values are higher than 100 kΩ cm ^{2} (the tallest column in the histogram). Hence, diodes are performing well and no leakage of current is expected through an alternative and undesired path in the structure.

Figure 5.7 plots the J-V curve of one of the best well-working diodes, here the small graph shows the exponential curve with a sharp knee near 1.4~1.5 V. For a better understanding, the linear graph of J-V has been plotted through a logarithmic plot. It can be noted that the dark current-density is always lower than 10^{-2} mA/cm^2 when the voltage range is between -2 V and 1 V and it reaches values lower than 10^{-4} mA/cm^2 near 0 V. When voltage is higher than 1 V, there is a steep increase of dark photo-current density up to 10 mA/cm^2.

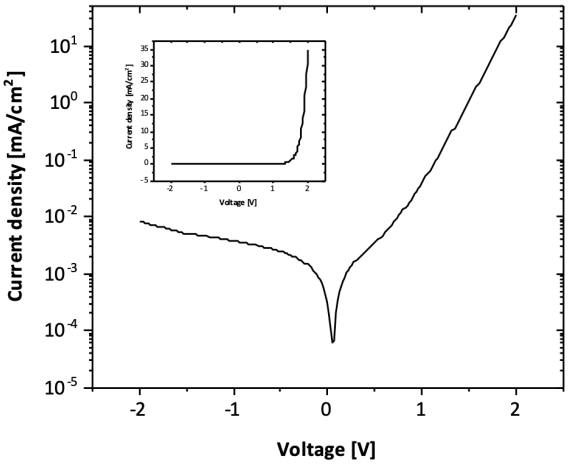

Figure 5.7: J-V curve of one of 198 diodes with very high Rp resistance.

On another sample, the active areas of solar cells have been deposited, including the lamination at rear side and the etching of temporary Al foil. As mentioned in Subsection 5.1.4, the sputtering of AZO and Al layers at the back contact is made through a mask that overlaps the sample and this mask is sketched in Figure 5.8 where 4 columns of active regions are located: from C1 to C5 and from C11 to C15 the active area is 0.81 cm^2 per each cell, while it is 0.36 cm^2 from C6 to C10 and from C16 to C20.

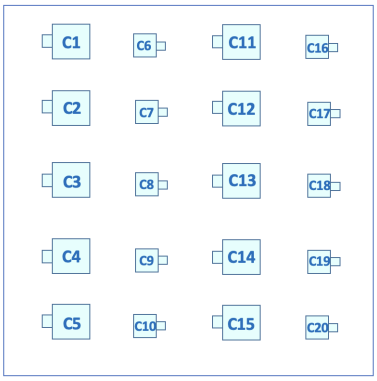

Figure 5.8: Mask used for AZO and Al layers in the first triple-junction deposition series.

If the equivalent electrical circuit of a solar cell (Figure 2.9, Chapter 2) is taken into account, the open circuit voltage is found when the solar cell is illuminated and the circuital terminals are not connected. Hence, the solar cell only generates voltage. In the J-V plot, this condition is found when the curve intersects the V-axis. The V_{oc} is expressed by the equation [7]:

$$V_{\mathrm{oc}} = \frac{k_B T}{q} \ln\left(\frac{J_{\mathrm{ph}}}{J_0} + 1\right) \approx \frac{k_B T}{q} \ln\left(\frac{J_{\mathrm{ph}}}{J_0}\right), \tag{5.1}$$

the approximation is possible when the photo-current density J_{ph} is considerably greater than the saturation current J_0, this latter measured in darkness. V_{oc} provides information about the bandgap of active layers, the doping amount in doped layers and the recombination effect in the solar cell. On the other hand, J_{sc} represents the condition when the solar device only delivers current and no voltage (J-axis intersection in J-V plot). It is the maximum deliverable current by the solar cell and depends strongly on optical features such as absorption in active layers or reflection. Therefore, J_{sc} may be altered by the spectrum and the intensity of incident light and it also depends on the probability that free charge carriers are collected at front/back contacts.

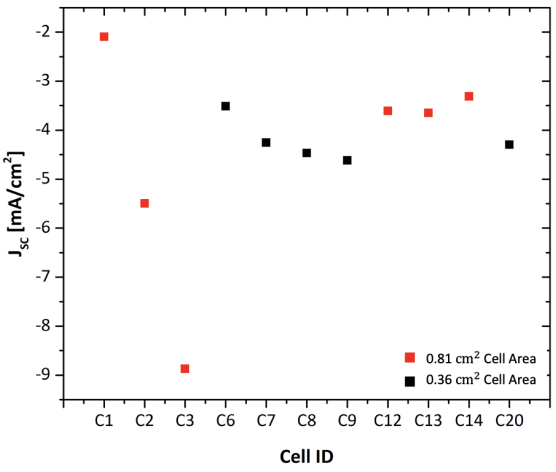

Figure 5.9: J_{sc} values (first triple-junction series).

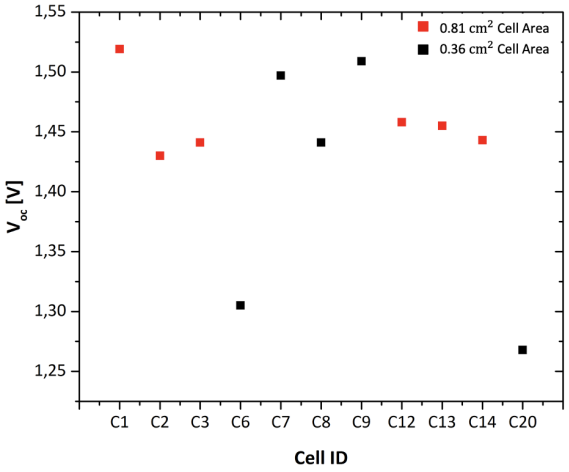

Figure 5.10: V_{oc} values (first triple-junction series).

Figure 5.9 plots the J_{sc} values and Figure 5.10 provides the V_{oc} measurements under illumination. Solar cells with an active area of 0.81 cm^2 provide an average J_{sc} and V_{oc} of 4.51 mA/cm^2 and 1.46 V respectively. When active area is 0.36 cm^2, J_{sc} and V_{oc} are 4.23 mA/cm^2 and 1.39 V on average.

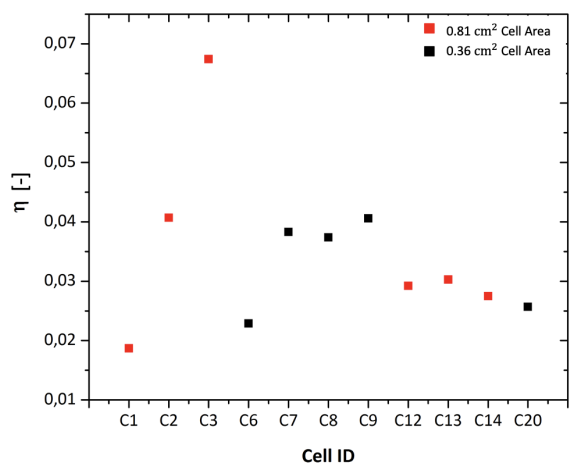

Figure 5.11: Efficiency η (first triple-junction series).

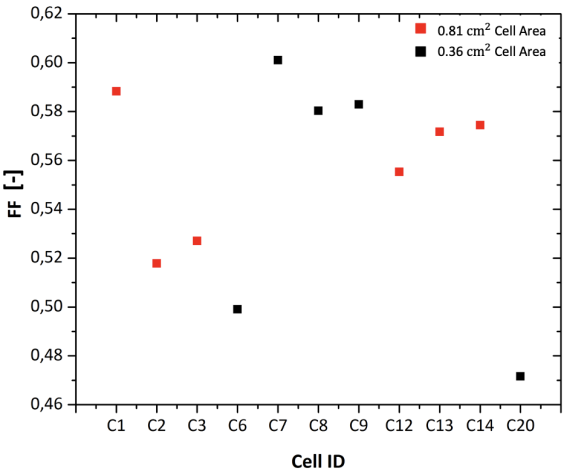

Figure 5.12: Fill factor FF (first triple-junction series).

The conversion efficiency η and the fill factor FF are depicted in Figure 5.11 and Figure 5.12 respectively, the formulas can be found in Section 2.7 (Chapter 2). When the active area corresponds to 0.81 cm^2, η is 0.034 and FF is 0.56 on average, whereas the active area of 0.36 cm^2 finds average values of 0.033 for efficiency and 0.55 for fill factor.

The last investigated parameter is the series resistance R_s that is expected to be as small as possible since the current that flows in is dissipated as thermal energy instead of being delivered by the solar cell. Looking at J-V plot of Figure 5.13, the R_s may be seen as the slope of the curve near the open circuit point, the parallel resistance R_p, also known as shunt resistance R_{sh}, is found near the short circuit operation. Figure 5.14 represents the measured series resistance. The solar cells with larger active areas have lower R_s the cells with smaller areas, 19.47 Ω m^2 for the former and 34.85 Ω m^2 for the latter on average.

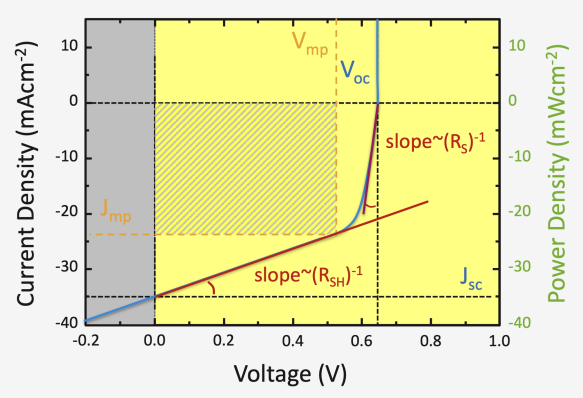

Figure 5.13: Derivation of R_s and R_{sh} from the slope of J-V curve.

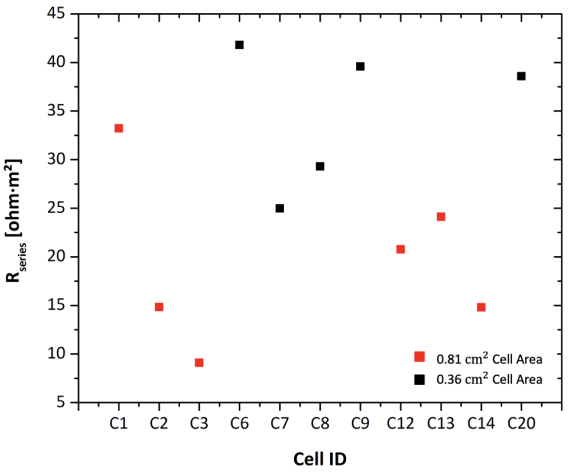

Figure 5.14: Series resistance R_s values (first triple-junction series).

Several cells could not have been measured because the back contact partly overlapped with the Al foil on the edge of the sample. Therefore, in the following series, the mask design for the back contact sputtering has been chanced and the active area has been optimised at 72 mm^2 per each solar cell. The new mask design has been represented in Figure 5.15. Further solar cells have been lost during the integration of copper tapes. For some cells, the Cu tape has been damaged

during the lamination, broken after removal from lamination or not properly protected with etch-resistant tape during the etching steps. Hence, during J-V measurements the missing solar cells were completely shunted without providing any reliable outcome.

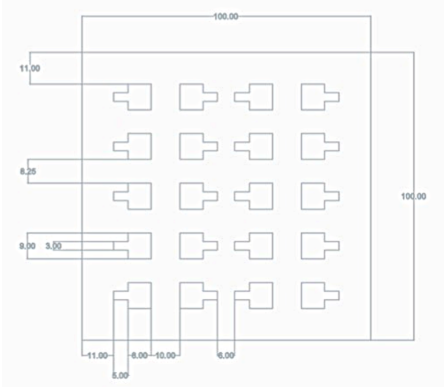

Figure 5.15: Design of the new mask, values in [mm^2].

5.1.9. Outcomes of the second series

The second series has been developed by using two different types of back contact. Except for one sample, the others have followed the sputtering procedure of 80 nm AZO layer and then 300 nm Al layer. The AZO has been sputtered with RF method by setting power at 407 W and pressure at 5.8 10^{-3} mbar, whereas the Al film has been deposited with the DC sputtering with higher power (1380 W) and lower pressure (1.8 10^{-3} mbar). Section 4.6 has addressed the importance of reflection at the back contact and how the implementation of a silver layer in the back reflector stack may enhance the optical properties of the triple-junction and then achieve a more efficient solar device. For this purpose, a sample has been processed with a back reflector made of 80 nm of Al-doped Zin Oxide, 400 nm of silver, an additional 80 nm of Al-doped Zin Oxide and 300 nm of Aluminum. The Ag layer has been deposited with DC sputtering and for this process 1400 W and 3.5 10^{-3} mbar have been applied for power and pressure settings respectively. The first type of back reflector is referred to as AZO/Al, the second type of back reflector is mentioned as ZAZAl.

The second batch has faced several issues during the fabrication, and therefore the vast majority of solar cells were shunted. It is important to consider that this manufacturing line is under development and requires several implementations, especially in the etching and lamination processes, which have shown various faults. These two aspects may be the explanations for the lack of results provided by the samples. Nevertheless, the following graphs have provided inconsistent values with the optimised optical modelling. The electrical modelling has been completely neglected and this has not allowed to simulate a real operation of triple-junction. It may also be possible that additional issues are related to the growth of nc-Si:H and a-Si:H materials during the PECVD process.

ZAZAl back contact				*AZO/Al back contact*			
J_{sc} [A/m^2]	V_{oc} [V]	FF [-]	R_{series} [$\Omega\ m^2$]	J_{sc} [A/m^2]	V_{oc} [V]	FF [-]	R_{series} [$\Omega\ m^2$]
60.16	1.30	0.44	6.93	45.61	2.03	0.59	31.67
60.28	1.50	0.44	4.31	21.29	1.95	0.61	65.69
59.89	1.43	0.47	4.75	22.40	1.53	0.45	149.40
63.99	1.35	0.35	5.11				
58.67	1.42	0.46	5.55				

Table 5.3: J_{sc}, V_{oc}, FF and R_s data collection with ZAZAl or AZO/Al as back contact.

Table 5.3 collects the outcomes of all operating solar cells in the second deposition series: five of them are with ZAZAl back contact and the other three cells with AZO/Al back contact. The graphs below offer a comparison between the two available back contact configurations. They provide the mean value and standard deviation of the short circuit current density in Figure 5.16, the voltage in open circuit condition in Figure 5.17 and the fill factor in Figure 5.18.

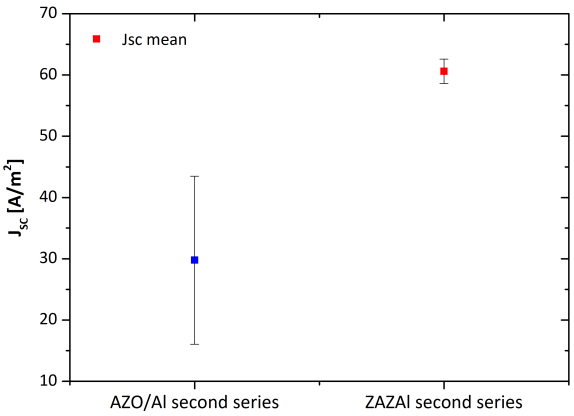

Figure 5.16: Short circuit current (second triple-junction series).

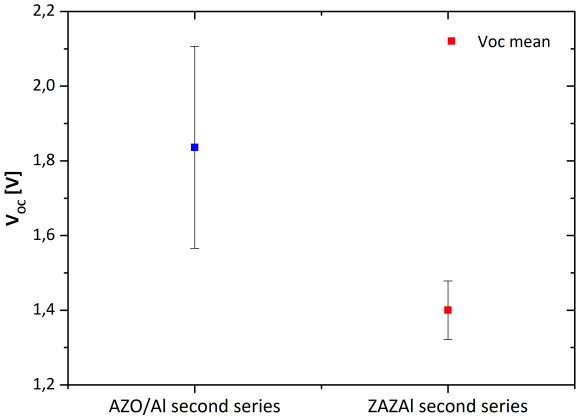

Figure 5.17: Open circuit voltage (second triple-junction series).

It can be observed that the series resistance is lower with ZAZAl as back contact compared to AZO/Al configuration. This has to do with the higher conductive property of Ag that Al material. Furthermore, a lower resistance at the back contact improves the short circuit current density, which is also dependent on the contact resistance. If Equation 2.7 (Chapter 2) is taken into account for the estimation of short circuit current, then higher R_s will result in lower J_{sc} and vice versa. Additionally, the resulting J_{sc} is also connected with the photo-generated current density: an increase of J_{ph} provides a J_{sc} improvement.

As discussed in the optical modelling developed in Section 4.6 (Chapter 4), J_{ph} may be enhanced by using a material such as silver that reflects more light back to the bottom sub-cell and hence, it boosts the light absorption in this active absorber layer. However, the J_{ph} enhancement is subject to the current matching condition, having mismatched currents among sub-cells decreases the photo-generated current and this is the case of ZAZAl as back contact, where the applied thicknesses are optimised only for a multi-junction structure with AZO/Al. The lower V_{oc} values in ZAZAl configuration than the one with AZO/Al may be justified by the fact the open-circuit voltage depends directly on the natural logarithm of J_{sc} and J_0 ratio. Hence, if J_{ph} is not optimised as in ZAZAl case, the measurements of V_{oc} are expected to be smaller as shown in Table 5.3.

Looking at open circuit values, it is also possible to recognise some solar cells have provided high value and more likely, this has to do with undesired deposition of amorphous material in middle/bottom sub-cells. a-Si:H has an open circuit voltage of 0.8 V, whereas nc-Si:H has a V_{oc} of 0.5 V. As a final remark, the given fill factor values differ from each other due to their close dependence with V_{oc} and J_{sc} as well as the maximum power-point.

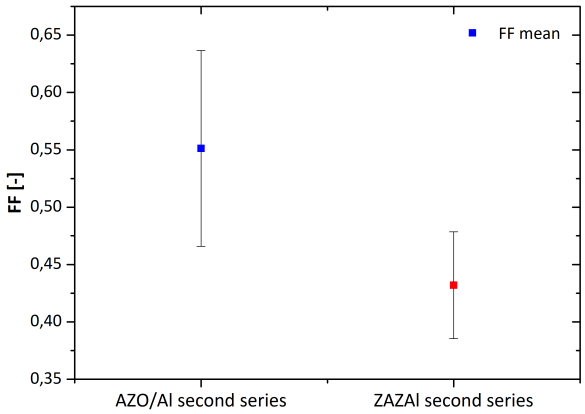

Figure 5.18: Fill factor (second triple-junction series).

5.2. Amorphous hydrogenated germanium-tin (a-GeSn:H) films

The research has looked into possible alloys from elements of IV group to yield low E_g and has refined the investigation into the germanium (Ge) and tin (Sn) elements. Except for their achievable low bandgap energy, Ge and Sn are earth-abundant materials and safe semiconductors. It is important to note that alloys with elements belonging to IV group generate a tetrahedral structure, which does not require other elements from other groups for the formation of neutral and intrinsic materials. Silicon, germane and tin elements have been already used in several studies for the growth of a lattice-matched direct bandgap [60], but this experimental path has been directed towards a-GeSn films processed via PECVD. Refer to Section 3.6 (Chapter 3) for the explanation of the plasma enhanced chemical vapour deposition technique.

This deposition method has been chosen due to the relatively cheap and fast processing of a-GeSn films and for the compatibility with the conventional processing methods applied for the processing of thin-film silicon solar cells, likewise in Section 5.1 for the triple-junction solar device on flexible Al substrate. Hence, the following analysis of a-GeSn:H has been based on the deposition process and material characterisation through vibrational and elemental spectroscopy of optical and electrical properties.

5.2.1. Deposition

The deposition of GeSn:H films has been carried out thanks to the use of tin as precursor gas for the growth of hydrogenated germanium material. Several precursors may be applied for the hydrogenated amorphous alloys deposition such as methane (CH_4), germane (GeH_4) or silane (SiH_4). If the SnH_4 is taken into account as a precursor, then it will result in a chemically unstable gas undesired for this research. However, an alternative Sn-precursor, known as TMT or tetra-methyltin ($Sn(CH_3)_4$) has been used for GeSn:H depositions. Table 5.4 summarises the standard parameters for nc-Ge:H and a-Ge:H samples.

Film	P_{RF} $(mW{\cdot}cm^{-2})$	p *(mbar)*	T_s *(°C)*	GeH_4 *(sccm)*	H_2 *(sccm)*
a-GeSn:H	14.9	4	210-290	2	200
nc-GeSn:H	24.8	1	210-290	1	200

Table 5.4: Deposition conditions for a-GeSn:H and nc-GeSn:H.

For each deposition series GeSn:H films have been deposited on two different substrates at the same time. The first substrate is 500 µm mono-crystalline silicon wafer, the other is Corning Ea-

gle XG glass (10 cm x 2.5 cm). Then, the depositions on wafer have been analysed through Fourier Transform Infrared (FTIR) spectroscopy, Raman spectroscopy (Raman), Energy Dispersive X-Ray Spectroscopy (EDX) and Scanning Electron Microscopy (SEM). The PECVD equipment is based on radio-frequency reactor, where germane, molecular hydrogen and TMT are been applied as precursor gasses. In addition, TMT is liquid at room temperature, thus it has always been pre-heated at 70 °C and for some series also diluted with helium He. The TMT inflow has been regulated by the duty of cycle δ, which is the fraction between the opening and closing time of TMT valve. Depending on the deposition, the open time has varied between 5 and 10 ms, while the close time is between 100 ms and 1 minute.

5.2.2. Outcomes & Remarks

The experimental investigation has been led among several parameters, such as activation energy (E_{act}), dark conductivity at room temperature σ_d, photo-conductivity σ_{ph}, the refractive index at a wavelength of 600nm ($n_{@600nm}$), film thickness and optical bandgap energy (E_{04}). The (E_{act}) is the difference between the Fermi energy level and the nearest band edge. For instance, in an intrinsic material the Fermi energy level has the same distance from the conduction and valence bands E_{act}=0.5E_G. A relation between σ_d and σ_{ph} is expressed by:

$$\sigma_{\mathrm{d}} = \sigma_0 \exp\left(\frac{-E_{\mathrm{act}}}{k_{\mathrm{B}} T}\right), \tag{5.2}$$

where the photo-conductivity has an exponential behaviour as function of E_{act}, temperature T and Boltzmann constant k_B. The E_{04} describes trends in the optical absorption of the films and is determined by calculating the photon energy at which the absorption coefficient equals 10^4 cm^{-1}.

Figure 5.19 represents an example of FTIR and Raman spectra used for elemental composition, which identify the relevant peaks of elements in the processed films. It has obtained by comparing the area of fitted Gaussian distributions after background subtraction. Here, FTIR allows determining the elemental fractions as the atomic fractions ($at._x$) instead of weight fractions, whereas Raman spectroscopy estimates the crystallinity (χ_c) [61]. Furthermore, absorbance peaks individuated through FTIR measurement has been used for the calculation of hydrogen atoms (N_H) bonded to germanium (Ge-H) and carbon (C-H).

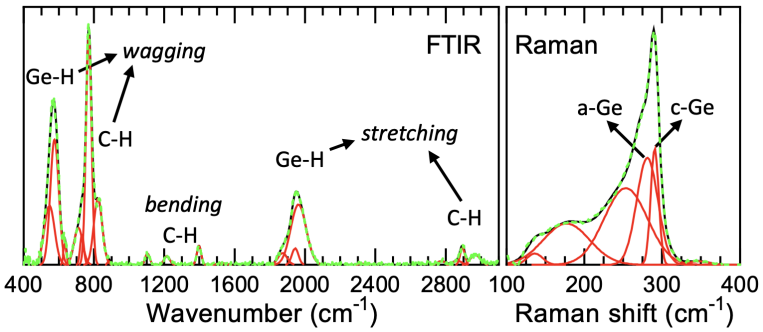

Figure 5.19: FTIR and Raman spectra of an nc-GeSn:H film.

The Ge-H and C-H vibrational modes are indicated in the left FTIR plot, while the amorphous and crystalline Ge vibrational modes are indicated in the Raman graph. The number of hydrogen atoms bonded to germanium (N_{H-Ge}) is determined by the wagging vibrational mode of Ge-H, located at around 560 cm^{-1} as depicted in FTIR plot. In this case, the strength of the wagging modes is proportional to the hydrogen concentration, whereas for the same purpose, the stretching modes

are used for C-H bonds. It should be noted that the wagging mode interests a change in the angle between the plane where Ge atom is located and the plane of H, while for example, the stretching mode changes the bond distance between C and H. Therefore, the ratio ($R_{CH/GeH}$) between the hydrogen atoms bonded to C and Ge is found as:

$$R_{\mathrm{CH/GeH}} = \frac{N_{\mathrm{H-C}}}{N_{\mathrm{H-C}} + N_{\mathrm{H-Ge}}}. \tag{5.3}$$

In this experimental research, several deposition series have been implemented, one series differs from the others according to TMT, temperature and power settings. The first bunch of experiments has interested the TMT injection. Initially, a-Ge:H has been deposited by decreasing progressively the duty cycle, especially when δ was lower than 1000. Figure 5.20 provides SEM results of a a-GeSn:H deposition through the same inspection at two different magnifications with 100 of duty cycle and no He gas flow. In particular, the left picture shows a nonuniform Sn distribution, where there is a diagonal Sn concentration on the examined sample and this can be associated with the TMT inflow direction. On the right, it can be observed clustering of Sn during the GeSn growth.

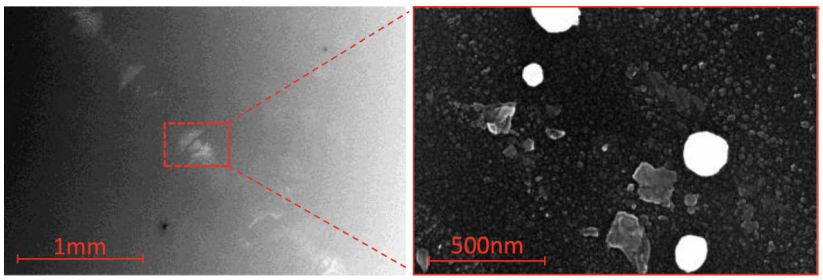

Figure 5.20: SEM images at 1 mm and 500 nm magnifications of a-GeSn:H surface, δ=100 and F_{He}=0 sccm.

In order to overcome the challenge related to the Sn clustering, TMT has been diluted with He and then inserted in the reactor chamber. Unfortunately, this attempt has not provided the expected result with δ equal to 100 and 20 sccm of F_{He} as can be seen in Figure 5.21 and more accurately in Figure 5.22.

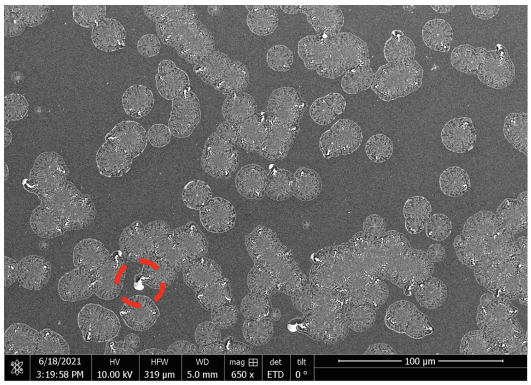

Figure 5.21: SEM image of a-GeSn:H samples with δ=100 and F_{He}=20 sccm.

Another challenge has been presented in Figure 5.21: the blue circle reveals a carbon concentration that exceeds that of Sn cluster. Having a high C concentration in reference to that of Sn impedes the deposition of chemically stable, intrinsic and low E_g Ge:H alloy.

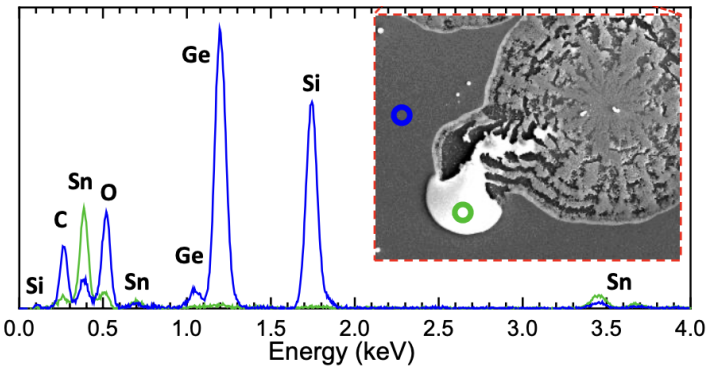

Figure 5.22: EDX spectra: Sn cluster (green) on the amorphous GeSn:H phase (blue).

Taking into account Figure 5.23, I graph shows how E_{04} raises with the increase of carbon concentration $at._C$, this also generates an increase of $at._O$ in the films, as plotted in IV graph. This outcome is justified by the fact that higher C-integration is expected when more CH_n groups are injected from the TMT precursor. Additionally, II graph as a function of $n_{@600nm}$ underlines the increase in $at._C$ also results in a more porous material. Moreover, some depositions with high Sn concentration are located in the region where E_{04} is lower than 1.1 eV. This is indicated in III graph where the presence of carbon does not forbid E_{04} decrease of unalloyed Ge:H films through Sn concentration.

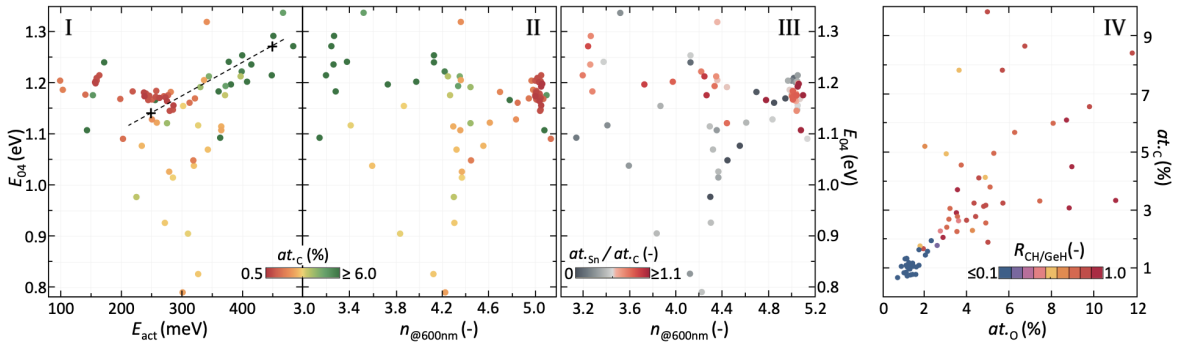

Figure 5.23: The influence of carbon on the opto-electrical properties of GeSn:H.

However, I graph shows the majority of green spots with higher $at._C$ are concentrated at higher E_{act} and consequently at higher E_{04}. This occurs regardless of the dependency between $at._O$ and $at._C$, E_{act} generally appears with higher oxygen integration [62]. In Ge:H phase dandling bonds are passivated by oxygen rather than hydrogen, hence oxygen is responsible for σ_{ph} decrease although the optical bandgap energy. Hence, IV graph indicates that Ge-dangling bonds are passivated by the C atoms from TMT precursor instead of hydrogen, $R_{CH/GeH}$ is about 80% between 2 and 8% of $at._C$.

It is important to remark the analysis provided above matches with the deposition series of amorphous GeSn:H, whereas the trends for nano-crystalline GeSn:H has shown different results for most of the measured metrics. Even if the C-concentration has played a key role in the optical and electrical properties of amorphous depositions, this cannot apply to the case of nano-crystalline films. By reducing the duty cycle this latter has provided a decrease of optical bandgap energy and photo-conductivity, and an increase of activation energy.

In the nano-crystalline conditions, lower $at._C$ and $at._O$ and higher $at._{Sn}/at._C$ have been measured than the amorphous samples. Hence, it has been analysed the relation been the crystallinity χ_C measured with Raman spectroscopy, $at._{Sn}$ and c-Ge peaks position to understand the crystalline phase in heterogeneous nc-GeSn:H samples and this has revealed a GeSn crystalline phase in such

material. Additionally, $at._{Sn}/at._{C}$ has pointed out Sn easily integrated into the growth of nanocrystalline structure rather than the amorphous one, resulting also in higher Sn concentration. In brief, the results have made it possible to achieve low E_{04} with a duty cycle lower than 2000 for nc-GeSn:H films, whereas a-GeSn:H depositions have required moderate duty cycle and high temperature for low E_{04}.

Subsequently, the analysis has been focused on how the temperature influences the amorphous GeSn films growth. Three deposition series have been diversified in terms of TMT dilution in F_{He} (from 0 sccm to 10 sccm with an increment of 5 sccm) and duty of cycle, δ equals 429 with 0 sccm and 10 sccm of F_{He}, whereas δ is 3333 with 5 sccm of F_{He}. The main challenge of processing stable and dense amorphous GeSn is to achieve low E_{04} with a low duty cycle as well. Even if a high deposition temperature allows the growth of dense materials, this does not prevent porosity. Hence, oxidation occurs easily and obstructs the amorphous a-GeSn:H growth at the conditions just defined.

Additionally, the series with the highest duty cycle has shown that working at a higher temperature leads to a higher refractive index with less oxidation and low optical bandgap energy. On the other hand, the atomic concentration between Sn and C is not affected by the temperature increase. However, oxygen may passivate dangling bonds in hydrogenated germanium and so, it can decrease the defect density, but the drop of E_{act} cannot be prevented. Hence, it seems that the right direction is the inclusion of oxygen other than hydrogen to achieve amorphous materials with good electrical features.

The last part of the analysis has been based on how the series of GeSn:H samples behave depending on the radio frequency power P_{RF} value. Figure 5.24 points out processing at high power is more favourable for low E_{04}, because it allows a higher dissociation rate of precursor gasses and hence, larger material growth.

This means that the increase of power helps to dissociate precursors with higher-dissociation energy, in other words, H_2 and CH_n dissociate more easily than GeH_4 and this latter breaks its bonds more readily than TMT. It should be noted that if the fraction of $Sn(CH_n)_n$ decreases, then $at._{Sn}$ decreases accordingly. Looking at $R_{CH/GeH}$ plot in the region with high power, the ratio of the C-H bonds drops in reference to the Ge-H bonds in the infrared spectra. Therefore, this is the result of higher GeH_4 dissociation than CH_3 groups from TMT.

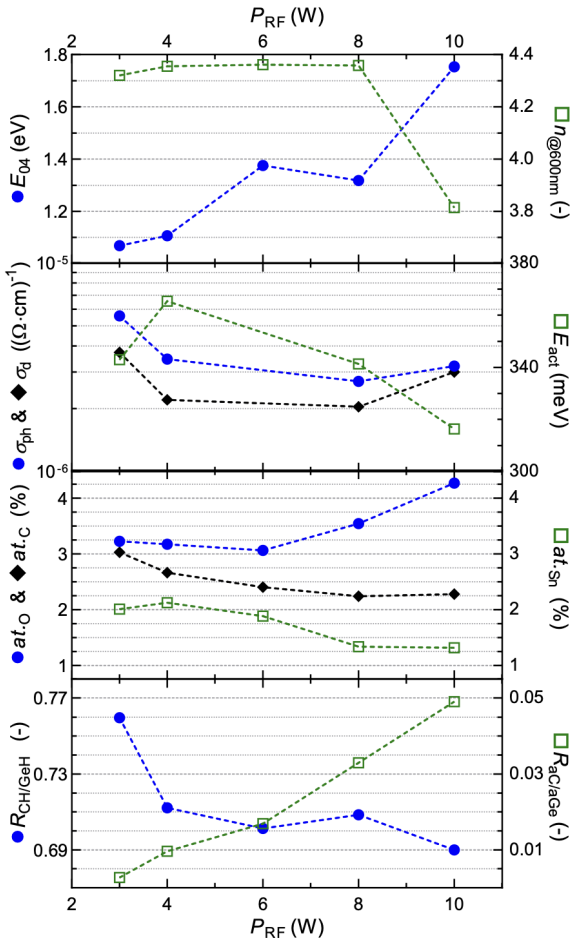

Figure 5.24: P_{RF} trends as a function of optical and electrical properties of GeSn:H samples. Deposition conditions: T=230 °C, F_{He}=5 sccm and δ=2857.

6

Conclusions and Outlooks

This Chapter has been divided into two main sections. Section 6.1 summarises the main outcomes obtained through detailed optical modelling and the first experimental results for the development of a lightweight and flexible Si-based triple-junction solar cell on Al substrate. Section 6.2 provides several recommendations on how the solar cell modelling might be improved. Then, further suggestions have been given in order to overcome challenges related to deposition and fabrication. This aims to offer a potential pathway towards the fabrication of a new frontier of photovoltaic technology.

6.1. Conclusions

6.1.1. Modelling section

The optical modelling has pointed out how MST with FLAM01 texturing enhances the light scattering at the interfaces, whereas the extended net-radiation method has shown how the ray tracing model suits better the triple-junction optical performance in terms of active layers absorption and photo-generated currents.

It has been demonstrated the thicknesses of intrinsic layers have to meet the current matching requirement for an optimised spectral utilisation. The top sub-cell thickness seems to be favourable between 80 nm and 100 nm, in this range, the bottom sub-cell has a feasible thickness in terms of manufacturing. At the thickest thicknesses combination, the total photo-generated current density finds a value higher than 27 mA/cm^2.

Furthermore, if aluminium is replaced with silver at the back reflector, it is possible to reach 28 mA/cm^2 of spectral utilisation. A further refinement is given by the embedding of ARC on front side, which may improve the light trapping properties by 4%. Here, the encapsulant boosts the photo-generation current density to 28.5 mA/cm^2 and unbalances the currents in active layers. By favouring the absorption in the top sub-cell, the impact of Staebler–Wronski Effect will affect less the solar cell performance. The front reflector optimisation has indicated IOH might be an FTO alternative among available transparent conductive oxide materials. Compared to FTO, IOH reduces the absorptance by 5% on average, resulting in 60% reduction of photo-generated current in the front reflector.

6.1.2. Experimental section

The first deposition series has exhibited the presence of cracks with such thicknesses. Even if a-Si(i)/nc-Si(i)/nc-Si(i) absorber layers were deposited without any current matching criteria, among 196 diodes analysed, more than 130 showed a parallel resistance in the order of magnitude of 100 k Ω cm^2. The second bunch has underlined the improvements of Ag material as back reflector,

measurements has shown the J_{sc} increase and the R_{series} reduction. It has been also observed some V_{oc} measurements were higher than expected due to potential amorphous phase in the layers below the top sub-cell.

The optimisation of bottom sub-cell has led to an investigation on different low bandgap energy materials, such as amorphous hydrogenated germanium tin films. Using high TMT concentration has underlined the formation of Sn-clusters that avoid lowering E_g during the deposition. On the other hand, it has been seen higher carbon integration through TMT favours the bandgap energy decrease. Related drawbacks are the material porosity and the samples oxidation. By also regulating power and temperature, some of the challenges has been attenuated.

6.2. Outlooks

6.2.1. Modelling section

The current matching analysis has underlined the challenge of increasing the thickness of a-Si:H top sub-cell and keeping the bottom sub-cell at feasible thickness simultaneously. For this reason, the optical modelling should investigate IOH as front reflector and silver as back reflector because their optical properties might enhance the light absorption in the near infrared region of solar spectrum.

It is also clear the developed optical modelling can be considered partially reliable because the electrical properties have been neglected completely. Therefore, the association of optical and electrical modelling would then allow foreseeing the comprehensive operation of the triple-junction solar device.

6.2.2. Experimental section

From the fabrication side, triple-junction thin-films on Al substrate have been processed for the first time and still several issues have to be solved. The current processing route has not been standardised for the triple-junction solar cells. The manufacturing still requires refinements in the lamination procedure, but also in the tuning of temperature and time for etching and annealing process.

The first attempts have been investigated at the maximum feasible a-Si:H thickness with low J_{sc} and V_{oc} mainly due to mismatched currents in the absorber layers. The second deposition series has investigated the lowest boundary for a-Si material thickness and in this case, sub-cells have been deposited in current matching condition. The lack of measurements does not allow asserting that thin a-Si top sub-cells are not achievable. Therefore, new deposition series are highly recommended, where the J-V curves analysis should be also associated with the EQE measurements, which have not been looked into yet.

Further samples should be deposited with IOH as front reflector and silver as back reflector. According to the modelling, this may be a solution to achieve a thicker top sub-cell, and a feasible and thinner bottom sub-cell. Additionally, it appears reasonable to investigate other materials belonging to IV group, which have exhibited a promising direction for the spectral utilisation at long wavelength.

Appendices

A

Matlab triple-junction architecture

```
%Simulation of triplejunction cell with FLAM01 texturing
% Al as back reflector
% model='ray'

clear all
clc
clear Lay Int

%===LAYERS===
Lay(1).med = 'air';                    Lay(1).thi = inf;
%INTERFACE 1
Lay(2).med = 'FTO';                    Lay(2).thi = 0.700;
%INTERFACE 2
Lay(3).med = 'a-Si(i)';                Lay(3).thi = 0.080;
%INTERFACE 3
Lay(4).med = 'nc-Si(i)';               Lay(4).thi = 1.100;
%INTERFACE 4
Lay(5).med = 'nc-Si(i)';               Lay(5).thi = 2.500;
%INTERFACE 5
Lay(6).med = 'air';                    Lay(6).thi = inf;

% INTERFACES : coatings are part of the interface
load('R2R_Flam01','Flam01');           %FLAM01 texturing

% Interface 1: between layer 1 and 2 (air/FTO)
Int(1).model = 'ray';
Int(1).Z = -Flam01*1e6;
Int(1).xy = [20,20];

Int(1).coat(1).med = 'ETFE';           Int(1).coat(1).thi = 25;
Int(1).coat(2).med = 'Glue';           Int(1).coat(2).thi = 90;
Int(1).coat(3).med = 'ETFE';           Int(1).coat(3).thi = 25;
Int(1).coat(4).med = 'Glue';           Int(1).coat(4).thi = 100;


% Interface 2: between layer 2 and 3 (FTO/a-si)
Int(2).model = 'ray';
Int(2).Z = -Flam01*1e6;
Int(2).xy = [20,20];
```

```
Int(2).coat(1).med = 'AZO';           Int(2).coat(1).thi = 0.020;
Int(2).coat(2).med = 'nc-SiOx(p)';    Int(2).coat(2).thi = 0.010;

% Interface 3: between layer 3 and 4 (a-Si/nc-si)
Int(3).model = 'ray';
Int(3).Z = -Flam01*1e6;
Int(3).xy = [20,20];

Int(3).coat(1).med = 'nc-SiOx(n)';  Int(3).coat(1).thi = 0.020;
Int(3).coat(2).med = 'nc-SiOx(p)';  Int(3).coat(2).thi = 0.016;

% Interface 4: between layer 4 and 5 (nc-Si/nc-si)
Int(4).model = 'ray';
Int(4).Z = -Flam01*1e6;
Int(4).xy = [20,20];

Int(4).coat(1).med = 'nc-SiOx(n)';  Int(4).coat(1).thi = 0.020;
Int(4).coat(2).med = 'nc-SiOx(p)';  Int(4).coat(2).thi = 0.016;

% Interface 5: between layer 5 and 6 (nc-Si/air)
Int(5).model = 'ray';
Int(5).Z = -Flam01*1e6;
Int(5).xy = [20,20];

Int(5).coat(1).med = 'nc-SiOx(n)';  Int(5).coat(1).thi = 0.015;
Int(5).coat(2).med = 'AZO';         Int(5).coat(2).thi = 0.080;
Int(5).coat(3).med = 'Al';          Int(5).coat(3).thi = 0.300;

% Execution Section
S.wav = 0.300:0.005:1.200;
% Wave length Range 300 to 1200 nm with 0.005 nm step
S.SM = 1;
[Lay,Int,out] = GENPRO4(Lay,Int,S);
% both 'Lay' and 'Int' are input

out.wav=1000*out.wav;
out.abp=out.abp';
```

B

Matlab triple-junction current matching

```
%if this code is not run directly after Appendix A code,
%load a workspace with output data from a previous simulation
%of 3J architecture

load('WSFLAM01_Al_cm80nm.mat')

%don't plot height map, only abs.
S.plot = 0;
% top absorber thickness values
T_ta = 0.080;
% middle absorber thickness values
T_ma = 0.85:0.05:1.1;
% bottom absorber thickness values
T_ba = 2.35:0.05:2.60;

% initialize
st=size(T_ta);
sm=size(T_ma);
sb=size(T_ba);
J_ta=zeros(st.*sm.*sb);
J_tm=zeros(st.*sm.*sb);
J_tb=zeros(st.*sm.*sb);

ii=1;

for tt = 1:length(T_ta)
    Lay(3).thi = T_ta(tt);
   for tm= 1:length(T_ma)
       Lay(4).thi = T_ma(tm);
      for tb = 1:length(T_ba)
          Lay(5).thi = T_ba(tb);

        [Lay,Int] = GENPRO4(Lay,Int,S);    %re-run simulation

          J_ta(ii)= Lay(3).cur;            %store current in vector
          J_tm(ii)= Lay(4).cur;            %store current in vector
          J_tb(ii)= Lay(5).cur;            %store current in vector
          ii=ii+1;
```

```
            drawnow
41        end
      end
43  end

45
    n=size(T_ma);              %n gives T_ma size: 1 row and #columns
47
    T_m=zeros(n.*n);
49  N=n(1,2);

51  T_m=reshape(repmat(T_ma, N,1),1,N*length(T_ma));
    %Matlab functions to create T_m combinations
53
    T_b=repmat(T_ba,n(1,1),n(1,2));
55  %Matlab function to create T_b combinations


57
    figure(5)
59  plot(T_ma,T_ba)
    scatter(T_m,T_b)
61  grid on
    xticks(T_ma)
63  yticks(T_ba)
    xlabel('Middle cell thickness values [um]');
65  ylabel('Bottom cell thickness values [um]');
    %title ('Space representation: J middle and
67  %J bottom [mA/cm^2] as the thickness varies')

69  for i=1:length(J_tm)
        xt=T_m(1,i);
71      yt=T_b(1,i);
        t={[J_tm(1,i), J_tb(1,i)]};
73
        text(xt,yt,t);
75
    end
77
    %legend('J middle and J bottom [mA/cm^2]')
79
    T_m=T_m';
81  T_b=T_b';
    J_tm=J_tm';
83  J_tb=J_tb';
    J_ta=J_ta';
85  J1=J_tm-J_ta;
    J2=J_tb-J_ta;
87

89  %current matching

91  u=size(J_ta);
    cm=zeros(6,u(1,1)*u(1,2));
93
    for i=1:length(J_tm)
95      if (abs(J_ta(i)-J_tm(i)) <0.1) && (abs(J_ta(i)-J_tb(i)) < 0.1)
```

```
97          cm(1,i)=J_ta(i);
            cm(2,i)=J_tm(i);
99          cm(3,i)=J_tb(i);
            cm(4,i)=T_ta;
101         cm(5,i)=T_m(i);
            cm(6,i)=T_b(i);
103         formatSpec = 'Jtop=%8.3f mA/cm2, Jmiddle=%8.3f mA/cm2,
            Jbottom=%8.3f mA/cm2\n
105         thick.top=%8.3f um, tick.middle=%8.3f um, thick.bottom=%8.3f um
               \n';
            fprintf(formatSpec,J_ta(i),J_tm(i),J_tb(i),T_ta,T_m(i),T_b(i))
107     end
end
```

C

Sensitivity Analysis: additional material

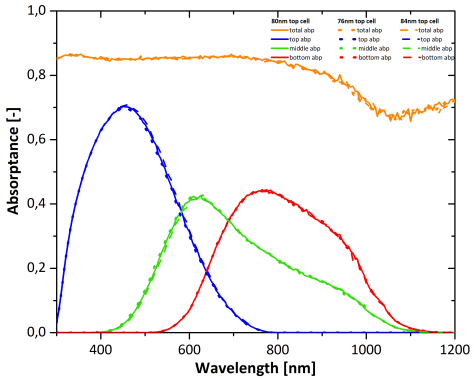

Figure C.1: Total and active layers A for [80nm±5% - 1.1 µm - 2.5 µm].

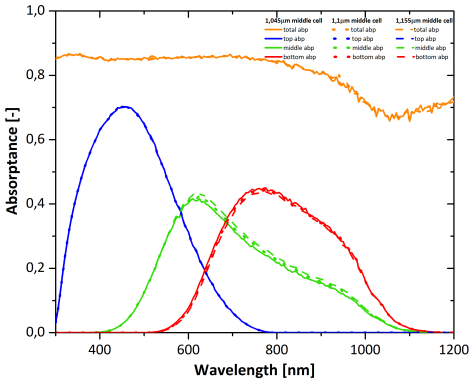

Figure C.2: Total and active layers A for [80nm - 1.1±5% µm - 2.5 µm].

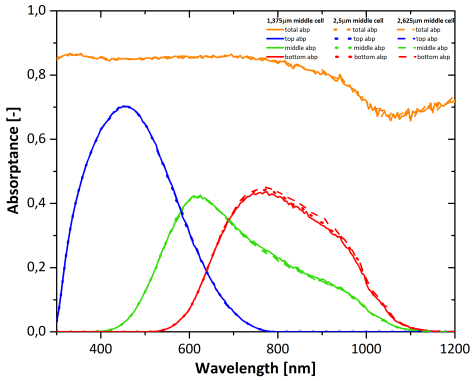

Figure C.3: Total and active layers A for [80nm - 1.1 µm - 2.5±5% µm].

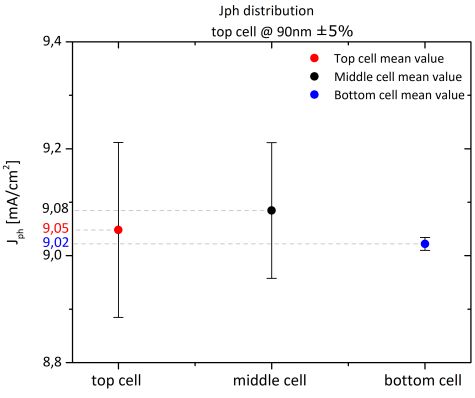

Figure C.4: J_{ph} distribution with [90nm±5% - 1.4 µm - 3.6 µm].

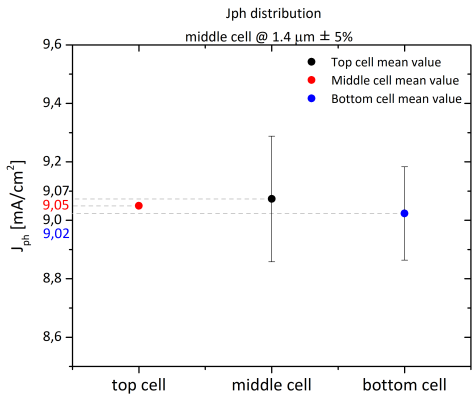

Figure C.5: J_{ph} distribution
with [90nm - 1.4±5% µm - 3.6 µm].

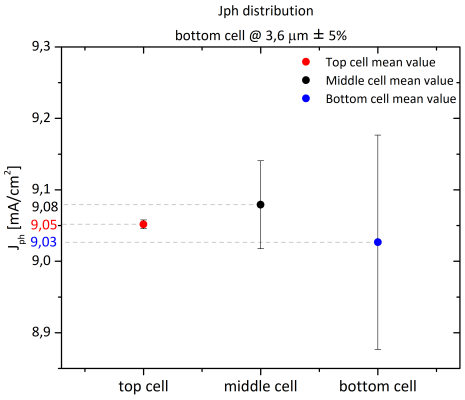

Figure C.6: J_{ph} distribution
with [90nm - 1.4 µm - 3.6±5% µm].

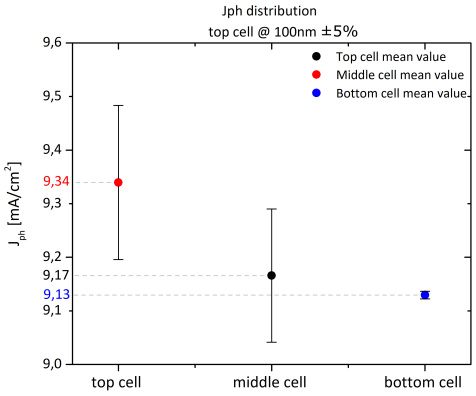

Figure C.7: J_{ph} distribution
with [100nm±5% - 1.6 µm - 4.4 µm].

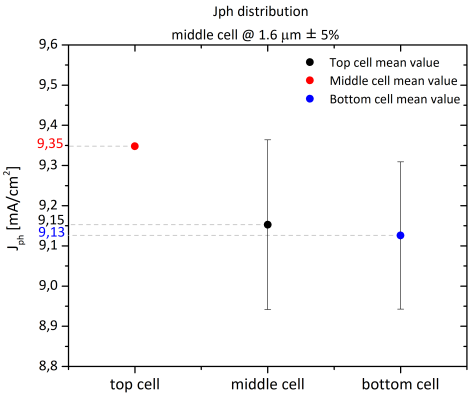

Figure C.8: J_{ph} distribution
with [100nm - 1.6±5% µm - 4.4 µm].

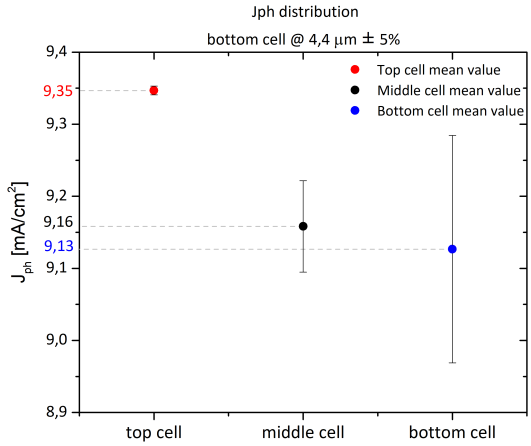

Figure C.9: J_{ph} distribution
with [100nm - 1.6 µm - 4.4±5% µm].

D

Refractive index and Absorption index of layers and coatings used in the optical modelling

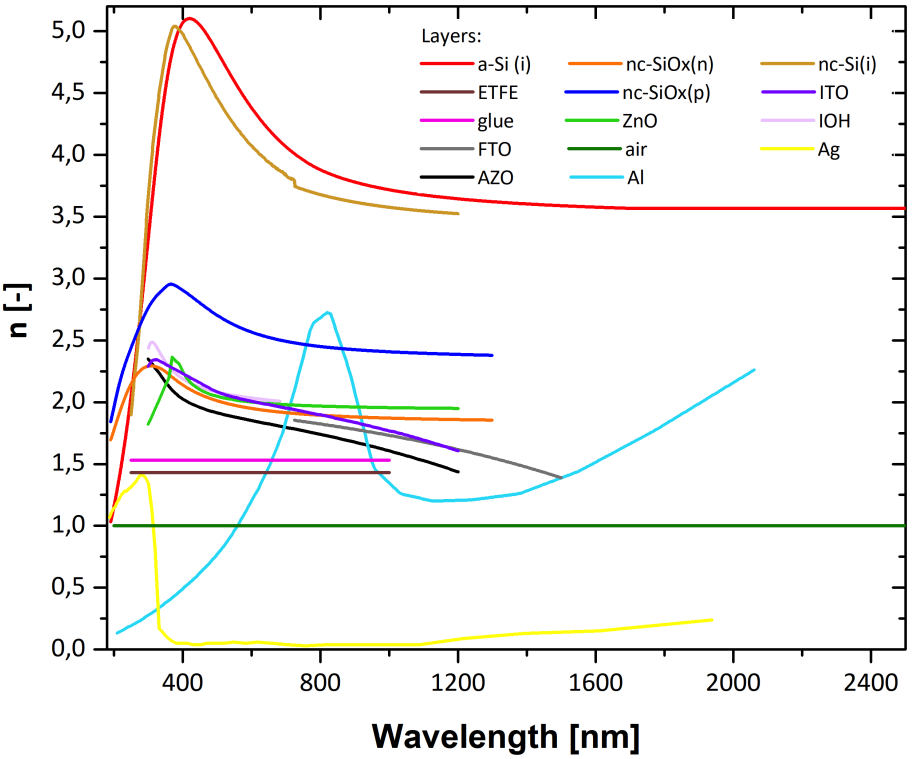

Figure D.1: Refractive index of layers and coatings modelled in the triple-junction optical modelling.

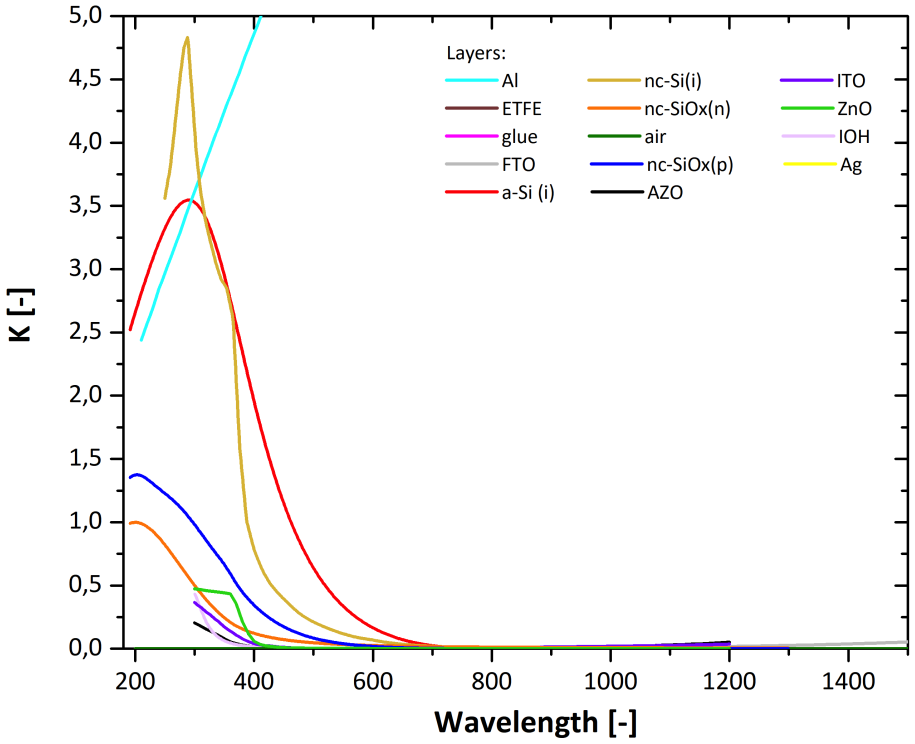

Figure D.2: Absorption index of layers and coatings modelled in the triple-junction optical modelling.

Bibliography

[1] Kevin Kinsella. Solar photovoltaic technologies fueling thin film energy markets. URL https://blog.bccresearch.com/solar-photovoltaic-technologies-fueling-thin-film-energy-markets.

[2] Kelly Pickerel, Kelly Pickerel, Sally Caron Says, Sally Caron, Kelly Pickerel says, LETICIA LAKUSIEWICZ says, Leticia Lakusiewicz, Mac says, and Mac. What is thin-film solar?, Aug 2019. URL https://www.solarpowerworldonline.com/2018/07/thin-film-solar-stuck-in-second-place-even-with-c-si-tariffs/.

[3] Klaus Jäger, Jos Lenssen, Pieter Veltman, and Edward Hamers. Large-area production of highly efficient flexible light-weight thin-film silicon pv modules. In *Proc. 28th European Photovoltaic Solar Energy Conf., Paris, France*, pages 2164–2169, 2013.

[4] HyET Solar. Vopak and hyet solar collaborate on 1mw thin-film storage tank application. URL https://www.hyetsolar.com/news/vopak-and-hyet-solar-collaborate-on-1mw-thin-film-storage-tank-application/.

[5] Rolf Enderlein and Norman JM Horing. *Fundamentals of semiconductor physics and devices*. World Scientific, 2012.

[6] David Hammen. Kyle Kanos. Uwe Pilz. How can it be that the sun emits more than a black body?, 2021. URL https://physics.stackexchange.com/questions/130209/how-can-it-be-that-the-sun-emits-more-than-a-black-body.

[7] Arno HM Smets, Klaus Jäger, Olindo Isabella, René ACMM Swaaij, and Miro Zeman. *Solar Energy: The physics and engineering of photovoltaic conversion, technologies and systems*. UIT Cambridge, 2015.

[8] Grant R Fowles. *Introduction to modern optics*. Courier Corporation, 1989.

[9] Oca.Tudelft.Nl. Semiconductor materials for solar cells., 2021. URL https://ocw.tudelft.nl/wp-content/uploads/Solar-Cells-R3-CH3_Solar_cell_materials.pdf.

[10] D. A. Neamen. *Semiconductor physics and devices: basic principles, 4th ed.* New York, NY: McGraw-Hill,,, 2012.

[11] PV education. Iv curve, 2021. URL https://www.pveducation.org/pvcdrom/solar-cell-operation/iv-curve.

[12] Hisham Nasser. Development of hybrid photonic and plasmonic light management interfaces for thin film semiconductor devices. 2015.

[13] EM Spaans. Optimisation of a-si: H/μc-si: H tandem solar cell on flexible al substrates: Use of modelling for cell design and performance predictions. 2020.

[14] Joost Adriaan Willemen. Modelling of amorphous silicon single-and multi-junction solar cells. 1998.

[15] Braden Bills, Xianbo Liao, David W Galipeau, and Qi Hua Fan. Effect of tunnel recombination junction on crossover between the dark and illuminated current–voltage curves of tandem solar cells. *IEEE transactions on electron devices*, 59(9):2327–2330, 2012.

[16] P Babál. Doped nanocrystalline silicon oxide for use as (intermediate) reflecting layers in thin-film silicon solar cells. 2014.

[17] Pere Roca i Cabarrocas. Deposition techniques and processes involved in the growth of amorphous and microcrystalline silicon thin films. In *Physics and technology of amorphous-crystalline heterostructure silicon solar cells*, pages 131–160. Springer, 2012.

[18] Rudi Santbergen, Tomomi Meguro, Takashi Suezaki, Gensuke Koizumi, Kenji Yamamoto, and Miro Zeman. Genpro4 optical model for solar cell simulation and its application to multijunction solar cells. *IEEE journal of photovoltaics*, 7(3):919–926, 2017.

[19] Light trapping. URL `https://www.pveducation.org/pvcdrom/design-of-silicon-cells/light-trapping`.

[20] Gianluca Limodio, Davide Bartesaghi, Maurice Hietkamp, Devika Rajagopal, Sajith Nawaratne, Robin Quax, Edward Hamers, and Arno Smets. Modulated surface texturing of temporary al foils substrates for high-efficiency thin film, flexible solar cells (conference presentation). In *Photonics for Solar Energy Systems VIII*, volume 11366, page 113660C. International Society for Optics and Photonics, 2020.

[21] Klaus Jäger. On the scalar scattering theory for thin-film solar cells. 2012.

[22] G. Bauer. Anti-reflection coatings. URL `https://www.pveducation.org/pvcdrom/design-of-silicon-cells/anti-reflection-coatings`.

[23] Devika Rajagopal. Modulated surface texturing on temporary aluminium substrate for flexible thin-film solar cells. 2020.

[24] Delft University of Technology and HyET Solar. Project description. *Flexible Lightweight Advanced Materials In Next Generation Of PV: Flamingo PV*, August 2018.

[25] Roar Søndergaard, Markus Hösel, Dechan Angmo, Thue T Larsen-Olsen, and Frederik C Krebs. Roll-to-roll fabrication of polymer solar cells. *Materials today*, 15(1-2):36–49, 2012.

[26] Egbert Boeker and Rienk Van Grondelle. *Environmental physics: sustainable energy and climate change*. John Wiley & Sons, 2011.

[27] Mikhail A Kats, Romain Blanchard, Patrice Genevet, and Federico Capasso. Nanometre optical coatings based on strong interference effects in highly absorbing media. *Nature materials*, 12 (1):20–24, 2013.

[28] Pietro Altermatt. Fresnel equations in absorptive incoming media., 2021. URL `https://www.pvlighthouse.com.au/cms/lectures/altermatt/optics/fresnel-equations-in-absorptive-incoming-media`.

[29] M Fortes, E Comesana, JA Rodriguez, P Otero, and AJ Garcia-Loureiro. Impact of series and shunt resistances in amorphous silicon thin film solar cells. *Solar Energy*, 100:114–123, 2014.

[30] Angèle Reinders, Pierre Verlinden, Wilfried Van Sark, and Alexandre Freundlich. *Photovoltaic solar energy: from fundamentals to applications*. John Wiley & Sons, 2017.

[31] Giso Hahn and Sebastian Joos. State-of-the-art industrial crystalline silicon solar cells. In *Semiconductors and Semimetals*, volume 90, pages 1–72. Elsevier, 2014.

[32] Thierry Goudon, Vera Miljanović, and Christian Schmeiser. On the shockley–read–hall model: generation-recombination in semiconductors. *SIAM Journal on Applied Mathematics*, 67(4): 1183–1201, 2007.

[33] AV Shah, H Schade, M Vanecek, J Meier, E Vallat-Sauvain, N Wyrsch, U Kroll, C Droz, and J Bailat. Thin-film silicon solar cell technology. *Progress in photovoltaics: Research and applications*, 12(2-3):113–142, 2004.

[34] H Schade, P Lechner, R Geyer, H Stiebig, B Rech, and O Kluth. Texture properties of tco uniquely determining light trapping in thin-film silicon solar cells. In *Conference Record of the Thirty-first IEEE Photovoltaic Specialists Conference, 2005.*, pages 1436–1439. IEEE, 2005.

[35] Miro Zeman. Advanced amorphous silicon solar cell technologies. *Thin film solar cells: fabrication, characterization and applications*, pages 1–66, 2006.

[36] Hellmut Fritzsche. Development in understanding and controlling the staebler-wronski effect in a-si: H. *Annual Review of Materials Research*, 31(1):47–79, 2001.

[37] Arvind Shah. *Thin-film silicon solar cells*, volume 68. EPFL press Lausanne, 2010.

[38] James M Gee. The effect of parasitic absorption losses on light trapping in thin silicon solar cells. In *Conference Record of the Twentieth IEEE Photovoltaic Specialists Conference*, pages 549–554. IEEE, 1988.

[39] R Hussin, SZS Anuar, SA Ibharim, Z Kamdi, AR Ainuddin, and Z Harun. Deposition of zno-al (azo) thin films for optical properties. In *AIP Conference Proceedings*, volume 2339, page 020198. AIP Publishing LLC, 2021.

[40] Akihisa Matsuda. Amorphous and microcrystalline silicon. *Springer Handbook of Electronic and Photonic Materials*, page 581, 2007.

[41] John Robertson. Growth mechanism of hydrogenated amorphous silicon. *Journal of non-crystalline solids*, 266:79–83, 2000.

[42] Simon Min Sze. *Semiconductor devices: physics and technology*. John wiley & sons, 2008.

[43] Robert Siegel. Net radiation method for transmission through partially transparent plates. 1973.

[44] Rudi Santbergen, Arno HM Smets, and Miro Zeman. Optical model for multilayer structures with coherent, partly coherent and incoherent layers. *Optics express*, 21(102):A262–A267, 2013.

[45] Norio Sato. *Electrochemistry at metal and semiconductor electrodes*. Elsevier, 1998.

[46] Liang Ding, T Chen, Yecheng Liu, Chi Yung Ng, Mengliu Yang, J Wong, Furong Zhu, M Tan, S Fung, X Chen, and ying-sheng Huang. Evolution of photoluminescence mechanisms of si+-implanted sio2 films with thermal annealing. *Journal of nanoscience and nanotechnology*, 8: 3555–60, 08 2008. doi: 10.1166/jnn.2008.128.

[47] Amirah Way, Joel Luke, Alex D Evans, Zhe Li, Ji-Seon Kim, James R Durrant, Harrison Ka Hin Lee, and Wing C Tsoi. Fluorine doped tin oxide as an alternative of indium tin oxide for bottom electrode of semi-transparent organic photovoltaic devices. *AIP Advances*, 9(8):085220, 2019.

[48] Mahdiyar Nouri Rezaie, Negin Manavizadeh, Ebrahim Nadimi, and Farhad Akbari Boroumand. Quality enhancement of azo thin films at various thicknesses by introducing ito buffer layer. *Journal of Materials Science: Materials in Electronics*, 28(13):9328–9337, 2017.

[49] Yifeng Zhao, Paul Procel, Can Han, Luana Mazzarella, Guangtao Yang, Arthur Weeber, Miro Zeman, and Olindo Isabella. Design and optimization of hole collectors based on nc-siox: H for high-efficiency silicon heterojunction solar cells. *Solar Energy Materials and Solar Cells*, 219:110779, 2021.

[50] GOVIND PADMAKUMAR. Fabrication and analysis of a-si: H/μc-si: H tandem solar cell on flexible al substrates: A flamingo pv project. 2021.

[51] Pierre Lamond and Paul Berman. High efficiency silicon solar cells. Technical report, TRANSITRON ELECTRONIC CORP WAKEFIELD MA, 1960.

[52] A Kromka, O Babchenko, S Potocky, B Rezek, A Sveshnikov, P Demo, T Izak, and M Varga. Diamond nucleation and seeding techniques for tissue regeneration. In *Diamond-Based Materials for Biomedical Applications*, pages 206–255. Elsevier, 2013.

[53] Hairen Tan, Efthymia Psomadaki, Olindo Isabella, Marinus Fischer, Pavel Babal, Ravi Vasudevan, Miro Zeman, and Arno HM Smets. Micro-textures for efficient light trapping and improved electrical performance in thin-film nanocrystalline silicon solar cells. *Applied Physics Letters*, 103(17):173905, 2013.

[54] Klaus Jäger, Dane NP Linssen, Olindo Isabella, and Miro Zeman. Ambiguities in optical simulations of nanotextured thin-film solar cells using the finite-element method. *Optics express*, 23(19):A1060–A1071, 2015.

[55] Patrick Campbell and Martin A Green. Light trapping properties of pyramidally textured surfaces. *Journal of Applied Physics*, 62(1):243–249, 1987.

[56] Keith R McIntosh and Simeon C Baker-Finch. Opal 2: Rapid optical simulation of silicon solar cells. In *2012 38th IEEE Photovoltaic Specialists Conference*, pages 000265–000271. IEEE, 2012.

[57] K Jäger, M Fischer, RACMM Van Swaaij, and M Zeman. A scattering model for nano-textured interfaces and its application in opto-electrical simulations of thin-film silicon solar cells. *Journal of Applied Physics*, 111(8):083108, 2012.

[58] Guangzhu Ding, Kaixuan Wang, Xiaohui Li, Qing Chen, Zhijun Hu, and Jieping Liu. The fabrication of nanoimprinted p3ht nanograting by patterned etfe mold at room temperature and its application for solar cell. *Nanoscale research letters*, 11(1):1–11, 2016.

[59] Klaus Ellmer. Magnetron sputtering of transparent conductive zinc oxide: relation between the sputtering parameters and the electronic properties. *Journal of Physics D: Applied Physics*, 33(4):R17, 2000.

[60] P Pearcef, T Wilsonf, A Johnson, and N Ekins-Daukes. Characterization of sigesn for use as a 1 ev sub-cell in multi-junction solar cells. In *2018 IEEE 7th World Conference on Photovoltaic Energy Conversion (WCPEC)(A Joint Conference of 45th IEEE PVSC, 28th PVSEC & 34th EU PVSEC)*, pages 0943–0948. IEEE, 2018.

[61] Thierry de Vrijer, Ashwath Ravichandran, Bilal Bouazzata, and Arno HM Smets. The impact of processing conditions and post-deposition oxidation on the opto-electrical properties of hydrogenated amorphous and nano-crystalline germanium films. *Journal of Non-Crystalline Solids*, 553:120507, 2021.

[62] Thierry de Vrijer, Julian EC van Dingen, Paul J Roelandschap, Koos Roodenburg, and Arno HM Smets. Improved pecvd processed hydrogenated germanium films through temperature induced densification. *Materials Science in Semiconductor Processing*, 138:106285, 2022.